

Mohammad Dehghani

Development of Advanced Computational Techniques for Alloys in Complex Atomic and Magnetic Configurational States

Doctoral thesis

conducted at Materials Center Leoben Forschung GmbH
Roseggerstrasse 12, A-8700 Leoben, Austria

under the supervision of
Assoc.-Prof. Dr. Peter Puschnig
Institute of Physics
University of Graz, Graz, Austria

and

Prof. Dr. Andrei Ruban
Department of Materials Science and Engineering
KTH Royal Institute of Technology, SE-100 44 Stockholm, Sweden

Leoben, 2017

To my lovely wife, Maedeh and my wonderful son, Kian.

Abstract

One of the most suitable approaches for first-principles electronic structure calculations of metallic alloys with complex chemical and magnetic structure is a Green's-function based method as implemented within the exact muffin-tin orbital formalism. This method, in combination with the coherent potential approximation is very efficient in modeling multicomponent alloys. In this thesis, we address two issues related to the computational efficiency and accuracy of some parts of this methodology.

The first problem is a formalism for calculating the energy-dependent structure constant matrix using a Taylor expansion. Replacing this approach with a more accurate and efficient method is necessary not only to solve existing problems appearing for some systems in the current implementation, but also to make the calculations numerically efficient in view of future developments. To this end, we have developed a new formalism which calculates the structure constants matrices for each energy directly. However, the implementation has led to unphysical irregularities related to finite size of real-space clusters. The numerical results show that it is impossible to eliminate them using the current procedure. We conclude with a discussion whether the method can be applied as a reliable replacement of the Taylor expansion method.

The second issue is related to unreliable values of elastic constants for low symmetry crystals, which is due to some computational inaccuracies within the current implementation, leading to numerical problems in the total energy as a function of strain. Here, we have introduced a number of new improvements which enhance numerical accuracy of the total energy-strain curves and lead to reliable values of elastic constants for such systems. These improvements have been applied to calculate elastic properties of the shape memory alloy $\text{NiTi}_{(1-x)}\text{Hf}_x$. Our results show a good agreement with other computational data and experimental observations.

Zusammenfassung

Einer der geeignetsten Ansätze für ab-initio Berechnungen der elektronischen Struktur von metallischen Legierungen mit komplexen chemischen und magnetischen Aufbau ist eine auf den Greenschen Funktionen basierende Methode, wobei die Formulierung ähnlich wie im exakten muffin-tin-orbital Formalismus auf der Vielfachstreuungstheorie basiert. In Verbindung mit der kohärenten Potentialnäherung ist das sehr effizient zum Modellieren von komplexen Materialien. In dieser Dissertation werden zwei Aspekte behandelt, die Effizienz und Genauigkeit der Methode betreffen.

Als erster Aspekt dieser Dissertation wird ein Formalismus zur Berechnung der energieabhängigen Strukturkonstantenmatrix mittels der Taylorentwicklung behandelt. Das Ersetzen dieses Formalismus mit einer genaueren Methode ist notwendig um existierenden Probleme zu lösen, aber auch um die Rechnungen effizienter zu machen für zukünftige Entwicklungen. Dazu wurde die Strukturkonstantenmatrix für jede Energie direkt berechnet. Jedoch zeigt dieser neue Formalismus auf, dass die numerische Berechnung von Strukturkonstanten wegen der endlichen Größe von Clustern im Realraum zu Singularitäten führt. Wir zeigen, dass es nicht möglich ist, diese Singularitäten im jetzigen Formalismus zu verhindern. Daher wird diskutiert, ob der neue Formalismus ein verlässlicher Ersatz für die Taylorentwicklung ist.

Zweitens betrachten wir elastische Konstanten für Systeme mit niedriger Symmetrie, welche wegen Ungenauigkeiten der aktuellen Implementation unzuverlässig sind. Diese Ungenauigkeiten führen zu großem Rauschen für totale Energie vs. Dehnung Kurven. Mittels Verbesserungen, die Energie-Dehnungs-Kurve glätten, werden verlässliche Werte für elastische Konstanten erhalten. Als Beispiel werden die elastischen Eigenschaften der Formgedächtnislegierung $\text{NiTi}_{(1-x)}\text{Hf}_x$ berechnet. Die Resultate stimmen gut mit anderen Berechnungen und experimentellen Beobachtungen überein.

Contents

1	Introduction	1
2	Density Functional Theory	5
2.1	Born-Oppenheimer Approximation	5
2.2	The Hohenberg-Kohn Theorems	7
2.2.1	v -representability and the Levy Constrained Search Formalism	9
2.3	The Kohn-Sham Scheme	10
2.4	The Exchange and Correlation Energy	11
2.4.1	The Local Density Approximation	12
2.4.2	Generalized Gradient Approximation	13
2.5	Methods for Solving the Kohn-Sham Equations	14
3	Basics of Green's Function Methods	17
3.1	Green's Function and Scattering	17
3.2	Energy-dependent Green's Function	19
3.3	Single-potential Scattering and the t -matrix	20
3.4	Formal Development of MST	21
3.5	MST for Muffin-tin Potentials	24
4	Exact Muffin-tin Orbital Theory	28
4.1	EMTO Basis Set	29
4.1.1	Screened Spherical Waves	30
4.1.2	Partial Waves	31
4.2	Kink Cancellation Equation and the Path Operator	33
4.3	Electron Density	35
4.4	Single-electron Potential	36
4.5	Full Charge Density Technique	38
4.5.1	Shape Function Technique	39
4.5.2	FCD Total Energy	41
4.6	EMTO-CPA method	43
4.7	EMTO-CPA code	47
5	Slope Matrix	48
5.1	Inhomogeneous Dyson equation	49
5.1.1	Blowing-up Technique	50
5.1.2	Energy Derivatives of the Slope Matrix	51
5.2	Details of Real Space-Cluster Calculations	52
5.3	Taylor Expansion	53
5.4	Direct Calculation of the Slope Matrix	55

CONTENTS

5.4.1	Application of Directly Calculating S^a and \dot{S}^a	58
5.5	Conclusion	66
6	Calculating Elastic Constants of $\text{NiTi}_{(1-x)}\text{Hf}_x$ Alloys	68
6.1	Ab-initio Calculation of Elastic Constants	69
6.1.1	Polycrystalline Elastic Constants	72
6.2	NiTiHf: A High Temperature Shape Memory Alloy	73
6.3	NiTi Structures and Details of Calculations	75
6.4	Details of the New Developments	77
6.4.1	Application of the ElaStic Package	77
6.4.2	Application of the <i>Voro</i> -shape Package	78
6.4.3	Modification on Radial Mesh Points	79
6.5	Results	81
6.5.1	Structural Parameters of $\text{NiTi}_{1-x}\text{Hf}_x$	81
6.5.2	Elastic Properties of $\text{NiTi}_{1-x}\text{Hf}_x$	84
6.6	Conclusion	94
	Acknowledgments	95
	List of Figures	96
	List of Tables	98
	Bibliography	99

Chapter 1

Introduction

Owing to the ever growing availability of computational resources, first-principles quantum mechanical description of solids is becoming an increasingly attractive method in solid state physics and material science. Thus, accurate electronic structure calculations are entering the materials design process, particularly for systems which are difficult to characterize by means of experimental methods. Density functional theory (DFT) [1, 2] has been among the most popular and versatile theoretical tools providing such an *ab initio* description. By means of DFT calculations, ground state material properties, such as lattice parameters, elastic properties, or phase stability are being routinely evaluated. The results of such calculations for many systems are typically in excellent agreement with experimental observations. However, there are also classes of materials which challenge existing first-principles methodologies. Among those are steels, undoubtedly one of the most important technological materials, which can be characterized as metallic alloys having a complex chemical and magnetic structure with a complicated temperature behavior. The main difficulty of studying such systems is to model the randomness of the atomic positions in the substitutional alloys or magnetic moments in the paramagnetic state, keeping a methodological framework based on the translational symmetry of the underlying crystal lattice.

During the past decades, many attempts have been made to develop accurate and, at the same time, efficient methods for solving the Kohn-Sham equations in applications of DFT for condensed matter. The majority of these methods are

based on diagonalization of the Kohn-Sham Hamiltonian [2]. Many formalisms of this type have been developed in the framework of either an all-electron full-potential technique [3–5], which fulfills the accuracy requirement, or pseudo-potential approximation [6, 7] which guarantees efficiency and accuracy at the same time on an acceptable level. Due to considerable progresses in this area, many codes have been developed based on these methods such as WIEN2k¹ [8] and VASP² [9–11], considered today as standard choices for performing calculations. However, they are not well-suited to describe properties of disordered alloys, since they become too cumbersome for modeling randomness in solids.

On the other hand, there is another group of methods based on the Green’s-function technique which, in contrast to the diagonalization methods, are well-suited for modeling the effects of random disorder in crystalline materials. It is in the pioneering works of Korringa [12] and Kohn and Rostocker [13] that for the first time multiple scattering theory (MST) was used to solve the Kohn-Sham equation and applied on band structure calculation of solids. Hence, they are also known as KKR methods. These methods, in combination with approximations such as coherent potential approximation (CPA) [14, 15] and disordered local moment (DLM) [16, 17] have made the electronic structure calculation of substitutional random alloys and modeling finite temperature magnetism possible.

The most well-adapted basis set for a Green’s function based method are muffin-tin orbitals. In the original KKR method non-overlapping muffin-tin spheres were used as an approximation to the geometry of a crystal. Soon it became clear that an overlapping muffin-tin sphere formalism can approximate the crystal potential more accurately, however, it also brings many technical difficulties in developing the method and its applications. Various solutions were proposed to overcome these difficulties, among which the most systematic is known as exact muffin-tin orbital (EMTO) theory [18] introduced by O. K. Andersen in late 1990’s. Subsequently, a KKR formalism using the EMTO basis set in combination with the CPA was developed [19–21] which is called hereafter EMTO-CPA method.

Compared to methods such as WIEN2k and VASP, the current formalism of EMTO-CPA is not accurate enough for calculating energetics of structural relaxations. For instance, it typically overestimates the elastic constants of high symmetry crystals compared to other more accurate computational methods. Moreover, it yields unreliable elastic constants for low symmetry solids. The main source of errors in such calculations arises from the use of the spherical cell approximation (SCA) [22]. In this approximation, the one-electron potential is assumed to be spherically symmetric within an atomic sphere. This approxima-

¹<http://www.wien2k.at/>

²<https://www.vasp.at/>

tion is usually too drastic to model the full one-electron potential, thus providing insufficiently accurate energetics of structural relaxations. Moreover, elastic constant calculations involve deformations that lower the symmetry of the system and thus have a strong dependence on non-spherical parts of the potential which are not considered in the SCA.

To improve the accuracy of the total energy, the full charge density (FCD) technique [23, 24] is used in the current EMTO-based implementations. In this technique, the total energy is calculated from the full charge density obtained from a converged self-consistent EMTO-SCA calculation. This means that the FCD step is done only once at the end of the calculation after the convergence of EMTO-SCA calculation has been achieved. A promising idea to improve the accuracy of the method is to introduce the FCD technique into the self-consistent cycle. Thereby, total energies are expected to reach accuracy comparable to full-potential codes. But before making such a modification of the computational scheme, there are other technical issues of the implementation which must be solved (improved) in advance.

The first issue we address in this thesis is the problem of calculating energy-dependent structure constants. Structure constants are the coefficients appearing in the so-called "one-center expansion" for the wave function in the interstitial region. This matrix and its first energy derivative, which are needed for each energy during the self-consistent cycle, are calculated using a Taylor expansion with respect to some reference energy. The structure constants matrix and its first several energy derivatives for the reference energy are calculated for a finite-size cluster of lattice vectors in real space by means of a Dyson equation. Then, they are transformed into the reciprocal space and are used to solve the KKR equation at each energy during the self-consistent cycle. This approach leads to inaccuracy in some cases. Moreover, the problem of the efficiency will deteriorate if the FCD technique is introduced to the self-consistent cycle. Therefore, it is necessary to replace it with an accurate and more efficient formalism. In this thesis, we introduce our new implementation and present its results in which the structure constants and its first energy derivative are calculated directly at any arbitrary energy by the Dyson equation.

Another source of errors in calculations of elastic constants of low symmetry crystals is an irregular behavior of the total energy as a function of strain which leads to unreliable values for elastic constants. In this thesis, we present our results for the elastic properties of the shape memory alloy NiTiHf in both $B2$ and $B19'$ phases. In order to improve the accuracy of the results, we have analyzed the origin of the errors and introduced necessary modifications, which lead to reliable elastic constants by improving the smoothness of energy-strain graphs. The most important modifications are, the integration of EMTO-CPA code with

Chapter 1. Introduction

ElaStic [25] software, which facilitate elastic constants calculations, and the *Voro*-shape package, which improves the accuracy of the total energy in case of low symmetry crystals.

This thesis is organized as follows. In Chapter 2 a summary of the basic concepts of the DFT is presented followed by Chapter 3 which deals with the basics of the Green's function methods including formal development of MST and its application to non-overlapping muffin-tin potentials, resulting in the KKR equation. Chapter 4 contains the details of the EMTO-CPA formalism such as the EMTO basis set, SCA potential, FCD technique and CPA concept. In Chapter 5 the current formalism for calculating the structure constants is described, and details and numerical results of our new implementation for direct calculation of these matrices are discussed. Finally, Chapter 6 deals with our result for elastic properties of shape memory alloys $\text{NiTi}_{(1-x)}\text{Hf}_x$ with $x = \{0, 0.1, 0.2, 0.3, 0.4, 0.5\}$. In this Chapter, first we review shortly the main concepts of the elasticity theory. Then, we give a brief review on properties of NiTiHf shape memory alloys. Finally, we present the details of our new developments for elastic constants calculation, as well as the results for $\text{NiTi}_{(1-x)}\text{Hf}_x$ alloys.

Chapter 2

Density Functional Theory

DFT is the primary tool for electronic structure calculations in condensed matter. With the help of this theory, the original many-body problem is simplified to an effective one-electron one, thereby making possible an accurate *ab initio* consideration of relatively large and complex systems. The main concept of DFT originates from the Hohenberg-Kohn theorems [1]. Its modern formulation, which is used in present-day methods for treating electrons in condensed matter, is based on the Kohn-Sham approach [2]. But before reviewing these topics, let us begin with some preliminaries.

2.1 Born-Oppenheimer Approximation

Most of the problems in the electronic structure of matter are covered by the time-independent Schrödinger equation: $\hat{H}\psi = E\psi$, where the Hamiltonian \hat{H} of a system consisting of nuclei and electrons (in Gaussian units) is:

$$\begin{aligned} \hat{H} = & - \sum_I \frac{\hbar^2}{2M_I} \nabla_I^2 - \frac{\hbar^2}{2m_e} \sum_i \nabla_i^2 + \frac{1}{2} \sum_{i \neq j} \frac{e^2}{|\mathbf{r}_i - \mathbf{r}_j|} \\ & + \frac{1}{2} \sum_{I \neq J} \frac{Z_I Z_J e^2}{|\mathbf{R}_I - \mathbf{R}_J|} - \sum_{i,I} \frac{Z_I e^2}{|\mathbf{r}_i - \mathbf{R}_I|. \end{aligned} \tag{2.1}$$

Chapter 2. Density Functional Theory

Here, $\hbar = h/2\pi$ and h is the Planck's constant, M_I are the masses of the nuclei, m_e is the electron mass, Z_I the nuclei charge, and e the electron charge. The first two terms are the kinetic energy of the electrons and nuclei, respectively; the third, fourth and fifth terms are the electron-electron, nucleus-nucleus and electron-nucleus interaction energies.

Nuclei are much heavier than electrons, and thus they are moving much slower, so that the full Schrödinger equation can be decoupled assuming that at any instant position of the nuclei, the electrons are fast enough to remain in their corresponding ground state. This is the Born-Oppenheimer approximation [26]. In this adiabatic approximation, the solution for the coupled system of nuclei and electrons is given by:

$$\Psi = \psi(\mathbf{r}_i; \{\mathbf{R}\})\chi(\mathbf{R}), \quad (2.2)$$

where the curly brackets indicate set of all \mathbf{R} and semicolon is to emphasize that $\{\mathbf{R}\}$ are parameters, not coordinates. $\psi(\mathbf{r}_i; \{\mathbf{R}\})$ satisfies the Schrödinger equation for the electrons in the potential of the now fixed nuclei at positions \mathbf{R}_I :

$$\left(-\frac{\hbar^2}{2m_i} \sum_i \nabla_i^2 + \frac{1}{2} \sum_{i \neq j} \frac{e^2}{|\mathbf{r}_i - \mathbf{r}_j|} - \sum_{i,I} \frac{Z_I e^2}{|\mathbf{r}_i - \mathbf{R}_I|} \right) \psi(\mathbf{r}_i; \{\mathbf{R}_I\}) = E_e(\mathbf{R}_I) \psi(\mathbf{r}_i; \{\mathbf{R}_I\}), \quad (2.3)$$

where the electron eigenvalues E_e depend on the \mathbf{R}_I . If we now apply the Hamiltonian, Eq. (2.1), to the wave function, Eq. (2.2), we get:

$$\begin{aligned} \hat{H}\Psi &= - \sum_I \frac{\hbar^2}{2M_I} \nabla_I^2 \Psi + \frac{1}{2} \sum_{I \neq J} \frac{Z_I Z_J e^2}{|\mathbf{R}_I - \mathbf{R}_J|} \Psi + E_e(\mathbf{R}) \Psi \\ &= E_e(\mathbf{R}) \Psi + \psi(\mathbf{r}_i, \{\mathbf{R}\}) \left(- \sum_I \frac{\hbar^2}{2M_I} \nabla_I^2 + \frac{1}{2} \sum_{I \neq J} \frac{Z_I Z_J e^2}{|\mathbf{R}_I - \mathbf{R}_J|} \right) \chi(\mathbf{R}) \\ &\quad - \sum_I \frac{\hbar^2}{2M_I} (2 \nabla_I \chi(\mathbf{R}) \nabla_I \psi(\mathbf{r}_i; \{\mathbf{R}\}) + \chi(\mathbf{R}) \nabla_I^2 \psi(\mathbf{r}_i; \{\mathbf{R}\})). \end{aligned} \quad (2.4)$$

The two terms in the last line are called non-adiabatic terms, and they are neglected in the Born-Oppenheimer approximation (see Ref. [27] for more details). In this case, $\chi(\mathbf{R})$ satisfies a Schrödinger-like equation:

$$\left(- \sum_I \frac{\hbar^2}{2M_I} \nabla_I^2 + \frac{1}{2} \sum_{I \neq J} \frac{Z_I Z_J e^2}{|\mathbf{R}_I - \mathbf{R}_J|} + E_e(\mathbf{R}) \right) \chi(\mathbf{R}) = E \chi(\mathbf{R}). \quad (2.5)$$

Thus, in the Born-Oppenheimer approximation, the problem is reduced to solving Eqs. (2.3) and (2.5) for electrons and nuclei, respectively. Eq. (2.5) is

what would be the Schrödinger equation for the nuclei alone and is the basis of the perturbation methods for the description of lattice vibrations of systems. Eq. (2.3) is the starting point for all methods which have been developed for investigating electronic structure of solids.

2.2 The Hohenberg-Kohn Theorems

Because of an exponential scaling with system size, it is too complicated to solve the original N -electron Schrödinger equation, Eq. (2.3), practically for many-electron systems. Hence, there is a long history of methods which are trying to get around this problem. Among them, the most important worth mentioning one, is the method of Thomas [28] and Fermi [29] proposed in 1927. Although this method is not accurate enough for today's electronic structure calculations, the idea of replacing the complicated N -electron wave function description by a much simpler one based on the one-electron density had a great impact upon the development of DFT. Both Thomas and Fermi neglected exchange and correlation effects; however, their theory was extended by Dirac [30] in 1930, who formulated the local density approximation for exchange energy still in use today. Nevertheless, the Thomas-Fermi-Dirac theory remains rather inaccurate for most applications. The largest source of error is in the representation of the kinetic energy, followed by the errors in the exchange energy, and due to the complete neglect of electron correlation.

Inspired by Thomas-Fermi-Dirac theory, P. Hohenberg and W. Kohn laid the foundation of DFT by proving the following theorems [1]:

Theorem I: For any system of interacting particles in an external potential, $V_{ext}(\mathbf{r})$, the potential $V_{ext}(\mathbf{r})$ is determined uniquely, except for a constant, by the ground state particle density $n_0(\mathbf{r})$.

Theorem II: A universal functional for the energy $E[n]$ in terms of the density $n_0(\mathbf{r})$ can be defined, valid for any external potential $V_{ext}(\mathbf{r})$. For any particular $V_{ext}(\mathbf{r})$, the exact ground state energy of the system is the global minimum value of this functional, and the density $n(\mathbf{r})$ that minimizes the functional is the exact ground state density $n_0(\mathbf{r})$.

The consequence of the first theorem is that all ground-state properties of a system are completely determined by its ground state electron density $n_0(\mathbf{r})$. In the original Hohenberg-Kohn paper, this theorem is proved for densities with non-degenerate ground states. The proof is elementary, and by contradiction. Suppose there are two potentials V_1 and V_2 differing by more than a constant, yielding

Chapter 2. Density Functional Theory

the same density. These would have two different ground-state wave-functions, ψ_1 and ψ_2 . Then, unless, $V_1 - V_2 = \text{const.}$, ψ_1 is different from ψ_2 since they are solutions of the same Schrödinger equation. So, if the Hamiltonians and energies associated with ψ_1 and ψ_2 are denoted by \hat{H}_1 , \hat{H}_2 and E_1 , E_2 , respectively, we have:

$$\begin{aligned} E_1 &= \langle \psi_1 | \hat{H}_1 | \psi_1 \rangle < \langle \psi_2 | \hat{H}_1 | \psi_2 \rangle = \langle \psi_2 | \hat{H}_2 + \hat{V}_1 - \hat{V}_2 | \psi_2 \rangle \\ &\Rightarrow E_1 < E_2 + \int (V_1(\mathbf{r}) - V_2(\mathbf{r}))n(\mathbf{r})d\mathbf{r}. \end{aligned} \quad (2.6)$$

Changing the indices of quantities leads to:

$$E_2 < E_1 + \int (V_2(\mathbf{r}) - V_1(\mathbf{r}))n(\mathbf{r})d\mathbf{r}. \quad (2.7)$$

By adding Eq. (2.6) and Eq. (2.7), we get $E_1 + E_2 < E_2 + E_1$, which is obviously false. Therefore, the total energies, E_1 and E_2 , must be equal, which implies that ψ_1 and ψ_2 are the same wave-functions by the variational principle and the assumption of non-degeneracy. An elegant constructive proof was found later by Levy [31, 32], which automatically includes degenerate states.

In order to prove the second theorem consider the energy functional of $n(\mathbf{r})$ defined as:

$$E_{V_0}[n] = \min_{\psi \rightarrow n} \left\langle \psi[n] \left| \hat{T} + \hat{W} + \hat{V}_0 \right| \psi[n] \right\rangle, \quad (2.8)$$

where \hat{V}_0 is the external potential of a system with ground state density $n_0(\mathbf{r})$, \hat{T} is the kinetic energy operator, and \hat{W} is the electron-electron interaction operator. Now, we can use the Rayleigh-Ritz variational principle [33] and show that

$$E_0 < E_{V_0}[n], \quad (2.9)$$

where E_0 is the ground state energy and $n \neq n_0$ and, of course

$$E_0 = E_{V_0}[n_0]. \quad (2.10)$$

So, the exact ground state density can be found by minimizing the functional $E_{V_0}[n]$ over all n . But we can write $E_{V_0}[n]$ as

$$E_{V_0}[n] = F_{HK}[n] + \int V_0(\mathbf{r})n(\mathbf{r})d\mathbf{r}, \quad (2.11)$$

where

$$F_{HK}[n] = \min_{\psi \rightarrow n} \left\langle \psi[n] \left| \hat{T} + \hat{W} \right| \psi[n] \right\rangle \quad (2.12)$$

is called the Hohenberg-Kohn universal functional. F_{HK} is said to be universal, because it does not depend on the external potential and thus is the same functional for all atoms, molecules, and solids.

2.2.1 v -representability and the Levy Constrained Search Formalism

When proving the Hohenberg-Kohn theorem above, we assumed that the density is v -representable, which means that it is a density associated with the anti-symmetric ground state wave function and some external potential $V_0(\mathbf{r})$. The reason for such an assumption is that we want to use the variational character of the energy functional in Eq. (2.9). If our trial density that we put in this functional turns out to be non- v -representable, the variational principle is no longer valid.

The Levy constrained-search formulation [31, 32] provides a way around the problem of v -representability and in the same way presents a constructive proof of the Hohenberg-Kohn theorem. According to Eq. (2.8) the minimization of $E_{V_0}[n]$ can be written as:

$$\begin{aligned} \langle \psi_0 | \hat{T} + \hat{W} | \psi_0 \rangle + \int V_0(\mathbf{r})n(\mathbf{r})d\mathbf{r} &\leq \langle \psi_{n_0} | \hat{T} + \hat{W} | \psi_{n_0} \rangle + \\ \int V_0(\mathbf{r})n(\mathbf{r})d\mathbf{r} &\Rightarrow \langle \psi_0 | \hat{T} + \hat{W} | \psi_0 \rangle = \langle \psi_{n_0} | \hat{T} + \hat{W} | \psi_{n_0} \rangle. \end{aligned} \quad (2.13)$$

Here ψ_0 is the ground state wave function and ψ_{n_0} is any other wave function yielding the same density. We recognize this as the Hohenberg-Kohn functional, F_{HK} . It turns out that the ground state wave function of density $n(\mathbf{r})$ can be defined as the wave function which yields $n(\mathbf{r})$ and minimizes the Hohenberg-Kohn functional.

The Levy constrained-search formulation of the Hohenberg-Kohn theorem proposes a two-step minimization procedure for the ground state energy. First, we minimize $E_{v_0}[n]$ over all wave functions giving a certain density, and then over all densities:

$$\begin{aligned} E_0 &= \min_{\psi} \langle \psi | \hat{T} + \hat{W} + \hat{V} | \psi \rangle \\ &= \min_n \left(\min_{\psi \rightarrow n} \langle \psi | \hat{T} + \hat{W} + \hat{V} | \psi \rangle \right) \\ &= \min_n \left(\min_{\psi \rightarrow n} \langle \psi | \hat{T} + \hat{W} | \psi \rangle + \int V(\mathbf{r})n(\mathbf{r})d\mathbf{r} \right). \end{aligned} \quad (2.14)$$

Here, the minimization is over all n which are N -representable, which means n can be obtained from an anti-symmetric wave function with the following three conditions: It should be positive, it should integrate to N , and it should be finite. This is obviously a much weaker condition than v -representability, and any

reasonable density fulfills it. The word "constrained" in Levy constrained search method comes from the fact that the ψ that we search among, are constrained to give the density n .

2.3 The Kohn-Sham Scheme

The year after Hohenberg and Kohn published their article, Kohn and Sham published another one [2] in which they presented an effective computational scheme to find the ground state electron density. They proposed to consider a system of non-interacting electrons with the same density as the physical system. The main achievement of this approach is that the complicated N -electron Schrödinger equation is replaced by a set of one-electron equations, known as Kohn-Sham equations, which are much easier to solve.

Let us consider such an auxiliary system of non-interacting electrons. For a system with N independent electrons, the ground state has one electron with spin σ in each of the N^σ orbitals $\phi_i^\sigma(\mathbf{r})$ and therefore the density is given by

$$n(\mathbf{r}) = \sum_{\sigma} n(\mathbf{r}, \sigma) = \sum_{\sigma} \sum_{i=1}^{N^\sigma} |\phi_i^\sigma(\mathbf{r})|^2, \quad (2.15)$$

where $N = N^\uparrow + N^\downarrow$. The kinetic energy of this system in Hartree atomic units ($\hbar = m_e = e = 1/(4\pi\epsilon_0) = 1$) is

$$T_s = -\frac{1}{2} \sum_{\sigma} \sum_{i=1}^{N^\sigma} \langle \phi_i^\sigma | \nabla^2 | \phi_i^\sigma \rangle = \frac{1}{2} \sum_{\sigma} \sum_{i=1}^{N^\sigma} |\nabla \phi_i^\sigma|^2. \quad (2.16)$$

The Kohn-Sham approach for the full interacting many-electron system starts by rewriting the total energy in the following form:

$$E_{KS} = T_s[n] + \int V_{ext}(\mathbf{r})n(\mathbf{r})d\mathbf{r} + E_{Hartree}[n] + E_{xc}[n] + E_{II}, \quad (2.17)$$

where $V_{ext}(\mathbf{r})$ is the external potential due to the nuclei and $E_{Hartree}(\mathbf{r})$ is the Coulomb energy of the electron density $n(\mathbf{r})$, which is

$$E_{Hartree} = \frac{1}{2} \int \frac{n(\mathbf{r})n(\mathbf{r}')}{|\mathbf{r} - \mathbf{r}'|} d\mathbf{r}d\mathbf{r}' \quad (2.18)$$

and E_{II} is the Coulomb energy of the nuclei. Comparing Eq. (2.17) and Eq. (2.11), one can find the following expression for E_{xc} which is called exchange-correlation energy,

$$E_{xc}[n] = T[n] - T_s[n] + E_{int}[n] - E_{Hartree}[n], \quad (2.19)$$

2.4. The Exchange and Correlation Energy

where $E_{int}[n]$ is the internal interaction energies of the true interacting many-body system including classical and non-classical terms. One can see that $E_{xc}[n]$ must be a functional of the density, since the right-hand sides of the equations are also functionals of the density.

The solution of the Kohn-Sham auxiliary system for the ground state can be viewed as the problem of minimization with respect to the density. Since T_s in Eq. (2.16) is explicitly expressed as a functional of orbitals but all other terms are considered to be functional of the density, one can use the chain rule and vary Eq. (2.17) by Rayleigh-Ritz principle to derive the variational equation,

$$\frac{\partial E_{KS}}{\partial \phi_i^{\sigma*}} = \frac{\partial T_s}{\partial \phi_i^{\sigma*}} + \left[\frac{\partial E_{ext}}{\partial n(\mathbf{r}, \sigma)} + \frac{\partial E_{Hartree}}{\partial n(\mathbf{r}, \sigma)} + \frac{\partial E_{xc}}{\partial n(\mathbf{r}, \sigma)} \right] \frac{\partial n(\mathbf{r}, \sigma)}{\partial \phi_i^{\sigma*}} = 0, \quad (2.20)$$

subject to the orthonormalization constraint

$$\langle \phi_i^\sigma | \phi_j^{\sigma'} \rangle = \delta_{i,j} \delta_{\sigma\sigma'}. \quad (2.21)$$

Using Eqs. (2.15) and (2.16), and the method of Lagrange multipliers one can find the single-electron Kohn-Sham equations set

$$\left[-\frac{1}{2} \nabla^2 + V_{ext}(\mathbf{r}) + \int \frac{n(\mathbf{r}')}{|\mathbf{r} - \mathbf{r}'|} + v_{xc}^\sigma(\mathbf{r}) \right] \phi_i^\sigma = \varepsilon_i \phi_i^\sigma, \quad (2.22)$$

where $v_{xc}(\mathbf{r}) = \partial E_{xc} / \partial n(\mathbf{r})$ is the exchange-correlation potential. Since the potential depends on the density, these equations should be solved in a self-consistent way. Usually one starts with an initial guess for $n(\mathbf{r})$, then calculates the corresponding potential and solves the Kohn-Sham equations for the ϕ_i^σ . From these one calculates a new density and starts again. This procedure is then repeated until convergence is reached. After convergence, using the solution $n(\mathbf{r})$ the total energy of real system can be found from the following expression,

$$E[n] = \sum_i \varepsilon_i - E_{Hartree}[n] + E_{xc}[n] - \int v_{xc}(\mathbf{r}) n(\mathbf{r}) d\mathbf{r} + E_{II}. \quad (2.23)$$

The only principle problem with the above equations is that the exact form of functional for exchange-correlation energy is unknown, and therefore it must be approximated. Fortunately, it turns out to be relatively easy to find reasonably good local approximations for it.

2.4 The Exchange and Correlation Energy

The accuracy of density functional theory calculations is, in principle, limited only by the employed approximate functionals describing the exchange and correlation

energy. Basically, $E_{xc}[n]$ is the sum of the distinct exchange and correlation terms,

$$E_{xc}[n] = E_x[n] + E_c[n]. \quad (2.24)$$

Even though the exact functional $E_{xc}[n]$ is presumably quite complex, great progress in practical applications could be made with remarkably simple approximations. We shall now take a look at the two most well-known and widely-used approximations for $E_{xc}[n]$.

2.4.1 The Local Density Approximation

Kohn and Sham pointed out in their paper [2] that solids with slowly varying density can be considered as close to the limit of a homogeneous electron gas. In that limit, a system with non-uniform electron density, can be treated as a collection of infinitesimally-small uniform electron gases of density n and therefore, the total exchange-correlation energy can be obtained by summing the individual contributions over all space. This is the local density approximation (LDA) for which $E_{xc}[n]$ has the following form

$$E_{xc}[n(\mathbf{r})] = \int n(\mathbf{r}) \mathcal{E}_x^{hom}(n(\mathbf{r})) \mathbf{r} + \int n(\mathbf{r}) \mathcal{E}_c^{hom}(n) d\mathbf{r}. \quad (2.25)$$

Here \mathcal{E}_x^{hom} and \mathcal{E}_c^{hom} represent the exchange and correlation energies per electron of a homogeneous electron gas, respectively.

$\mathcal{E}_x^{hom}(n)$ can be calculated analytically [30]. For a homogeneous electron gas the eigenfunctions are plane waves. Integrating over all states is equal to the number of electrons in the system N . Therefore, it is easy to show that

$$N = V \frac{k_F^3}{3\pi^2} \Rightarrow n = \frac{k_F^3}{3\pi^2} = \frac{3}{4\pi r_s^3}, \quad (2.26)$$

where V is the volume, k_F is the Fermi wave vector and the Seitz radius, r_s , is introduced as the radius of a sphere which on average contains one electron. The exchange energy per electron for a homogeneous electron gas, is obtained by calculating the Fock integral [27]:

$$\mathcal{E}_x^{hom}(k_F) = -\frac{3k_F}{4\pi}. \quad (2.27)$$

This leads to the following term for LDA exchange energy

$$E_x^{LDA}[n(\mathbf{r})] = -\frac{3}{4} \left(\frac{3}{\pi}\right)^{1/3} \int n^{4/3}(\mathbf{r}) d\mathbf{r}. \quad (2.28)$$

2.4. The Exchange and Correlation Energy

Accurate analytic expressions for \mathcal{E}_c^{hom} are known only in extreme limits. The high-density ($r_s \rightarrow 0$) limit is also the weak-coupling limit [34], in which

$$\mathcal{E}_c^{hom}(r_s) = c_0 \ln(r_s) - c_1 + r_s (c_2 \ln(r_s) - c_3) + \dots, \quad (2.29)$$

and the low-density ($r_s \rightarrow \infty$) is also the strong coupling limit [35], in which

$$\mathcal{E}_c^{hom}(r_s) = -\frac{d_0}{r_s} + \frac{d_1}{r_s^{3/2}} + \dots. \quad (2.30)$$

An analytical expression for \mathcal{E}_c^{hom} was proposed by Perdew and Wang [36] which encompasses these two limits. Subsequently, Ceperly and Alder found the coefficients of this expression by fitting to accurate quantum Monte-Carlo data [37]. Some other well-known, and regularly used, parameterizations have been made by Hedin and Lundqvist [38], von Barth and Hedin [39], Gunnarsson and Lundqvist [40], Vosko, Wilk, and Nusair [41], and Perdew and Zunger [42]. A detailed description of the above equations are found in [43].

The local density approximation was the standard approach for all density functional calculations until the early 1990s and is still used to a very large extent for solid state calculations. However, it typically overestimates crystal cohesive and molecular binding energies and it is not well suited for strongly correlated systems.

2.4.2 Generalized Gradient Approximation

The first step beyond the LDA is a functional of the magnitude of the gradient of the density $|\nabla n^\sigma|$ as well as the value $n(\mathbf{r})$ at each point. This approximation is referred to as generalized gradient approximation (GGA). A first attempt at doing this was the so-called *gradient expansion approximation* (GEA), first suggested in the original paper of Kohn and Sham and carried out by Herman et al. [44]. However, it does not lead to a consistent improvement over the LDA. It violates the sum rules and other relevant conditions [44] and, indeed, often leads to worse results.

A GGA functional, on the other hand, can be defined in its most general form as [45]:

$$\begin{aligned} E_{xc}^{GGA}[n(\mathbf{r})] &= \int \mathcal{E}_{xc}(n(\mathbf{r}), |\nabla n(\mathbf{r})|) n(\mathbf{r}) d\mathbf{r} \\ &= \int \mathcal{E}_x^{hom}(n) F_{xc}(n, |\nabla n|) n(\mathbf{r}) d\mathbf{r}, \end{aligned} \quad (2.31)$$

where $F_{xc}(n, |\nabla n|) \equiv F_{xc}(r_s(\mathbf{r}), s(\mathbf{r}))$ is called the enhancement factor. Here, $s(\mathbf{r})$ is the dimensionless density gradient defined by:

$$s = \frac{|\nabla n(\mathbf{r})|}{2k_F n(\mathbf{r})}. \quad (2.32)$$

Considering Eq. (2.26), the explicit expression for the gradient can be written as

$$s = \frac{3}{2} \left(\frac{4}{9\pi} \right)^{1/3} |\nabla r_s|. \quad (2.33)$$

For the exchange energy F_x has been calculated analytically in case of slowly varying densities ($s \ll 1$) [45, 46]

$$F_x = 1 + \mu s^2. \quad (2.34)$$

with μ as the effective gradient coefficient. In the spin-polarized case, it is straightforward to show that there is a "spin-scaling relation" [43]

$$E_x[n^\uparrow, n^\downarrow] = \frac{1}{2} E_x[2n^\uparrow] + \frac{1}{2} E_x[2n^\downarrow], \quad (2.35)$$

where $E_x[n]$ is the exchange energy for an unpolarized system of the density. Thus we need only the spin-unpolarized $F_x[n, |\nabla n|]$. Numerous forms for $F_x(n, s)$, have been proposed. These can be illustrated by the three widely used forms of Becke (B88) [47], Perdew and Wang (PW91) [36], and Perdew, Burke and Enzerhof (PBE) [48].

For correlation, the quantitative form of F_c is extrapolated between low-density and high-density limits. The lowest order gradient expansion at high density ($r_s \rightarrow 0$) has been determined by Ma and Breuckner [49] to be

$$F_c = \frac{\mathcal{E}_c^{LDA}}{\mathcal{E}_x^{LDA}} (1 - 0.219s^2). \quad (2.36)$$

For instance, in GGA-PBE the form for correlation is expressed as the local correlation plus an additive term both of which depend upon the gradients and the spin polarization [48].

2.5 Methods for Solving the Kohn-Sham Equations

Here we start with a quote from the book of David J. Singh and Lars Nordström [50]: "The methods for solving Kohn-Sham equations are classified according to

2.5. Methods for Solving the Kohn-Sham Equations

the representations that are used for the density, potential and, most importantly, the Kohn-Sham orbitals. The choice of representation is made to minimize the computational and human (e.g. programming) costs of calculations, while maintaining sufficient accuracy.” These competing material and application dependent have led to the development and use of a wide variety of techniques. These techniques can be categorized based on the formalisms used to approximate the potential. The most noteworthy classes of such a categorization are as follow.

The all-electron full-potential methods have been designed to fulfill the requirement of accuracy and provide the exact local density or gradient level description of solid materials [3-5, 51-56]. Regardless of basis set choice in these methods, the Kohn-Sham equation is solved for all electrons (valence and core electrons) considering exact Coulomb terms and exchange-correlation approximation. These methods have been applied to calculate the physical properties of ordered compounds, as well as to study defects in these systems. Though, in principle, these techniques give highly accurate results in most cases, they generally demand high computational costs which almost make their application for complicated systems such as random alloys very cumbersome and often inefficient.

Pseudo-potential methods [6, 7, 57, 58] have been introduced to reduce the costs of the calculations, but simultaneously to keep the accuracy of the results compared to all-electron full-potential methods. In this approach, the electrons are divided in two groups of core and valence electrons, based on the fact that the electrons in inner shells (core electrons) are strongly bound and do not play a significant role in the chemical bonding of atoms. Thus, they are considered together with the nucleus as ion core, thereby reducing the atom to an ionic core that interacts with the valence electrons. A pseudo-potential, that approximates the potential felt by the valence electrons, is built in a way that the wave functions of valence electrons, called pseudo wave function, are identical to the true wave functions outside a chosen core cut-off radius, while they should be nodeless and have the same norm as the true wave functions inside that region. In practice, one often finds that the physical and chemical properties calculated using pseudo-potential methods are almost identical to those obtained using all-electron full-potential methods [59]. The higher computational speed in combination with the accurate results in pseudo-potential calculations, compared to the all-electron full-potential ones, have made this method the first choice for doing *ab initio* calculations for most structures.

”Another important class of Kohn-Sham methods is built around the muffin-tin approximation to the effective potential and electron density. The basis of this approximation lies in the fact that the crystal potential is assumed to be spherically symmetric within the muffin-tin region and constant in the interstitial” [20]. Many full-potential electronic structure methods mentioned above employ

Chapter 2. Density Functional Theory

this approximation, but there are also methods such as LMTO-ASA [60–62] which are not full-potential. The latter is based on the atomic sphere approximation (ASA) which considers only the spherically symmetric part of the potential inside the spheres.

The majority of the above-mentioned methods use the Hamiltonian formalism. This means that the electronic spectrum and wave functions are calculated as eigenvalues and eigenvectors, respectively, of the corresponding Hamiltonian operator using a diagonalization technique. An equivalent way of solving the Kohn-Sham equation is to calculate the Green's function, which contains all the information about the electronic spectrum of the system. The Green's function formalism which is originally based on the MST, was first applied to describe the electronic structure of solids within the KKR method [12, 13]. The most important feature of this formalism is that it is suitable for studying disordered systems such as impurities in crystals and random alloys. This is due to the fact that the Green's function of a system has a self-averaging property, which means the statistical average of the Green's functions of a statistical ensemble can be used to calculate the average physical properties of the system. In contrary, the ensemble average of the wave function cannot easily be related to physical observables. This is a very important distinction that makes Green's function methods so fundamental and versatile compared to Hamiltonian based methods for description of electronic structure of random alloys. In the next chapter we shall review the basic concepts of this method.

Chapter 3

Basics of Green's Function Methods

The mathematical formalism behind Green's function based methods is the multiple scattering theory which was first formulated by Lord Rayleigh in 1892 [63] for the propagation of heat or electricity through inhomogeneous media. Since then, it has been applied for different problems in physics ranging from scattering of electromagnetic waves in optics to the electronic structure calculations in condensed matter physics. Within the latter, MST was first used for the calculation of stationary electronic states by Korringa [12]. Kohn and Rostoker extended MST to solve the eigenvalue problem for periodic lattices [13]. Since then, the theory has come to be known as the KKR method for the calculation of electronic structure and has been used as the basis for a number of related Green's function based methods. In this chapter we give a brief introduction to MST and KKR method. This chapter is mainly based on the book by A. Gonis and W. H. Buttler [64]

3.1 Green's Function and Scattering

We begin with the time-dependent form of the single-particle Schrödinger equation in Rydberg atomic units ($\hbar = 2m_e = e^2/2 = 1$),

$$i\frac{\partial}{\partial t}\psi(t) = H\psi(t), \quad (3.1)$$

Chapter 3. Basics of Green's Function Methods

which describes the wave function for a single particle moving in a perturbing potential, $V(\mathbf{r}, t)$. The Hamiltonian operator can be written as

$$H = H_0 + V(\mathbf{r}, t) = -\nabla^2 + V(\mathbf{r}, t). \quad (3.2)$$

In the absence of a perturbing potential $V(\mathbf{r}, t)$, the Hamiltonian is simply $H_0 = -\nabla^2$ and the Schrödinger equation can be solved exactly in terms of the *free particle propagators*, or Green's functions $G_0^\pm(\mathbf{r}, t; \mathbf{r}', t')$,

$$\left(i \frac{\partial}{\partial t} - H_0 \right) G_0^\pm(\mathbf{r}, t; \mathbf{r}', t') = \delta(\mathbf{r} - \mathbf{r}') \delta(t - t'), \quad (3.3)$$

The Green's function $G_0(\mathbf{r}, t; \mathbf{r}', t')$ connects the values of a wave function at the space-time point (\mathbf{r}', t') to its value at time (\mathbf{r}, t) . It can be shown that in the coordinate representation, G_0^\pm take the following forms:

$$G_0^+(\mathbf{r}, t; \mathbf{r}', t') = -i \left[\frac{1}{4\pi i (t - t')^{3/2}} \right] \exp \left(\frac{i|\mathbf{r} - \mathbf{r}'|^2}{4|t - t'|} \right) \Theta(t - t'), \quad (3.4)$$

and

$$G_0^-(\mathbf{r}, t; \mathbf{r}', t') = +i \left[\frac{1}{4\pi i (t - t')^{3/2}} \right] \exp \left(\frac{i|\mathbf{r} - \mathbf{r}'|^2}{4|t - t'|} \right) \Theta(t' - t), \quad (3.5)$$

where

$$\Theta(\tau) = \begin{cases} 1 & \tau > 0, \\ 0 & \tau < 0. \end{cases} \quad (3.6)$$

Therefore, G_0^+ vanishes for the past time, $t < t'$, and it is called *retarded propagator*, whereas G_0^- vanishes in the future, and it is called *advanced propagator*. Hence, for determining the wave function at time t from its value at time $t = 0$ we must use G_0^+ ,

$$\phi(\mathbf{r}, t) = \int d\mathbf{r}' G_0^+(\mathbf{r} - \mathbf{r}', t) \phi(\mathbf{r}', 0). \quad (3.7)$$

This shows that every point in space where the wave function is non-zero at time $t = 0$, acts as a source for producing the wave function at time t .

Now considering the system influenced by perturbing potential $V(\mathbf{r}, t)$, the solution of Eq. (3.1) can be written in the form

$$\psi(\mathbf{r}, t) = \phi(\mathbf{r}, t) + \int G_0(\mathbf{r}, t; \mathbf{r}', t') V(\mathbf{r}', t') \psi(\mathbf{r}', t') d\mathbf{r}' dt'. \quad (3.8)$$

This is referred as the Lippmann-Schwinger equation and is made the formal basis of the MST.

3.2 Energy-dependent Green's Function

Developing the time-independent formalism would be more convenient for time-independent potentials, such as those commonly appearing in the determination of electronic structure of materials. In this case, the energy-dependent Green's function is the Fourier transform of the time-dependent Green's function,

$$G(E) = \int G(t)e^{i(E+i\varepsilon)t} dt \quad (3.9)$$

that results in the following formal solution:

$$G(E) = (E + i\varepsilon - H)^{-1}. \quad (3.10)$$

Here, ε is an infinitesimal positive real number, which ensures convergence of the integral in Eq. (3.8) for $t \rightarrow \infty$. More generally, one may define the above time-independent Green's function as the resolvent of the time-independent Schrödinger equation, via the operator equation

$$G(z) = (z - H)^{-1} \quad (3.11)$$

for an arbitrary complex energy $z = E + i\varepsilon$ (as long as $[z - H]$ can be inverted). The poles of $G(z)$ determine the eigenvalue spectrum. The spectral representation in real space for a system with the complete set of eigenfunctions, $|\psi_k\rangle$, and eigenvalues ϵ_k , is

$$G(\mathbf{r}, \mathbf{r}'; z) = \sum_k \frac{\psi_k(\mathbf{r})\psi_k^*(\mathbf{r}')}{z - \epsilon_k} \quad (3.12)$$

Using the Dirac identity,

$$\int_{-\infty}^{\infty} \frac{f(x)}{x - x_0 \pm i\varepsilon} dx = P \left[\int_{-\infty}^{\infty} \frac{f(x)}{x - x_0} dx \right] \mp i\pi f(x_0), \quad (3.13)$$

where P stands for the Cauchy principal part of the integral, in the limit of $\text{Im}(z) = \varepsilon \rightarrow 0^+$, the one electron density is readily obtained as follows:

$$n(\mathbf{r}) = -\frac{1}{\pi} \text{Im} \left(\int^{E_F} G(\mathbf{r}, \mathbf{r}; z) dz \right) \quad (3.14)$$

where the upper integration limit is the Fermi energy, E_F . The density of states $n(E)$ can be calculated analogously,

$$n(E) = -\frac{1}{\pi} \text{Im} \left(\int^{E_F} G(\mathbf{r}, \mathbf{r}; z) d\mathbf{r} \right) = -\frac{1}{\pi} \text{Im} [\text{Tr}(G(z))] \quad (3.15)$$

from which the one-electron energy is easily calculated,

$$E_{one-el} = \int_0^{E_F} n(E)E dE = E_F N(E_F) - \frac{1}{\pi} \int_0^{E_F} N(E) dE, \quad (3.16)$$

with $N(E)$ being the number of states. The Fermi level E_F is obtained from the nonlinear equation,

$$N(E_F) = \int_0^{E_F} n(E) dE = N_e, \quad (3.17)$$

where N_e is the number of electrons in the system. Therefore, the Green's function contains all information which is given by the eigenfunctions.

3.3 Single-potential Scattering and the *t-matrix*

Suppose the free-particle Green's function operator, G_0 and the full Green's function operator, G , defined in the following way,

$$G(z) = (z - H)^{-1} \quad , \quad G_0(z) = (z - H_0)^{-1}, \quad (3.18)$$

which are associated with the Hamiltonian H_0 and $H = H_0 + V$, respectively. They are related by the *Dyson* equation,

$$G = G_0 + G_0 V G. \quad (3.19)$$

The Lippmann-Schwinger equation can be rewritten in the following equivalent forms,

$$\begin{aligned} |\psi_\alpha^\pm\rangle &= |\phi_\alpha\rangle + G_0^\pm(E)V|\psi_\alpha^\pm\rangle \\ &= |\phi_\alpha\rangle + G^\pm(E)V|\phi_\alpha\rangle \\ &= |\phi_\alpha\rangle + G_0^\pm(E)T^\pm|\phi_\alpha\rangle. \end{aligned} \quad (3.20)$$

Here, the *t-matrix* operator, T^\pm , which is short for "transition matrix", is defined by the following relations

$$\begin{aligned} T_{\alpha\alpha'}^+ &= \langle\phi_\alpha(E_\alpha)|T^+|\phi_{\alpha'}(E_{\alpha'})\rangle = \langle\phi_\alpha(E_\alpha)|V|\psi_{\alpha'}^+(E_{\alpha'})\rangle, \\ T_{\alpha\alpha'}^- &= \langle\phi_\alpha(E_\alpha)|T^-|\phi_{\alpha'}(E_{\alpha'})\rangle = \langle\psi_\alpha^-(E_\alpha)|V|\phi_{\alpha'}(E_{\alpha'})\rangle. \end{aligned} \quad (3.21)$$

When $E_\alpha = E_{\alpha'} = E$, the *t-matrix* is called on-the-energy-shell *t-matrix*, and we have $T_{\alpha\alpha'}(E) = T_{\alpha\alpha'}^+ = T_{\alpha\alpha'}^-$. From a simple iteration of the first line of Eq.

3.4. Formal Development of MST

(3.20) and comparison with the third line, we find that T is given formally by the following expression known as Born series,

$$T = V + VG_0V + VG_0VG_0V + \cdots . \quad (3.22)$$

If this series converges, T satisfies the *Dyson* equation,

$$T = V + VG_0T \quad (3.23)$$

which has the formal solution,

$$\begin{aligned} T &= (1 - VG_0)^{-1} V \\ &= (V^{-1} - G_0)^{-1} . \end{aligned} \quad (3.24)$$

Therefore, having the *t-matrix* available, the solution of perturbed system is simplified. From Eq. (3.19), the Green's function of perturbed system can also be obtained as

$$\begin{aligned} G &= G_0 (1 - G_0V)^{-1} \\ &= (G_0^{-1} - V)^{-1} \\ &= \left(G_0^{-1} - (T^{-1} + G_0)^{-1} \right)^{-1} \\ &= \left((T^{-1} + G_0)^{-1} T^{-1} G_0^{-1} \right)^{-1} \\ &= G_0 T (T^{-1} + G_0) \\ &= G_0 + G_0 T G_0 . \end{aligned} \quad (3.25)$$

3.4 Formal Development of MST

If two perturbing potentials, V_1 and V_2 , act simultaneously on the system, it can be shown that the *t-matrix* can be obtained from the following series,

$$\begin{aligned} T(V_1 + V_2) = & T(V_1) + T(V_2) + T(V_1)G_0T(V_2) + T(V_2)G_0T(V_1) + \\ & T(V_1)G_0T(V_2)G_0T(V_1) + \cdots , \end{aligned} \quad (3.26)$$

where $T(V_i)$ is the *t-matrix* corresponding to the potential V_i acting alone. In this expression, there is no term like $T(V_1)G_0T(V_1)$, which means no two successive scattering events corresponding to the same potential can happen.

Chapter 3. Basics of Green's Function Methods

For a case in which multiple perturbing potentials, V_i , are acting simultaneously, Eq. (3.26) takes the following form,

$$\begin{aligned} T \equiv T \left(\sum_i V_i \right) &= \left[\sum_i T(V_i) \right] + \left[\sum_i T(V_i) \right] G_0 \left[\sum_j T(V_j) \right] + \dots \\ &= \sum_i t^i + \sum_i \sum_{j \neq i} t^i G_0 t^j + \dots, \end{aligned} \quad (3.27)$$

where $t^i \equiv t(V_i)$ is the *t-matrix* of potential V_i acting alone. Equivalent to Eq. (3.24), one can obtain

$$T = \sum_{i,j} T^{ij} \equiv \left[\left(\sum_i V_i \right)^{-1} - G_0 \right] \quad (3.28)$$

where $T^{i,j}$ is the sum of the all terms in Eq. (3.27) that start with t^i and end with t^j , and satisfy the *equation of motion*,

$$T^{ij} = t^i \delta_{i,j} + t^i G_0 \sum_{k \neq i} T^{kj}. \quad (3.29)$$

Eq. (3.28) shows a fundamental property that the total *t-matrix*, T , corresponding to an assembly of scattering potential cells depends on the total potential, $\sum_i V_i$, but is entirely independent of the shape, extent or overlap of individual cells. In the case of non-overlapping potentials Eq. (3.29) can be rewritten as

$$T^{ij} = t^i \delta_{i,j} + t^i \sum_{k \neq i} G_0^{ik} T^{kj}. \quad (3.30)$$

where G_0^{ik} is that part of G_0 which connects t^i to t^k in Eq. (3.27). Thus, T^{ij} can be obtained as the inverse of a matrix M with matrix elements,

$$M^{ij} = m^i \delta_{i,j} + G_0^{ij} (1 - \delta_{i,j}), \quad (3.31)$$

where $m^i \equiv (t^i)^{-1}$ is the inverse of the *t-matrix* associated with potential V_i .

In order to interpret the equations of MST in terms of wave functions, we can start from the following equation,

$$V|\psi\rangle = T|\phi\rangle, \quad (3.32)$$

which is a result of Equations (3.20) and (3.23) for the single-potential scattering case. For an assembly of scattering cells, we introduce $|\psi^{in,i}\rangle$ which describes

3.4. Formal Development of MST

the wave incident on cell i , in the presence of all other scatterers. Therefore, in analogy to Eq. (3.32) one can write

$$V_i|\psi\rangle = t^i|\psi^{in,i}\rangle, \quad (3.33)$$

where $|\psi\rangle$ denotes the solution of the Lippmann-Schwinger equation for the entire system. From Eq. (3.32) we have the relation

$$\begin{aligned} \left(\sum_i V_i\right)|\psi\rangle &= \sum_{i,j} T^{ij}|\phi\rangle \\ &= \sum_i T^i|\phi\rangle, \end{aligned} \quad (3.34)$$

where T^i describes all multiple scattering events coming from cell i , and is defined by

$$T^i = \sum_{j \neq i} T^{ij}. \quad (3.35)$$

From Eq. (3.30) one can find

$$T^i = t^i \left[1 + G_0 \sum_{k \neq i} T^k \right]. \quad (3.36)$$

Thus, from Eq. (3.34) we have

$$\begin{aligned} V_i|\psi\rangle &= T^i|\phi\rangle \\ &= t^i \left[1 + G_0 \sum_{k \neq i} T^k \right] |\phi\rangle \\ &= t^i|\psi^{in,i}\rangle, \end{aligned} \quad (3.37)$$

which leads to the equation,

$$\begin{aligned} |\psi^{in,i}\rangle &= \left[1 + G_0 \sum_{k \neq i} T^k \right] |\phi\rangle, \\ &= |\phi\rangle + G_0 \sum_{k \neq i} t^k |\psi^{in,k}\rangle, \end{aligned} \quad (3.38)$$

describing the incoming wave at cell i as the sum of an incident wave $|\phi\rangle$ and incoming waves at all other sites that are scattered there and then propagated to site i via G_0 . Finally, the wave function of the entire system can be obtained from the following equation,

$$\begin{aligned} |\psi\rangle &= |\phi\rangle + G_0 T |\phi\rangle \\ &= |\phi\rangle + G_0 \sum_i t^i |\psi^{in,i}\rangle, \end{aligned} \quad (3.39)$$

which is a multi-center expansion of the wave function in terms of the incoming waves of the system. It can also be expressed as a single-center expansion

$$|\psi\rangle = |\psi^{in,i}\rangle + |\psi^{out,i}\rangle, \quad (3.40)$$

by defining

$$|\psi^{out,i}\rangle = G_0 t^i |\psi^{in,i}\rangle. \quad (3.41)$$

Eq. (3.39) can be used to obtain bound states of the system, i.e, the states that have non-zero amplitude even in the absence of an overall incident wave, $|\phi\rangle$. Rewriting it in the form

$$\sum_j [\delta_{i,j} - G_0 t^j (1 - \delta_{ij})] |\psi^{in,j}\rangle = |\phi\rangle, \quad (3.42)$$

shows that nontrivial solutions for these states exist only if the following condition is satisfied:

$$\det |[\delta_{i,j} - G_0 t^j (1 - \delta_{ij})]| = 0. \quad (3.43)$$

In a particular representation, the left-hand side of this equation becomes a determinant that has to be solved to find the bound states of the system, for instance, the Bloch states of a periodic solid. In this case, providing that $\det[t^i] \neq 0$ (assuming that $m^i = [t^i]^{-1}$ exists), Eq. (3.43) can be rewritten in following form

$$\det[M] = \det [m^i - G_0 (1 - \delta_{ij})] = 0, \quad (3.44)$$

where the matrix M has been defined in Eq. (3.31).

3.5 MST for Muffin-tin Potentials

In a non-overlapping muffin-tin approximation, space is divided into non-overlapping spherical cells centered at different sites, and the potential is approximated to be spherically symmetric inside the cells and constant in the interstitial region. In this case, the intra-cell vectors, $\mathbf{r}_i = \mathbf{r} - \mathbf{R}_i$, which are confined inside spheres, together with the inter-cell vectors, $\mathbf{R}_{ij} = \mathbf{R}_j - \mathbf{R}_i$, satisfy the conditions,

$$\begin{aligned} |\mathbf{R}_{ij}| > |\mathbf{r}_i|, & \quad |\mathbf{R}_{ij}| > |\mathbf{r}_j|, & \quad |\mathbf{R}_{ij}| > |\mathbf{r}_i - \mathbf{r}_j| \\ |\mathbf{R}_{ij} - \mathbf{r}_j| > |\mathbf{r}_i|, & \quad |\mathbf{R}_{ij} - \mathbf{r}_i| > |\mathbf{r}_j|. \end{aligned} \quad (3.45)$$

In *coordinate representation* one can find the *t-matrix* using the following equations. First, using integral form of Eq. (3.12), one can find the following form for the free-particle propagator corresponding to the outgoing wave [64]

$$G_0(\mathbf{r}, \mathbf{r}') \equiv G_0(\mathbf{r} - \mathbf{r}') = -\frac{1}{4\pi} \frac{e^{ik|\mathbf{r}-\mathbf{r}'|}}{|\mathbf{r} - \mathbf{r}'|}, \quad (3.46)$$

3.5. MST for Muffin-tin Potentials

and then $T(\mathbf{r}, \mathbf{r}') = \sum_{i,j} T^{ij}(\mathbf{r}, \mathbf{r}')$, where the T^{ij} elements can be obtained from

$$\begin{aligned}
 T^{ij}(\mathbf{r}, \mathbf{r}') &= t^i(\mathbf{r}, \mathbf{r}')\delta_{ij} + \sum_{k \neq i} \int_{\Omega_i} d^3 r_1 \int_{\Omega_k} d^3 r_2 t^i(\mathbf{r}, \mathbf{r}_1) G_0^{ik}(\mathbf{r}_1, \mathbf{r}_2) T^{kj}(\mathbf{r}_2, \mathbf{r}') \\
 &= t^i(\mathbf{r}, \mathbf{r}')\delta_{ij} + (1 - \delta_{ij}) \int_{\Omega_i} d^3 r_1 \int_{\Omega_k} d^3 r_2 t^i(\mathbf{r}, \mathbf{r}_1) G_0^{ij}(\mathbf{r}_1, \mathbf{r}_2) t^j(\mathbf{r}_2, \mathbf{r}') \\
 &+ \sum_{k \neq i} \int_{\Omega_i} d^3 r_1 \int_{\Omega_k} d^3 r_2 \int_{\Omega_k} d^3 r_3 \int_{\Omega_j} d^3 r_4 \\
 &\times t^i(\mathbf{r}, \mathbf{r}_1) G_0^{ik}(\mathbf{r}_1, \mathbf{r}_2) t^k(\mathbf{r}_2, \mathbf{r}_3) G_0^{kj}(\mathbf{r}_3, \mathbf{r}_4) t^j(\mathbf{r}_4, \mathbf{r}') + \dots,
 \end{aligned} \tag{3.47}$$

which is equivalent to Eq. (3.30) and Eq. (3.27) in coordinate representation. Here, $G_0^{ik}(\mathbf{r}_1, \mathbf{r}_2)$ is a cell-off-diagonal element of G_0 corresponds to the vectors \mathbf{r} and \mathbf{r}' confined to cells i and k , respectively. These integral equations are very difficult to handle computationally, and therefore the coordinate representation is not interesting for real applications. Instead, the *angular momentum representation* has been found to be better suited for carrying out practical calculations.

Using the well-known expansion of the plane wave in terms of Bessel functions and spherical harmonics (Bauer's identity),

$$\begin{aligned}
 e^{i\mathbf{k}\cdot\mathbf{r}} &= 4\pi \sum_{l,m} i^l j_l(kr) Y_{l,m}(\hat{\mathbf{r}}) Y_{l,m}^*(\hat{\mathbf{k}}) \\
 &= 4\pi \sum_L i^l J_L(\mathbf{r}) Y_L^*(\hat{\mathbf{k}}),
 \end{aligned} \tag{3.48}$$

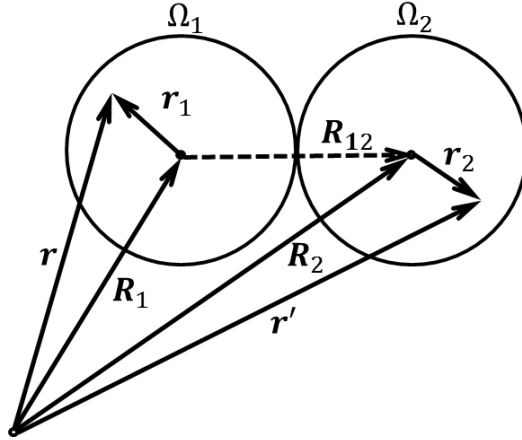


Figure 3.1: Intra-cell and inter-cell vectors in muffin-tin spheres

Chapter 3. Basics of Green's Function Methods

where $L \equiv \{l, m\}$ and $J_L(\mathbf{r}) = j_l(kr)Y_L(\hat{\mathbf{r}})$, one can find

$$G_0(\mathbf{r} - \mathbf{r}') = G_0(\mathbf{r}_1 - \mathbf{R}_{12} - \mathbf{r}_2) = -ik \sum_{L, L'} J_L(\mathbf{r}_1) G_{LL'}(\mathbf{R}_{12}) J_{L'}(\mathbf{r}_2). \quad (3.49)$$

The expansion coefficients, $G_{LL'}(\mathbf{R}_{12})$, are the real space representative of the well-known KKR *structure constants* [12, 13] which are defined as

$$G_{LL'}(\mathbf{R}) = 4\pi \sum_{L_3} i^{l_1 - l_2 - l_3} C(L_1, L_2, L_3) H_{L_3}(\mathbf{R}), \quad (3.50)$$

in which, $H_L(\mathbf{R}) = h_l(kR)Y_L(\hat{\mathbf{R}})$, with h_l denoting the Hankel function and $C(L_1, L_2, L_3)$ are the Gaunt numbers defined as

$$C(L_1, L_2, L_3) = \int Y_{L_1}(\Omega) Y_{L_2}(\Omega) Y_{L_3}^*(\Omega) d\Omega. \quad (3.51)$$

Now, Using Eq. (3.49) and the generalized form of Eq. (3.25) for multiple scattering cells, which is

$$G = G_0 + G_0 \sum_{\alpha} t^{\alpha} G_0 + G_0 \sum_{\alpha} t^{\alpha} G_0 \sum_{\beta \neq \alpha} t^{\beta} G_0 + \dots, \quad (3.52)$$

we obtain the following expression for \mathbf{r} and \mathbf{r}' in the interstitial region near cells m and n , respectively,

$$G(\mathbf{r}, \mathbf{r}') = G_0(\mathbf{r}, \mathbf{r}') + \sum_{m, n} \sum_{L_1, L_2} (-ik)^2 H_{L_1}(\mathbf{r} - \mathbf{R}_m) \tau_{L_1 L_2}^{mn}(E) H_{L_2}(\mathbf{r}' - \mathbf{R}_n). \quad (3.53)$$

$\tau_{LL'}^{mn}(E)$ is called the *scattering path matrix* and denote the matrix elements of the on-the-energy shell part of the scattering matrix, T . It satisfies the following expansion

$$\tau_{LL'}^{mn} = t_{LL'}^m \delta_{mn} + (1 - \delta_{mn}) \sum_{L_1 L_2} t_{LL_1}^m \tilde{G}_{L_1 L_2}(\mathbf{R}_{mn}) t_{L_2 L'}^n + \dots, \quad (3.54)$$

where $\tilde{G}_{L_1 L_2} = -ik G_{L_1 L_2}$. This quantity is more often called the *scattering path operator*, but it is not technically an operator, since it is defined only on the energy shell. It satisfies the equation of motion, Eq(3.29), in the following form,

$$\tau_{LL'}^{mn} = t_{LL'}^m \delta_{mn} + \sum_{k \neq m} \sum_{L_1 L_2} t_{LL_1}^m \tilde{G}_{L_1 L_2}(\mathbf{R}_{mk}) \tau_{L_2 L'}^{kn}, \quad (3.55)$$

or in angular momentum representation,

$$\underline{\tau}^{mn} = \underline{t}^m \left[\delta_{mn} + \sum_{k \neq m} \underline{\tilde{G}}(\mathbf{R}_{mk}) \underline{\tau}^{kn} \right]. \quad (3.56)$$

3.5. MST for Muffin-tin Potentials

where the *underline* notation denotes the quantity in L space. Comparing with Eq. (3.31), it can be seen that

$$\underline{\tau}^{mn} = [\underline{M}^{-1}]^{mn}, \quad (3.57)$$

where the matrix \underline{M} is the angular momentum representation of M in Eq. (3.31) which is

$$\underline{M}^{ij} = \underline{m}^i \delta_{ij} - \underline{\tilde{G}}(\mathbf{R}_{ij})(1 - \delta_{ij}). \quad (3.58)$$

Eq. (3.57) forms the basis for electronic structure calculations of a translationally invariant material. Consider a simple case in which N identical muffin-tin scatterers are arranged on the sites of a simple Bravais lattice, so that $\underline{t}^i = t$ for all i . Then the Fourier transform of $\underline{\tau}$ and $\underline{\tilde{G}}$ is obtained from following relations,

$$\underline{\tau}(\mathbf{k}) = \frac{1}{N} \sum_{m,n} e^{i\mathbf{k}\cdot(\mathbf{R}_m - \mathbf{R}_n)} \underline{\tau}_{mn}, \quad (3.59)$$

$$\begin{aligned} \underline{\tau}^{mn} &= \frac{1}{N} \sum_{\mathbf{k}} e^{-i\mathbf{k}\cdot(\mathbf{R}_m - \mathbf{R}_n)} \underline{\tau}(\mathbf{k}) \\ &= \frac{1}{\Omega_{BZ}} \int_{BZ} d^3k e^{-i\mathbf{k}\cdot(\mathbf{R}_m - \mathbf{R}_n)} \underline{\tau}(\mathbf{k}), \end{aligned} \quad (3.60)$$

and

$$\underline{\tilde{G}}(\mathbf{k}) = \frac{1}{N} \sum_{m,n} e^{i\mathbf{k}\cdot(\mathbf{R}_m - \mathbf{R}_n)} \underline{\tilde{G}}(\mathbf{R}_{mn}). \quad (3.61)$$

From Eq. (3.58) we obtain

$$\underline{\tau}(\mathbf{k}) = \left[\underline{m} - \underline{\tilde{G}}(\mathbf{k}) \right]^{-1}. \quad (3.62)$$

Here $\underline{m} = \underline{t}^{-1}$ depends on the energy and potential of a cell, whereas $\underline{\tilde{G}}$, the *KKR structure constants*, depend on the energy and structure of the lattice. The eigenvalues, $E(\mathbf{k})$, can be obtained from the solution of the so-called *secular equation*,

$$\det|\underline{\tau}(\mathbf{k})| = \det \left| \underline{m} - \underline{\tilde{G}}(\mathbf{k}) \right| = 0. \quad (3.63)$$

In this equation, the matrix dimension labeled by angular momentum index, $L \equiv \{l, m\}$, is in principle infinite. However, in real applications, l is truncated at some reasonably small number.

In the next chapter, we will review how MST is used in exact muffin-tin orbital theory.

Chapter 4

Exact Muffin-tin Orbital Theory

Originally, Kohn and Rostoker formulated a general variational principle in terms of a Green's function of a system [13]. However, to make practical calculations with it they had to use a simplified muffin-tin potential, which resulted in the same set of equations as the one proposed independently by Korringa [12]. A muffin-tin potential approximates a realistic (full) potential by a set of non-overlapping spherically symmetric wells centered at atomic sites separated by a constant interstitial potential. This approximation has been the foundation for various practical implementations of the KKR formalism. In particular, O. K. Andersen has introduced the notion of screened muffin-tin orbitals (MTO). These are functions that form a complete basis for a muffin-tin potential. They are also short-ranged, which results in short-ranged structure constants, making real-space KKR calculations possible. With an additional constraint of energy-independent structure constants this basis set was used to implement the atomic-sphere approximation (ASA) of KKR equations [60, 61].

Despite the success of the muffin-tin KKR methods it is clear that the non-overlapping atomic spheres give only a crude description of a realistic potential. Therefore, various generalizations have been put forward. Among them is an improved version of MTOs proposed by O. K. Andersen [18]. He pointed out that a much better approximation of a realistic potential can be achieved by overlapping spherical potentials. As a suitable basis he introduced a set of short-ranged functions referred to as exact muffin-tin orbitals (EMTO) (sometimes called "third-generation MTOs" [62]) that can be utilized for solving both the

Kohn-Sham as well as the Poisson equations. A Green's function method based on this basis set was implemented in the EMTO-CPA (coherent-potential approximation) code [19–21] suitable for modeling disordered systems. In this chapter we shall review the basic concepts of this theory as well as some computational techniques implemented in this code.

4.1 EMTO Basis Set

Although the EMTO-CPA code is based on the Green's function method, it is more convenient to present the formalism in terms of matching of scattering waves at atomic spheres. Here, the basic concepts of the formalism are reviewed. For more details, we refer to the book by L. Vitos [20].

Using Rydberg atomic units, Eq. (2.22) can be rewritten in the following form:

$$[-\nabla^2 + v(\mathbf{r})] \Phi_i(\mathbf{r}) = \epsilon_i \Phi_i(\mathbf{r}). \quad (4.1)$$

The potential is approximated as follows:

$$v(\mathbf{r}) \approx v_{mt}(\mathbf{r}) = v_0 + \sum_R [v_R(r_R) - v_0], \quad (4.2)$$

where $v_R(r_R)$ are overlapping spherical symmetric potentials centered on lattice sites \mathbf{R} with radii s_R and $r_R = |\mathbf{r} - \mathbf{R}|$, and v_0 is the so-called muffin-tin zero potential, constant potential in the interstitial region. v_R and v_0 are determined by minimizing the mean of the squared deviation between $v_{mt}(\mathbf{r})$ and $v(\mathbf{r})$ which is obtained by

$$F_v[\{v_R\}, v_0] = \int \left\{ v(\mathbf{r}) - v_0 - \sum_R [v_R(r_R) - v_0] \right\}^2 d\mathbf{r}. \quad (4.3)$$

Minimizing F_v will lead to the following conditions,

$$\int \delta v_R(\mathbf{r}) \frac{\delta F_v[\{v_R\}, v_0]}{\delta v_R(\mathbf{r})} d\mathbf{r} = 0 \quad \text{for any } R, \quad (4.4)$$

and

$$\frac{\partial F_v[\{v_R\}, v_0]}{\partial v_0} = 0. \quad (4.5)$$

The optimal values for v_0 and $v_R(r_R)$, which are the solution of Eq. (4.4) and Eq. (4.5), form the so-called *optimized overlapping muffin-tin* potential.

In order to solve Eq. (4.1), the Kohn-Sham orbitals, $\Phi_i(\mathbf{r})$, are expanded in terms of a complete basis set, called *exact muffin-tin orbitals*, $\bar{\Psi}_{RL}^a(\epsilon_i, \mathbf{r}_R)$, as follows

$$\Phi_i(\mathbf{r}) = \sum_{RL} \bar{\Psi}_{RL}^a(\epsilon_i, \mathbf{r}_R) u_{RL,i}^a, \quad (4.6)$$

where $L \equiv \{l, m\}$ and $u_{RL,i}^a$ are the expansion coefficients. In practice, the summation on l is truncated at a maximum value called l_{max} . In most cases, $l_{max} = 3$, *i.e.*, a *spdf* basis set, is sufficient to have proper results.

The basis functions which are used for constructing $\bar{\Psi}_{RL}^a(\epsilon_i, \mathbf{r}_R)$ are referred to as *screened spherical waves* (SSW) for the interstitial region, and *partial waves* for the region inside the muffin-tin spheres. We shall now take a look at these functions.

4.1.1 Screened Spherical Waves

The potential inside the interstitial region, which is the space between the hard spheres, is v_0 . For this region, Eq. (4.1) can be rewritten as:

$$[\nabla^2 + \kappa^2] \psi_{RL}^a(\kappa^2, \mathbf{r}_R) = 0, \quad (4.7)$$

where $\kappa^2 = \epsilon - v_0$. The solutions for above equation are well known, but a proper choice for $\psi_{RL}^a(\kappa^2, \mathbf{r}_R)$ should follow two considerations. Firstly, every single $\psi_{RL}^a(\kappa^2, \mathbf{r}_R)$ must be attached to a corresponding partial wave, and secondly, they must be well-localized for energies of interest, so that they can be easily calculated in real space. Since the potential spheres overlap, in order to specify these conditions, at each site \mathbf{R} , a *screening sphere* (or *a-sphere*) with radius a_R is centered. These spheres are defined to be non-overlapping and the following boundary condition is imposed at them,

$$\begin{aligned} \psi_{R'L}^a(\kappa^2, \mathbf{r}_R = a_{R'}) &= Y_L(\hat{\mathbf{r}}_R) & \text{if } \mathbf{R}' = \mathbf{R} \\ \psi_{R'L}^a(\kappa^2, \mathbf{r}_R = a_{R'}) &= 0 & \text{if } \mathbf{R}' \neq \mathbf{R}. \end{aligned} \quad (4.8)$$

This means that every SSW should vanish on all screening spheres except for the one at its own site \mathbf{R} on which it equals the real harmonic $Y_L(\hat{\mathbf{r}}_R)$ ¹. Now, it is possible to expand the SSW related to the interstitial region of site \mathbf{R} in terms

¹For the convention used for the real harmonics and Bessel and Neumann functions see Appendix B of Ref. [20]

of real harmonics around any site \mathbf{R}' as:

$$\begin{aligned} \psi_{RL}^a(\kappa^2, \mathbf{r}_R) &= f_{RL}^a(\kappa^2, r_R) Y_L(\hat{\mathbf{r}}_R) \delta_{RR'} \delta_{LL'} \\ &+ \sum_{L'} g_{R'L'}^a(\kappa^2, r_{R'}) Y_{L'}(\hat{\mathbf{r}}_{R'}) S_{R'L'RL}^a(\kappa^2), \end{aligned} \quad (4.9)$$

where the expansion coefficients $S_{R'L'RL}^a(\kappa^2)$ are the elements of a *screened structure constant* matrix. It is also known as *slope matrix* within EMTO theory and will be discussed in the next chapter. Furthermore, f_{RL}^a and g_{RL}^a are called the *value* (or *head*) and the *slope* (or *tail*) functions, respectively. They are defined in terms of spherical Bessel, j_l , and Neumann, n_l , functions¹, as follows:

$$\begin{aligned} f_{RL}^a(\kappa^2, r_R) &= t_{RL}^1(\kappa^2) n_l(\kappa^2, r) + t_{RL}^2(\kappa^2) j_l(\kappa^2, r), \\ g_{RL}^a(\kappa^2, r_R) &= -t_{RL}^3(\kappa^2) n_l(\kappa^2, r) - t_{RL}^4(\kappa^2) j_l(\kappa^2, r), \end{aligned} \quad (4.10)$$

where the coefficients $t_{RL}^{1, \dots, 4}$ are called screening parameters. In addition, from the boundary conditions in Eq. (4.8), we have

$$f_{RL}^a(a_R) = 1 \quad , \quad g_{RL}^a(a_R) = 0. \quad (4.11)$$

Finally in order to completely specify t^1, \dots, t^4 , we make the following choices for their radial slope on the a -spheres,

$$\left. \frac{\partial f_{RL}^a(\kappa^2, r_R)}{\partial r_R} \right|_{a_R} = 0 \quad , \quad \left. \frac{\partial g_{RL}^a(\kappa^2, r_R)}{\partial r_R} \right|_{a_R} = \frac{1}{a_R}. \quad (4.12)$$

Using conditions (4.11) and (4.12) we can find t^1, \dots, t^4 at all sites and for all l ,

$$\begin{Bmatrix} t_{RL}^1(\kappa^2) & t_{RL}^2(\kappa^2) \\ t_{RL}^3(\kappa^2) & t_{RL}^4(\kappa^2) \end{Bmatrix} = 2 \frac{a_R^2}{w} \begin{Bmatrix} \frac{\partial j_l(\kappa^2, a_R)}{\partial r_R} & - \frac{\partial n_l(\kappa^2, a_R)}{\partial r_R} \\ \frac{1}{a_R} j_l(\kappa^2, a_R) & - \frac{1}{a_R} n_l(\kappa^2, a_R) \end{Bmatrix} \quad (4.13)$$

where w is the Wigner-Seitz radius.

In Eq. (4.9), $l \leq l_{max}$ and the l' summation is infinite. In practice the SSWs are not enforced to vanish exactly on each screening sphere. Rather it is required that the tail function at a -spheres vanish up to $l' = l_{max}$. Therefore, in order to have the slope matrices finite-sized, the l' summation is truncated at $l_{max}^h \approx 8 - 12$, and for $l' \geq l_{max}$, the tail function reduces to the Bessel function, *i.e.*, $g_{R'L'}^a(\kappa^2, r_{R'}) = -j_l(\kappa^2, r_{R'})$. This means that the SSWs are allowed to penetrate the a -spheres for $l' \geq l_{max}$.

4.1.2 Partial Waves

The potential inside the muffin-tin spheres, $v_R(r)$, is spherically symmetric and the corresponding solution of the Schrödinger equation, referred to as partial

Chapter 4. Exact Muffin-tin Orbital Theory

waves, can be written as

$$\phi_{RL}^a(\epsilon, \mathbf{r}_R) = N_{RL}^a(\epsilon) \phi_{RL}(\epsilon, r_R) Y_L(\hat{\mathbf{r}}_R), \quad (4.14)$$

where $N_{RL}^a(\epsilon)$ are the normalization functions and will be determined from the matching condition. The functions $\phi_{RL}(\epsilon, r_R)$ are the regular solutions of the radial Schrödinger equation,

$$\frac{\partial^2 [r_R \phi_{RL}(\epsilon, r_R)]}{\partial^2 r_R} = \left[\frac{l(l+1)}{r_R^2} + v_R(r_R) - \epsilon \right] r_R \phi_{RL}(\epsilon, r_R). \quad (4.15)$$

In practice, instead of the non-relativistic Schrödinger equation above, the Dirac equation is solved numerically within the *scalar relativistic approximation*. For more details, see Ref. [62].

The partial waves are defined for $r_R \leq s_R$. Since a SSW behaves like real harmonics only on its own screening sphere, the matching condition should be arranged at this sphere. As a result, it is natural to conclude that the screening spheres should be equal to the potential spheres, $a_R = s_R$. But this would bring problems such as difficulties in boundary conditions of SSWs or poor localization of the resulting SSWs [62]. On the other hand, making the potential spheres smaller will result in a poor muffin-tin approximation for the potential. This dilemma is solved by introducing a new additional free-electron wave that joins continuously and differentiable to the partial waves at s_R and continuously to the SSW at a_R . It is called a *backward extrapolated free-electron solution* with the following form,

$$\varphi_{RL}^a(\epsilon, r_R) = f_{RL}^a(\kappa^2, r_R) + g_{RL}^a(\kappa^2, r_R) D_{RL}^a(\epsilon), \quad (4.16)$$

where $D_{RL}^a \equiv \mathcal{D} \{ \varphi_{RL}^a(\epsilon, a_R) \}$ is the logarithmic derivative of $\varphi_{RL}^a(\epsilon, r_R)$ at $r_R = a_R$. By definition, the logarithmic derivative of a function $f(r_R)$ at r_R^0 is

$$\mathcal{D} \{ f(r_R^0) \} = \frac{r_R^0}{f(r_R^0)} \frac{\partial f(r_R)}{\partial r_R} \Big|_{r_R=r_R^0}. \quad (4.17)$$

The matching condition at the potential spheres leads to

$$N_{RL}^a(\epsilon) \phi_{RL}(\epsilon, s_R) = \varphi_{RL}^a(\epsilon, s_R), \quad (4.18)$$

and

$$N_{RL}^a(\epsilon) \frac{\partial \phi_{RL}(\epsilon, r_R)}{\partial r_R} \Big|_{r_R=s_R} = \frac{\partial \varphi_{RL}^a(\epsilon, r_R)}{\partial r_R} \Big|_{r_R=s_R}. \quad (4.19)$$

Rearranging these two equations leads to the following equations for the normalization functions and logarithmic derivative, respectively,

$$N_{RL}^a(\epsilon) = \left[\frac{\phi_{RL}(\epsilon, s_R)}{f_{RL}^a(\kappa^2, s_R)} \frac{\mathcal{D}_\phi - \mathcal{D}_g}{\mathcal{D}_f - \mathcal{D}_g} \right]^{-1}, \quad (4.20)$$

4.2. Kink Cancellation Equation and the Path Operator

and

$$D_{RL}^a(\epsilon) = -\frac{f_{RL}^a(\kappa^2, s_R)}{g_{RL}^a(\kappa^2, s_R)} \frac{\mathcal{D}_\phi - \mathcal{D}_f}{\mathcal{D}_\phi - \mathcal{D}_g}, \quad (4.21)$$

where we have used the abbreviations $\mathcal{D}_\phi = \mathcal{D}\{\phi_{RL}(\epsilon, s_R)\}$, $\mathcal{D}_f = \mathcal{D}\{f_{RL}^a(\epsilon, s_R)\}$ and $\mathcal{D}_g = \mathcal{D}\{g_{RL}^a(\epsilon, s_R)\}$ for simplicity.

Now that the basis set is complete, one can build the exact muffin-tin orbitals as

$$\begin{aligned} \bar{\Psi}_{RL}^a(\epsilon, \mathbf{r}_R) = & \psi_{RL}^a(\kappa^2, \mathbf{r}_R) + N_{RL}^a(\epsilon)\phi_{RL}(\epsilon, r_R)Y_L(\hat{\mathbf{r}}_R) \\ & - \varphi_{RL}^a(\epsilon, r_R)Y_L(\hat{\mathbf{r}}_R). \end{aligned} \quad (4.22)$$

The radial part of the second terms is truncated outside the potential spheres. In the same way, since $\varphi_{RL}^a(\epsilon, r_R)$ is defined only for $a_R \leq r_R \leq s_R$, the radial part of the third term is truncated outside this region.

4.2 Kink Cancellation Equation and the Path Operator

The exact muffin-tin orbital, $\bar{\Psi}_{RL}^a(\epsilon, \mathbf{r}_R)$, is continuous everywhere in space, but has a kink (i.e, a discontinuous slope) at every a -sphere. It is customary to define the *kink matrix*, K^a , such that $K_{R'L'RL}^a = a_R^2 \times (\text{kink at } R' \text{ in the } L' \text{ projection of } \bar{\Psi}_{RL}^a)$. One can see from the above equations that

$$\begin{aligned} K_{R'L'RL}^a &= -a_R S_{R'L'RL}^a(\kappa^2) & \text{for } R' \neq R, L' \neq L, l' \leq l_{max}, \\ K_{R'L'RL}^a &= a_R D_{RL}^a(\epsilon) - a_R S_{RLRL}^a(\kappa^2) & \text{for } R' = R, L' = L, l' \leq l_{max}. \end{aligned} \quad (4.23)$$

Therefore, the *kink matrix* can be expressed as follows,

$$K_{R'L'RL}^a(\epsilon_i) \equiv a_{R'} S_{R'L'RL}^a(\kappa_i^2) - \delta_{R'R} \delta_{L'L} a_R D_{RL}^a(\epsilon_i) \quad (4.24)$$

The exact muffin-tin orbital would be an eigenfunction of the Schrödinger equation for the whole muffin-tin potential if the kinks disappear. This means that the Kohn-Sham orbitals, $\Phi_i(\mathbf{r})$, can be written as a superposition of $\bar{\Psi}_{RL}^a(\epsilon_i, \mathbf{r}_R)$ in Eq. (4.6), as long as the kinks of all individual $\bar{\Psi}_{RL}^a(\epsilon_i, \mathbf{r}_R)$ cancel each other. This can be written in following form,

$$\sum_{RL} K_{R'L'RL}^a(\epsilon_i) u_{RL,i}^a = 0, \quad (4.25)$$

which is known as *kink cancellation equation* and its solutions are the Kohn-Sham energies and wave functions.

Chapter 4. Exact Muffin-tin Orbital Theory

The kink cancellation equation can be considered equivalent to the secular equation in the KKR method, which was discussed in previous chapter. Although it is solved in a Hamiltonian based formalism in LMTO method, a Green's function based technique is used in EMTO theory to find the solutions, which makes it possible to apply this method to disordered systems. The kink cancellation equation can be solved using the *path operator*, $g_{R'L'RL}^a(z, \mathbf{k})$. It is defined in \mathbf{k} space for a complex energy z as follows:

$$\sum_{R''L''} K_{R'L'R''L''}^a(z, \mathbf{k}) g_{R''L''RL}^a(z, \mathbf{k}) = \delta_{RR'} \delta_{LL'}. \quad (4.26)$$

Each pole of the path operator corresponds to a single state. Therefore, since $g^a(z)$ is analytical for complex z , one can use the residue theorem to find the total number of states. It is, thus, important that the path operator is properly normalized with the overlap of the basis functions. Using the equations in the previous section together with Green's second theorem, one can show that the overlap is given by [20]

$$\begin{aligned} \int \bar{\Psi}_{RL}^{a*}(\epsilon, \mathbf{r}_R) \bar{\Psi}_{RL}^a(\epsilon, \mathbf{r}_R) d\mathbf{r}_R &= a_R \dot{S}_{R'L'RL}^a(\kappa^2) - a_R \dot{D}_{RL}^a(\epsilon) \\ &= \dot{K}_{R'L'RL}^a(\epsilon) \end{aligned} \quad (4.27)$$

where the dots represent derivatives with respect to energy. Consequently, the total number of states below the Fermi level can be obtained from the following expression:

$$N(\epsilon_F) = \frac{1}{2\pi i} \oint_{\epsilon_F} G(z) dz, \quad (4.28)$$

where

$$\begin{aligned} G(z) &= \sum_{R'L'RL} g_{R'L'RL}^a(z) \dot{K}_{R'L'RL}^a(z) \\ &\quad - \sum_{RL} \left(\frac{\dot{D}_{RL}^a(z)}{D_{RL}^a(z)} - \sum_{\epsilon_{RL}^D} \frac{1}{[z - \epsilon_{RL}^D]} \right), \end{aligned} \quad (4.29)$$

is the Green's function of the system with $l, l' \leq l_{max}$. It is worth noting that the first term in the second summation is needed to remove the unphysical poles of \dot{K} and the second term acts to restore the poles of $\dot{D}(z)/D(z)$ which are due to the zeros of the logarithmic derivative function and denoted here by ϵ_{RL}^D . It is clear that if $\dot{D}^a(z)$ has no poles in the energy range of interest, these terms have no contribution to density of state.

Applying Eqs. (4.28) and (4.29), one can calculate $N(\epsilon_F^*)$ for a series of ϵ_F^* and then obtain the correct ϵ_F from Eq. (3.17), ensuring that the total number of states $N(\epsilon_F)$ is equal to the number of electrons N_e .

4.3 Electron Density

For calculating the electron density within the EMTO theory, the total density $n(\mathbf{r})$ is obtained from

$$n(\mathbf{r}) = \sum_R n_R(\mathbf{r}_R), \quad (4.30)$$

where $n(\mathbf{r}_R)$ is the electron density defined inside the Wigner-Seitz cell around site R . These density components can be expanded in terms of real harmonics as follows

$$n_R(\mathbf{r}_R) = \sum_L n_{RL}(r_R) Y_L(\hat{\mathbf{r}}_R). \quad (4.31)$$

It can be shown that the partial components $n_{RL}(r_R)$ can be obtained using the residue [20],

$$n_{RL}(r_R) = \frac{1}{2\pi i} \oint_{\epsilon_F} \sum_{L''L'}^{l_{max}} C_{LL'L''} Z_{RL''}^a(z, r_R) \tilde{g}_{RL''RL'}^a(z) Z_{RL'}^a(z, r_R) dz, \quad (4.32)$$

where $C_{LL'L''}$ are the real gaunt numbers introduced in previous chapter. $Z_{RL}^a(z, r_R)$ and $\tilde{g}_{RL'L}^a(z)$, which is called the generalized path operator, are calculated from the following equations,

$$Z_{RL}^a(z, r_R) = \begin{cases} N_{RL}^a(z) \phi_{RL}(z, r_R) & l \leq l_{max}, r_R \leq s_R, \\ \varphi_{RL}^a(z, r_R) & l \leq l_{max}, r_R > s_R, \\ -j_l(\kappa r_R) & l > l_{max}, \text{ for all } r_R, \end{cases} \quad (4.33)$$

and

$$\tilde{g}_{RL'RL}^a = \begin{cases} g_{RL'RL}^a + \frac{\delta_{L'L}}{a_R \dot{D}_{RL}^a} \left(\frac{\dot{D}_{RL}^a}{D_{RL}^a} - \sum_{\epsilon_{RL}^D} \frac{1}{z - \epsilon_{RL}^D} \right) & l, l' \leq l_{max}, \\ \sum_{R''L''} g_{RL'R''L''}^a a_{R''} S_{R''L''RL}^a & l' \leq l_{max}, l > l_{max}, \\ \sum_{R''L''} g_{RL'R''L''}^a S_{R''L''RL}^a & l' > l_{max}, l \leq l_{max}, \\ \sum_{R''L''R'''L'''} S_{RL'R''L''}^a g_{R''L''R'''L'''}^a a_{R'''} S_{R'''L'''RL}^a & l', l > l_{max}. \end{cases} \quad (4.34)$$

where the energy dependence has been suppressed for simplicity. The first line of Eq. (4.34) is the low- l block, the next two are off-diagonal blocks and the last one is the high- l block of the generalized path operator matrix. It is worth noting that since the partial components in Eq. (4.31) for $l > l_{max}^h$ are very small, the summation over l is truncated at l_{max}^h . This means that the low- l and off-diagonal blocks of the slope matrix and their first energy derivatives are needed to be calculated. This will be discussed in the next chapter.

4.4 Single-electron Potential

The final task to complete the self-consistent cycle of solving Kohn-Sham equations is to create the single-electron potential for the next iteration. To this end, one can calculate the full potential from the calculated charge density, as described in previous section, and then build the optimized overlapping muffin-tin wells using Eqs. (4.4) and (4.5). Instead of using relevant equations including integrals over real space, the Poisson equation can be solved approximately within the *spherical cell approximation* (SCA) [22].

The SCA involves two approximations. First, in Eq. (4.3) the Wigner-Seitz cell around each lattice site is replaced by a spherical cell with the volume equal to the volume of the real cell and second, $v_R(r_R)$ is approximated by the spherical average of the full-potential,

$$v_R(r_R) = \frac{1}{4\pi} \int_{r_R \leq s_R} v(\mathbf{r}) d\hat{\mathbf{r}}. \quad (4.35)$$

The muffin-tin constant v_0 is fixed to the average of the full potential in the interstitial. It can be shown that within the SCA, v_0 can be obtained from the following equation [22]

$$v_0 = \frac{\sum_R \int_{s_R}^{w_R} r^2 [\int v(\mathbf{r}) d\hat{\mathbf{r}}] dr_R}{\sum_R [4\pi (w_R^3 - s_R^3) / 3]} \quad (4.36)$$

where w_R is the radius of the spherical cell for site R . Therefore, the main consequence of the SCA is that both $v_R(r_R)$ and v_0 are obtained by the spherically symmetric part of the full potential.

For calculating $v_R(r_R)$, the potential is divided into different parts as follows

$$v(\mathbf{r}) = v^C(\mathbf{r}) + v_{xc}([n]; \mathbf{r}), \quad (4.37)$$

where v_{xc} is the exchange-correlation energy and $v^C(\mathbf{r})$ is the electrostatic part of the potential satisfying the Poisson equation,

$$\nabla^2 v^C(\mathbf{r}) = -8\pi \left[n(\mathbf{r}) + \sum_R Z_R \delta(r_R) \right] \quad (4.38)$$

for the electronic and nuclear charge densities. The spherical symmetric part of v_{xc} is found by

$$v_R^{xc}(r_R) = \frac{1}{4\pi} \int v_{xc}([n_R]; \mathbf{r}_R) d\hat{\mathbf{r}}_R, \quad (4.39)$$

4.4. Single-electron Potential

and the spherically symmetric part of v^C is found from the solution of the Poisson equation and can be divided into contributions from the inside and outside of potential sphere. Here, we only introduce the final equations. More details can be found in the book by J. D. Jackson [65].

The intra-cell part of the electrostatic potential can be written as

$$v_R^I(\mathbf{r}_R) = -\frac{2Z_R}{r_R} + 2 \int_{\Omega_R} \frac{n_R(\mathbf{r}'_R)}{|\mathbf{r}_R - \mathbf{r}'_R|} d\mathbf{r}'_R \quad (4.40)$$

It can be shown that the spherical symmetric part of the above equation can be written as

$$\begin{aligned} v_R^I(r_R) &= \frac{1}{4\pi} \int v_R^I(\mathbf{r}_R) d\hat{\mathbf{r}}_R \\ &= \frac{8\pi}{r_R} \int_0^{r_R} r'^2 n_{RL_0}(r'_R) dr'_R + 8\pi \int_{r_R}^{s_R} r'_R n_{RL_0}(r'_R) dr'_R - \frac{2Z_R}{r_R}, \end{aligned} \quad (4.41)$$

where $n_{RL_0} = n_{RL=\{0,0\}}$. The inter-cell contribution gives the Madelung potential,

$$v_R^M(\mathbf{r}_R) = - \sum_{R \neq R'} \frac{2Z_{R'}}{|\mathbf{r}_{R'} + \mathbf{R}'|} + \sum_{R \neq R'} 2 \int_{\Omega_{R'}} \frac{n_{R'}(r_{R'})}{|\mathbf{r}_R - \mathbf{r}_{R'} + \mathbf{R} - \mathbf{R}'|} d\mathbf{r}_{R'}, \quad (4.42)$$

and the final equation is given by

$$v_R^M(r_R) = \frac{1}{4\pi} \int v_R^M(\mathbf{r}_R) d\hat{\mathbf{r}}_R = \frac{1}{w} \sum_{R' \neq R, L'} M_{RL_0 R' L'} Q_{R' L'}^{SCA}. \quad (4.43)$$

Here,

$$\begin{aligned} M_{RL_0 R' L'} &= 8\pi(-1)^{l'} \sum_{L''} C_{LL'L''} \frac{(2l'' - 1)!!}{(2l - 1)!!(2l' - 1)!!} \delta_{l'', l'+l} \\ &\quad \times \left(\frac{w}{|\mathbf{R}' - \mathbf{r}|} \right)^{l''+1} Y_{L''}(\widehat{\mathbf{R}' - \mathbf{r}}) \end{aligned} \quad (4.44)$$

are the elements of the Madelung matrix and w is the average Wigner-Seitz radius. The multipole moments, $Q_{R' L'}^{SCA}$, are calculated within the SCA as

$$Q_{R' L'}^{SCA} = \frac{\sqrt{4\pi}}{2l+1} \int_0^{w_R} \left(\frac{r_R}{w} \right)^l n_{RL}(r_R) r_R^2 dr_R - Z_R \delta_{L, L_0} + \delta^{SCA} \delta_{L, L_0}, \quad (4.45)$$

where δ^{SCA} is a site independent constant which is added to the above equation to have charge neutrality in the unit cell. This is necessary because the charge

density described in the previous section is normalized within the unit cell, but since the integral in above equation is done over the spherical cell, the charge density has to be renormalized within the spherical cell. Thus, the δ^{SCA} is determined by $\sum_R Q_{RL_0}^{SCA} = 0$. As a consequence of the SCA, the number of electrons inside the s -sphere

$$Q(s_R) = \frac{\sqrt{4\pi}}{2l+1} \int_0^{s_R} n_{RL}(r_R) r_R^2 dr_R, \quad (4.46)$$

is different from the number of electrons inside the unit cell, $Q_{RL_0}^{SCA} + Z_R$. The contribution of this missing charge to the potential is taken into account using equal redistribution of this charge over the N_{NN} nearest-neighbor cells, which can be expressed as

$$\Delta v_R^{SCA} \approx \frac{0.55}{w} \Delta Q_{R_{NN}}, \quad (4.47)$$

where $\Delta Q_{R_{NN}} = \frac{1}{N_{NN}} [Q_{RL_0}^{SCA} + Z_R - Q(s_R)]$ and R_{NN} are the nearest-neighbor sites. With this, the total potential within the potential sphere is obtained as

$$v_R(r_R) = v_R^I(r_R) + v_R^M(r_R) + \Delta v_R^{SCA} + v_R^{xc}(r_R). \quad (4.48)$$

4.5 Full Charge Density Technique

The simplifications of the full one-electron potential made within the SCA is usually too drastic to provide accurate results compared to the full-potential methods. For instance, such an inaccuracy is notable for properties related to energetics of structural relaxations, such as elastic constants. The required deformations necessary for calculating such properties decrease the symmetry of the system and therefore, the results are strongly dependent on the non-spherical symmetric part of the potential which is missing in the SCA approximation.

In order to improve the accuracy, the *full charge density* (FCD) technique is used in EMTO-based methods [23, 24, 66]. In this technique, the total energy is calculated from relevant equations involving integrals of the total charge density over the Wigner-Seitz cell. The total charge density is taken from a converged self-consistent SCA-EMTO calculation. The technique used for volume integration over the Wigner-Seitz cell is called the *shape function technique* [66, 67]. First, we will shortly review this integration technique and then will come back to the FCD technique.

4.5.1 Shape Function Technique

The shape function technique is a numerical method for performing volume integrals over any arbitrary polyhedra. Using this technique, any integral over a cell is transformed into an integral over a sphere circumscribing the cell. The shape function is a 3-D step-function defined as

$$\sigma_R(\mathbf{r}_R) = \begin{cases} 1 & \text{if } \mathbf{r}_R \in \Omega_R, \\ 0 & \text{otherwise,} \end{cases} \quad (4.49)$$

where Ω_R is the Wigner-Seitz cell at R . The shape function can be expanded in terms of real harmonics as

$$\sigma_R(\mathbf{r}_R) = \sum_L \sigma_{RL}(r_R) Y_L(\hat{\mathbf{r}}_R), \quad (4.50)$$

where

$$\sigma_{RL}(r_R) = \int \sigma_R(\mathbf{r}_R) Y_L(\hat{\mathbf{r}}_R) d\hat{\mathbf{r}}_R \quad (4.51)$$

are the partial components of the shape function. Once they are evaluated for the Wigner-Seitz cell, the integral over any arbitrary functional of the electron density, $K([n]; \mathbf{r})$, over the Ω_R can be transformed into an integral over the smallest circumscribed sphere with radius s_R^c centered on lattice site R . This can be expressed as

$$\int_{\Omega_R} n(\mathbf{r}_R) K([n]; \mathbf{r}_R) d\mathbf{r}_R = \int_{s_R^c} \sigma_R(\mathbf{r}_R) n_R(\mathbf{r}_R) K([n]; \mathbf{r}_R) d\mathbf{r}_R, \quad (4.52)$$

where the functions $\sigma_R(\mathbf{r}_R) n_R(\mathbf{r}_R)$ can be expanded in terms of real harmonics, *viz.*

$$\sigma_R(\mathbf{r}_R) n_R(\mathbf{r}_R) = \sum_L \tilde{n}_{RL}(r_R) Y_L(r_R). \quad (4.53)$$

The radial function $\tilde{n}_{RL}(r_R)$ can be expressed in terms of partial components $\sigma_{RL}(r_R)$ as follows,

$$\tilde{n}_{RL}(r_R) = \sum_{L', L''} C_{LL'L''} n_{RL'}(r_R) \sigma_{RL''}(r_R), \quad (4.54)$$

where $C_{LL'L''}$ are the real Gaunt coefficients. Finally, Eq. (4.52) can be rewritten as

$$\int_{\Omega_R} n(\mathbf{r}_R) K([n]; \mathbf{r}_R) d\mathbf{r}_R = \sum_L \int_0^{s_R^c} \tilde{n}_{RL}(r_R) K_L(r_R) r_R^2 dr_R, \quad (4.55)$$

where $K_L(r_R)$ is the $Y_L(\hat{\mathbf{r}}_R)$ projection of $K([n], \mathbf{r}_R)$ on the spherical surface with radius r_R , obtained by

$$K_L(r_R) = \int Y_L(\hat{\mathbf{r}}_R) K([n], \mathbf{r}_R) d\hat{\mathbf{r}}_R. \quad (4.56)$$

To calculate the partial components, $\sigma_{RL}(r_R)$, Eq. (4.51) can be rewritten as

$$\sigma_{RL}(r_R) = \int_{\mathcal{S}_R(r_R)} Y_L(\hat{\mathbf{r}}_R) d\hat{\mathbf{r}}_R, \quad (4.57)$$

where $\mathcal{S}_R(r_R)$ represents that part of the spherical surface of radius r_R which lies inside the Wigner-Seitz cell. It is easy to show that

$$\sigma_{RL}(r_R) = \begin{cases} \sqrt{4\pi} \delta_{l0} & r_R \leq s_R^i, \\ 0 & r_R > s_R^c, \end{cases} \quad (4.58)$$

where s_R^i denotes the inscribed sphere centered at site R .

For $s_R^i < r_R \leq s_R^c$ the Wigner-Seitz cell is divided into tetrahedra. Generally, the Wigner-Seitz cell is a convex polyhedron bounded by N_f polygons and it can be partitioned by taking every polygon as the base of a pyramid with its apex set on the lattice site R . Assuming $N_e(p)$ as the number sides of pyramid p , each pyramid can be subdivided into $N_e(p)$ tetrahedra, using a line drawn from the apex normal to the base. Considering the intersection of this line and the base together with the apex as two common vertices of all tetrahedra, the other vertices of every tetrahedra are two vertices of the base. Therefore, there are $\sum_{p=1}^{N_f} N_e(p)$ tetrahedra, but usually most of them are equivalent. Denoting the number of non-equivalent tetrahedra by N_n and the number of tetrahedra of type t by $N_e(t)$, the total shape function is obtained as

$$\sigma_{RL}(r_R) = \sum_{t=1}^{N_n} \sum_{i=1}^{N_e(t)} \left\{ \sum_{m'} D_{mm'}^l(\alpha_i, \beta_i, \gamma_i) \sigma_{Rlm'}^t(r_R) \right\}, \quad (4.59)$$

where $D_{mm'}^l$ are the matrix elements of finite rotations defined in Appendix B of Ref. [20]. The partial shape functions for the tetrahedron t are obtained by

$$\sigma_{Rlm}^t = \int_{\varphi_{min}^t}^{\varphi_{max}^t} \left\{ \int_{\theta_{min}^t(\varphi)}^{\theta_{max}^t(\varphi)} Y_{lm}(\theta, \varphi) \sin \theta d\theta \right\} d\varphi. \quad (4.60)$$

The last point we mention here is that the l -summation in Eq. (4.50) has to be truncated at a reasonable value which is usually chosen to be $l_{max}^s \approx 30 - 40$.

4.5.2 FCD Total Energy

The *full charge density* technique evaluates the total energy functional in terms of the charge density obtained from Eq. (4.31) for every lattice site after a converged self-consistent cycle of a SCA-EMTO calculation. To achieve this, the total energy is divided into different parts as follows,

$$E_{tot} = T_s[n] + \sum_R (E_R^{intra}[n_R] + E_R^{xc}[n_R]) + E^{inter}[n], \quad (4.61)$$

where $E_R^{intra}[n_R]$ is due to the charges inside a Wigner-Seitz cell and together with $E_R^{xc}[n_R]$ depends only on the charge density within the actual cell, and $E^{inter}[n]$ is the interaction between different cells, which is usually referred to as the Madelung energy.

As we know from Chapter 2, the kinetic energy functional, $T_s[n]$, does not have an explicit form and instead it is calculated using the following expression,

$$T_s[n] = \sum_{\epsilon_i \leq \epsilon_F} \epsilon_i - \int v([n]; \mathbf{r}) n(\mathbf{r}) d\mathbf{r}, \quad (4.62)$$

which in the EMTO formalism leads to

$$T_s[n] = \frac{1}{2\pi i} \oint_{\epsilon_F} z G(z) dz - \sum_R \int_{\Omega_R} v_{mt}(\mathbf{r}_R) n(\mathbf{r}_R) d\mathbf{r}_R, \quad (4.63)$$

where $G(z)$ is expressed in Eq. (4.29) and $v_{mt}(\mathbf{r}_R)$ is the muffin-tin potential. The first term is a sum of the eigenvalues and is calculated by the residue theorem. Using Eq. (4.55), the second term in right-hand side of the above equation can be rewritten as

$$- \sum_R \sqrt{4\pi} \int_0^{s_R^c} v_{mt}(r_R) \tilde{n}_{RL_0}(r_R) r_R^2 dr_R, \quad (4.64)$$

where $\tilde{n}_{RL_0}(r_R)$ are defined in Eq. (4.54). Note that the radial integral in the above equation is divided into two sections, $0 \leq r_R \leq s_R^i$ and $s_R^i \leq r_R \leq s_R^c$.

The exchange-correlation energy is calculated by a three dimensional direct integral over the Wigner-Seitz cell, *i.e.*,

$$\begin{aligned} E_R^{xc}[n_R] &= \int_{\Omega_R} n(\mathbf{r}_R) \varepsilon_{xc}([n]; \mathbf{r}_R) d\mathbf{r}_R \\ &= \int_0^{2\pi} \int_0^\pi \int_0^{s_R^c} n(\mathbf{r}_R) \varepsilon_{xc}([n]; \mathbf{r}_R) \sum_L^{l_{max}} \sigma_{RL}(r_R) Y_L(\hat{\mathbf{r}}_R) r_R^2 dr_R \sin \theta d\theta d\varphi \end{aligned} \quad (4.65)$$

Chapter 4. Exact Muffin-tin Orbital Theory

where $\varepsilon_{xc}([n]; \mathbf{r}_R)$ could be one of the approximations discussed in Section 2.4.

The intra-cell energy part is defined by the following equation,

$$E_R^{intra}[n_R] = \int_{\Omega_R} \int_{\Omega_R} \frac{n_R(\mathbf{r}')n_R(\mathbf{r}_R)}{|\mathbf{r} - \mathbf{r}'|} d\mathbf{r}_R d\mathbf{r}'_R - \int_{\Omega_R} \frac{2Z_R}{r_R} n_R(\mathbf{r}_R) d\mathbf{r}_R. \quad (4.66)$$

Using the shape function and expansion of $\frac{1}{|\mathbf{r} - \mathbf{r}'|}$ in terms of real harmonics [24], one can obtain

$$E_R^{intra}[n_R] = \frac{\sqrt{4\pi}}{w} \sum_L \int_0^{s_R^c} \tilde{n}_{RL}(r_R) \left[\left(\frac{r_R}{w}\right)^l P_{RL}(r_R) + \left(\frac{r_R}{w}\right)^{-l-1} Q_{RL}(r_R) - 2Z_R \frac{w}{r_R} \delta_{LL_0} \right] r_R^2 dr_R \quad (4.67)$$

with

$$P_{RL}(r_R) = \frac{\sqrt{4\pi}}{2l+1} \int_{r_R}^{s_R^c} \tilde{n}_{RL}(r'_R) \left(\frac{r'_R}{w}\right)^{-l-1} (r'_R)^2 dr'_R \quad (4.68)$$

and

$$Q_{RL}(r_R) = \frac{\sqrt{4\pi}}{2l+1} \int_0^{r_R} \tilde{n}_{RL}(r'_R) \left(\frac{r'_R}{w}\right)^l (r'_R)^2 dr'_R. \quad (4.69)$$

The inter-cell energy is the electrostatic energy between different cells and can be expressed by following equation,

$$E^{inter}[n] = \sum_R \sum_{R' \neq R} \left\{ \int_{\Omega_R} \int_{\Omega_{R'}} \frac{n_{R'}(\mathbf{r}')n_R(\mathbf{r}_R)}{|\mathbf{r}_R - \mathbf{r}'_R + \mathbf{R} - \mathbf{R}'|} d\mathbf{r}'_R d\mathbf{r}_R - \int_{\Omega_R} \frac{2Z_{R'}n_R(\mathbf{r}_R)}{|\mathbf{r}_R + \mathbf{R} - \mathbf{R}'|} d\mathbf{r}_R + \frac{Z_R Z_{R'}}{|\mathbf{R} - \mathbf{R}'|} \right\}. \quad (4.70)$$

For non-overlapping spheres, the inter-cell energy is obtained by

$$E_{no}^{inter}[n] = \frac{1}{2w} \sum_{\substack{R, R' \\ R' \neq R}} \sum_{L, L'} Q_{RL} M_{RLR'L'} Q_{R'L'}, \quad (4.71)$$

where $M_{RLR'L'}$ are the Madelung matrix elements defined in Eq. (4.44) and Q_{RL} are the multiple moments calculated using the shape function as

$$Q_{RL} = \frac{\sqrt{4\pi}}{2l+1} \int_0^{s_R^c} \left(\frac{r_R}{w}\right)^l \tilde{n}_{RL}(r_R) r_R^2 dr_R - Z_R \delta_{LL_0}. \quad (4.72)$$

Eq. (4.70) should not be applied for inter-cell energy of overlapping spheres because it causes divergence with increasing l [68, 69]. To treat this problem the so-called *displacement vector*, $\mathbf{b}_{RR'}$, is introduced [68]. The final expression is

$$\begin{aligned}
E_{ov}^{inter}[n] = \frac{1}{2w} \sum_{\substack{R,R' \\ R' \neq R}} \left\{ \sum_L \frac{1}{2L+1} \left(\frac{b_{RR'}}{w} \right)^L Y_L(\hat{\mathbf{b}}_{RR'}) \right. \\
\times \sum_{L',L''} Q_{RL'} \frac{4\pi(2l''-1)!!}{(2l-1)!!(2l'-1)!!} C_{LL'L''} \delta_{l'',l+l'} \\
\left. \times \sum_{L'''} M_{RL''\tilde{R}'L'''} Q_{R'L'''} \right\}, \quad (4.73)
\end{aligned}$$

where $\tilde{\mathbf{R}}' = \mathbf{R}' + \mathbf{b}_{RR'}$, and the displacement vector $\mathbf{b}_{RR'}$ has to satisfy the following inequality,

$$|\mathbf{R} - \mathbf{R}'| + b_{RR'} > s_R^c + s_{R'}^c. \quad (4.74)$$

In order to ensure convergence for increasing l , the displacement vector is obtained from the following equation [69],

$$|\mathbf{R} - \mathbf{R}'| + b_{RR'} = \left(1 + \frac{1}{2\alpha} \right) (s_R^c + s_{R'}^c) \quad (4.75)$$

where the coefficient α is fixed for all neighbors and determined by a condition that ensures the convergence of Eq. (4.73) [69].

4.6 EMTO-CPA method

In order to calculate the electronic structure of random alloys, a Green's function method can be combined with techniques which are developed for this purpose. In particular, the *coherent potential approximation* [14, 15] and the *locally self-consistent Green's function* (LSGF) approach [70, 71] have been implemented within the EMTO method. Here, we only focus on the EMTO-CPA method which is the basis for the code utilized in this thesis.

The problem of calculating the electronic structure of a random substitutional alloy is a classical problem in solid state physics. The CPA is often described as the best single-site solution to this problem, wherein the scattering from a particular site is assumed to be independent of scattering from other sites. It is a mean-field approximation and the main idea is that the random alloy may be replaced by an ordered effective medium such that its parameters are

determined self-consistently. Thus, the translational symmetry of the underlying lattice is kept.

Consider a substitutional alloy with one atom per unit cell and two alloy components, *i.e.* $A_cB_{(1-c)}$, where c is the concentration of atom A . This system is described by the path operator g and the potential m . Figure (3.1) shows the main idea of CPA for such a system. Within the CPA this system is replaced by a mono-atomic configuration described by the site-independent *coherent potential* \tilde{m} and the *coherent path operator* \tilde{g} . Effects of the local environment are neglected in the CPA, which means that the local potentials, here m_A and m_B , around a certain alloy component are the same, independent of its position.

Using an electronic structure formalism such as the KKR method, the relation between \tilde{g} and \tilde{m} is given by

$$\tilde{g} = [S - \tilde{m}]^{-1}, \quad (4.76)$$

where S denotes the structure constant matrix. The path operator of alloy components can be obtained from a single-site Dyson equation:

$$g_i = \tilde{g} + \tilde{g}(m_i - \tilde{m})g_i \quad i = A, B. \quad (4.77)$$

According to the CPA, one can obtain the coherent path operator from path operators of alloy components [19, 20] using

$$\tilde{g} = cg_A + (1 - c)g_B. \quad (4.78)$$

Equations (4.76)-(4.78) are solved iteratively. The extension of these equations to more components is relatively simple.

In the EMTO-CPA method [19], the coherent potential is introduced via the

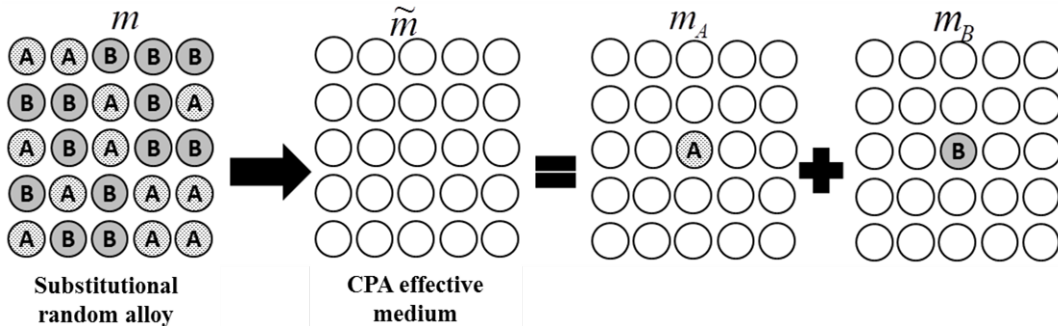


Figure 4.1: Demonstration of the CPA for a substitutional alloy with two alloy components A and B.

4.6. EMTO-CPA method

coherent potential function $\tilde{D}_{RLRL'}(z)$ which can be obtained by

$$\begin{aligned} \sum_{R',L''} a_{R'} \left[S_{R'L'R''L''}(\kappa^2, \mathbf{k}) - \delta_{R'R'} \tilde{D}_{R'L'R''L''}(z) \right] \tilde{g}_{R''L''RL}(z, \mathbf{k}) \\ = \delta_{RR'} \delta_{LL'}. \end{aligned} \quad (4.79)$$

Then one can get the path operator of alloy components from the Dyson equation,

$$\begin{aligned} g_{RLRL'}^i(z) = \tilde{g}_{RLRL'}(z) + \sum_{L'',L'''} \tilde{g}_{RLRL''}(z) \\ \times \left[D_{R''}^i(z) \delta_{L''L'''} - \tilde{D}_{RL''RL'''}(z) \right] g_{R''L''RL'}^i(z), \end{aligned} \quad (4.80)$$

where the $D_{Ri}^i(z)$ is the potential function for the i th alloy component and $\tilde{g}_{RLRL'}(z)$ is obtained by integrating $\tilde{g}_{RLRL'}(z, \mathbf{k})$ over the k space,

$$\tilde{g}_{RLRL'}(z) = \int_{BZ} \tilde{g}_{RLRL'}(z, \mathbf{k}) d\mathbf{k}. \quad (4.81)$$

Finally, the coherent path operator is obtained from

$$\tilde{g}_{RLRL'}(z) = \sum_i c_R^i g_{RLRL'}^i(z), \quad (4.82)$$

where c_R^i is the concentration of the i th alloy component at R . These equations are solved self-consistently for $\tilde{D}(z)$, $\tilde{g}(z, \mathbf{k})$ and $g^i(z)$. The average Green's function of the system is obtained from

$$\begin{aligned} \langle G(z) \rangle = \int_{BZ} \sum_{R'L'RL} \tilde{g}_{R'L'RL}(z, \mathbf{k}) a_R \dot{S}_{RLR'L'}(\kappa^2, \mathbf{k}) d\mathbf{k} \\ - \sum_{R,i} c_R^i \sum_L \left[g_{RLRL}^i(z) a_R \dot{D}_{Ri}^i(z) + \left(\frac{\dot{D}_{Ri}^i(z)}{D_{Ri}^i(z)} - \frac{1}{z - \epsilon_{Ri}^i} \right) \right]. \end{aligned} \quad (4.83)$$

For ordered systems, the above equations reduce to the corresponding equations introduced in Section 4.2. The equations discussed in previous sections for generating the charge density, potential and FCD total energy for ordered systems can be extended to the EMTO-CPA method. The potential within the potential sphere of the i th alloy component on site R is obtained by

$$v_R^i(r_R) = v_R^{I,i}(r_R) + v_R^M + \Delta v_R^{SCA} + v_R^{scr,i} + v_R^{xc,i}(r_R), \quad (4.84)$$

where $v_R^{I,i}$, v_R^M , Δv_R^{SCA} and $v_R^{xc,i}(r_R)$ are obtained from Eqs. (4.41), (4.43), (4.47) and (4.39) respectively using partial components of the charge density of the i th alloy component on site R .

Chapter 4. Exact Muffin-tin Orbital Theory

The expression $v_R^{Scr,i}$ denotes an additional modification which is taken into account using the *screened Coulomb interactions* model [72, 73]. This correction deals with the charge transfer problem. In the KKR-CPA formalism embedding a single atom into the effective medium may violate the condition of charge neutrality. This happens because an arbitrary choice of atomic spheres may result in a net charge transfer different from the alloy average value. Therefore, the system of effective medium plus single atom will have extra charges which must be compensated in some way to keep the system neutral. According to this model, an additional shift of

$$v_R^{scr,i}(r_R) = -\frac{2\alpha_{scr}}{w}(Q_R^{i,s} - Q_R^s), \quad (4.85)$$

is added to the spherical part of the potential of the i th alloy component at site R , where $Q_R^{i,s}$ is the net charge inside the potential sphere of i th alloy component at site R and $Q_R^s = \sum_i c_R^i Q_R^{i,s}$. The α_{scr} is called the on-site screening constant and is different for different alloy components.

Applying this model for the total energy calculation using the FCD technique, the following contribution must be considered:

$$E^{scr} = -\sum_{R,i} c_R^i \frac{\alpha_{scr}}{w} \beta (Q_R^{i,s} - Q_R^s)^2. \quad (4.86)$$

Here, β is the average on-site screening constant, which accounts for the electrostatic multipole moment energy contribution due to inhomogeneous local environments of different sites in a random alloy [73]. Finally, the FCD total energy is obtained from the following expression,

$$E_{tot} = T_s[n] + \sum_{R,i} c_R^i (E_R^{intra,i}[n_R^i] + E_R^{xc,i}[n_R^i]) + E^{inter}[n] + E^{scr} \quad (4.87)$$

The CPA can be used to describe many physical properties of disordered alloys. It is nonetheless important to note that there are some effects which are not properly taken into account, and as a result CPA fails in some applications. For instance, because of the single-site approximation, it cannot account for composition fluctuations in the local environment of a site. Such fluctuations may strongly influence equilibrium or magnetic properties of the system [74]. In addition, short-range order effects can only be taken into account accurately and convincingly within the context of a multisite theory like LSGF [70, 71]. Also local atomic relaxation missing within CPA entirely, can only be taken into account by supercell calculations [75].

4.7 EMTO-CPA code

The EMTO-CPA method has been implemented within the *EMTO-CPA* code. Here in this thesis, I use the Lyngby version of this code maintained by Prof. A. V. Ruban². This code consists of four packages that one needs to run in a proper order for calculating the FCD total energy of a system. The first package hereafter referred to as **kstr** allows one to calculate slope matrix and its energy derivatives for a real energy parameter $\omega \equiv (\kappa w)^2$ on a real space cluster for a given structure. It also computes the Madelung matrix of the system. The slope matrix calculation will be discussed in the next chapter. The second package is **shape** that calculates the shape function of the structure. The third package is referred to as **kgrn** and it solves the Kohn-Sham equation using EMTO-CPA formalism in a self-consistent cycle, and the final package is **kfcd** responsible for computing the total energy of the system by FCD technique.

²Department of Materials Science and Engineering, KTH Royal Institute of Technology, SE-100 44 Stockholm, Sweden and Materials Center Leoben Forschung GmbH, A-8700 Leoben, Austria

Chapter 5

Slope Matrix

The elements of the slope matrix $S_{R'L'RL}^a$ are the expansion coefficients of the screened spherical waves centered at lattice site R around site R' . Determining these matrices is one of the most challenging parts of the calculation. As it has been shown in the previous chapter, during the self-consistent calculation we need to know the slope matrix and its first energy derivative for a set of complex energies on the energy contour enclosing the valence states. In every iteration, the Fermi energy is updated with Eq. (4.28) and thus the energy points on the complex contour change. As a result, the slope matrix and its energy derivative need to be recalculated after every iteration for the new set of energy points.

The slope matrix can be calculated using the *inhomogeneous Dyson equation* [18] on a real space cluster of finite size including a number of nearest lattice sites. Then the slope matrix in \mathbf{k} -space is computed from a Bloch sum,

$$S_{R'L'RL}^a(\kappa^2, \mathbf{k}) = \sum_T e^{i\mathbf{k}\cdot\mathbf{T}} S_{R'L'(R+T)L}^a(\kappa^2), \quad (5.1)$$

where \mathbf{T} is a translation vector. In the current implementation of EMTO-CPA, instead of calculating the slope matrix and its first energy derivative for a set of complex energy points directly from this method, a Taylor expansion is used. To this end, first the slope matrix and the first several energy derivatives (usually up to the 6th order) are calculated using the inhomogeneous Dyson equation only for one certain value of real energy parameter κ^2 . Then the \mathbf{k} -dependent forms of these matrices are obtained from a Bloch sum. Eventually, these matrices are applied to calculate the \mathbf{k} -dependent slope matrix and its first energy derivative

5.1. Inhomogeneous Dyson equation

for any complex energy points on the contour using this *Taylor expansion*. Although it is clear that this procedure speeds up the self-consistent calculation, there are some problems such as accuracy and efficiency which show the necessity for a more accurate and efficient method to replace the Taylor expansion.

In this chapter, I will first review the basics of the current formalism which is used for calculating these matrices and then show the results of the new development which allows one to calculate the slope matrix and the first energy derivative for all energy points directly from the inhomogeneous Dyson equation.

5.1 Inhomogeneous Dyson equation

The inhomogeneous Dyson equation connects the elements of the slope matrix or the screened structure constants matrix with the elements of the *bare structure constants* matrix. The bare structure constants matrix, $S_{R'L'RL}^0(\kappa^2)$, is defined within the KKR formalism [5, 60] as the expansion coefficients of the bare spherical waves $n_L(\kappa^2, \mathbf{r}_R) \equiv n_l(\kappa^2, \mathbf{r}_R)Y_L(\hat{\mathbf{r}}_R)$ centered on site R , in terms of $j_L(\kappa^2, \mathbf{r}_{R'}) \equiv j_l(\kappa^2, \mathbf{r}_{R'})Y_L(\hat{\mathbf{r}}_{R'})$ centered on site R' ,

$$n_L(\kappa^2, \mathbf{r}_R) = - \sum_{L'} j_{L'}(\kappa^2, \mathbf{r}_{R'}) S_{R'L'RL}^0(\kappa^2). \quad (5.2)$$

They can be calculated explicitly from the following equation,

$$S_{R'L'RL}^0(\kappa^2) = -8\pi \sum_{L''} (-1)^l C_{LL'L''} (-\kappa w)^{(l+l'-l'')} \frac{(2l''-1)!!}{(2l'-1)!!(2l-1)!!} n_{L''}(\kappa^2, \mathbf{R}-\mathbf{R}'). \quad (5.3)$$

The bare structure constants matrix is Hermitian and since the Gaunt numbers vanish unless $l+l'+l''$ is even, all elements of this matrix are real for a real κ^2 .

In order to derive the inhomogeneous Dyson equation, one can start from Eq. (4.9). Using this equation, a screened spherical wave in the entire space can be expressed by the multi-center expansion

$$\psi_{RL}^a(\kappa^2, \mathbf{r}) = \sum_{R'L'} [f_{Rl}^a(\kappa^2, r_R) Y_L(\hat{\mathbf{r}}_R) \delta_{RR'} \delta_{LL'} + g_{R'l'}^a(\kappa^2, r_{R'}) Y_{L'}(\hat{\mathbf{r}}_{R'}) S_{R'L'RL}^a(\kappa^2)]. \quad (5.4)$$

Using the head and tail functions in Eq. (4.10), the above equation can be

Chapter 5. Slope Matrix

rewritten as

$$\begin{aligned} \psi_{RL}^a(\kappa^2, \mathbf{r}) = & \sum_{R'L'} n_{l'}(r_{R'}) Y_{L'}(\hat{\mathbf{r}}_{R'}) [t_{Rl}^1 \delta_{RR'} \delta_{LL'} - t_{R'l'}^3 S_{R'L'RL}^a] \\ & - \sum_{R'L'} j_{l'}(r_{R'}) Y_{L'}(\hat{\mathbf{r}}_{R'}) [-t_{Rl}^2 \delta_{RR'} \delta_{LL'} + t_{R'l'}^4 S_{R'L'RL}^a], \end{aligned} \quad (5.5)$$

where the κ^2 dependency has been dropped for simplicity. We can also expand the screened spherical wave in the entire space in terms of the bare spherical waves. This leads to

$$\begin{aligned} \psi_{RL}^a(\kappa^2, \mathbf{r}) = & \sum_{R'L'} \left[n_{l'}(r_{R'}) Y_{L'}(\hat{\mathbf{r}}_{R'}) M_{R'L'RL}^a \right. \\ & \left. - \sum_{R''L''} j_{l''}(r_{R''}) Y_{L''}(\hat{\mathbf{r}}_{R''}) S_{R''L''R'L'}^0 M_{R'L'RL}^a \right], \end{aligned} \quad (5.6)$$

where $M_{R'L'RL}^a$ is a yet unknown transformation matrix. Comparing Eqs. (5.6) and (5.4), one can find

$$M_{R'L'RL}^a = r_{Rl}^1 \delta_{RR'} \delta_{LL'} - t_{R'l'}^3 S_{R'L'RL}^a, \quad (5.7)$$

and

$$\sum_{R''L''} S_{R'L'R''L''}^0 M_{R''L''RL}^a = -t_{Rl}^2 \delta_{RR'} \delta_{LL'} + t_{R'l'}^4 S_{R'L'RL}^a. \quad (5.8)$$

Substituting $M_{R''L''RL}^a$ in Eq. (5.8) with the right hand side of Eq. (5.7) results in

$$\begin{aligned} -t_{Rl}^2 \delta_{RR'} \delta_{LL'} + t_{R'l'}^4 S_{R'L'RL}^a = & \\ & \sum_{R''L''} S_{R'L'R''L''}^0 [t_{Rl}^1 \delta_{R''R'} \delta_{L''L'} - t_{R''l''}^3 S_{R''L''RL}^a]. \end{aligned} \quad (5.9)$$

Finally, rearranging for S^a , the inhomogeneous Dyson equation will be obtained,

$$S_{R'L'RL}^a = \frac{t_{Rl}^1}{t_{Rl}^3} \delta_{RR'} \delta_{LL'} + \frac{1}{t_{R'l'}^3} \left[-S^0 - \frac{t_{Rl}^4}{t_{Rl}^3} \right]_{R'L'RL}^{-1} \frac{d_{Rl}^a}{t_{Rl}^3}, \quad (5.10)$$

where d_{Rl}^a is the determinant of the screening matrix defined in Eq. (4.13) and it can be shown that

$$d_{Rl}^a = t^1 t^4 - t^2 t^3 = -2 \frac{a_R}{w}. \quad (5.11)$$

5.1.1 Blowing-up Technique

Eq. (5.10) together with Eq. (5.3) can be used to calculate the slope matrix for an arbitrary complex energy. As it is clear from Eq. (4.34), in addition

5.1. Inhomogeneous Dyson equation

to the low- l block ($l, l' \leq l_{max}$), we also need to know the off-diagonal blocks ($l \leq l_{max}, l_{max} < l' \leq l_{max}^h$ and $l' \leq l_{max}, l_{max} < l \leq l_{max}^h$) of the slope matrix. Calculating the full slope matrix up to l_{max}^h using the above equations is a relatively time-consuming task, especially keeping in mind that we need to compute the slope matrix and its first energy derivative for a reasonable number of nearest lattice sites within the real space cluster and then apply Eq. (5.1) to calculate them in k -space. The most time-consuming part of the calculation is the matrix inversion in Eq. (5.10). Although applying optimized routines for matrix-matrix operations, such as matrix-matrix multiplication or matrix inversion, implemented within the standard programming libraries can speed up the calculation and reduce computational expenses significantly, there is a much simpler method, known as the blowing-up technique [76], which makes it possible to calculate instantly the off-diagonal elements from low- l block.

Rearranging Eq. (5.9), one can find the following equation,

$$t_{R'l'}^4 S_{R'l'RL}^a = t_{Rl}^2 \delta_{RR'} \delta_{LL'} + S_{R'l'RL}^0 t_{Rl}^1 - \sum_{R''L''} S_{R'l'R''L''}^0 t_{R''l''}^3 S_{R''L''RL}^a. \quad (5.12)$$

Let us consider the above equation for $l' > l_{max}$ and $l \leq l_{max}$. As it was mentioned in Subsection 4.1.1 the tail function must reduce to the Bessel function when $l' > l_{max}$. This brings us to $t_{Rl}^3 = 0$ and $t_{Rl}^4 = 1$ for high l orbitals. Therefore, Eq. (5.11) can be rewritten as

$$S_{R'HRL}^a = S_{R'HRL}^0 t_{Rl}^1 - \sum_{R''L''}^{l_{max}} S_{R'H R''L''}^0 t_{R''l''}^3 S_{R''L''RL}^a, \quad (5.13)$$

where $H \equiv (l'm')$ with $l' > l_{max}$ and the HL block of bare structure constants matrix is obtained from Eq. (5.3). With this equation, the HL block of the slope matrix is obtained from the low- l block. The LH block is found by the following expression

$$S_{R'HRL}^a = a_R S_{RLR'H}^a, \quad (5.14)$$

which is valid because S^a is a Hermitian matrix.

5.1.2 Energy Derivatives of the Slope Matrix

In order to express the energy derivatives of the slope matrix, a dimensionless energy parameter $\omega \equiv (\kappa w)^2$ is introduced. Rearranging Eq. (5.9), we have

$$\sum_{R''L''} \mathcal{B}_{R'l'R''L''}(\omega) \mathcal{A}_{R''L''RL}(\omega) = -2 \frac{a_R}{w} \delta_{R'R} \delta_{L'L}, \quad (5.15)$$

where

$$\mathcal{A}_{R'L'RL}(\omega) = \frac{t_{RL}^1(\omega)}{t_{RL}^3(\omega)} \delta_{R'R} \delta_{L'L} - S_{R'L'RL}^a(\omega), \quad (5.16)$$

and

$$\mathcal{B}_{R'L'RL}(\omega) = t_{R'L'}^3(\omega) [t_{RL}^4(\omega) \delta_{R'R} \delta_{L'L} + S_{R'L'RL}^0 t_{RL}^3]. \quad (5.17)$$

Then, using above expressions and applying the product rule for matrices ¹, the n th order energy derivative of the slope matrix is obtained as

$$\begin{aligned} \frac{d^n S^a(\omega)}{d\omega^n} = & \mathcal{B}(\omega)^{-1} \left[\sum_{i=0}^{n-1} \frac{n!}{i!(n-i)!} \frac{d^{n-i} \mathcal{B}(\omega)}{d\omega^{n-i}} \frac{d^i \mathcal{A}(\omega)}{d\omega^i} + 2 \frac{a}{w} \delta_{n,0} \right] \\ & + \frac{d^n t^1(\omega)}{d\omega^n t^3(\omega)}, \end{aligned} \quad (5.18)$$

where RL subscripts have been dropped.

5.2 Details of Real Space-Cluster Calculations

In order to make use of the above formulae to calculate the slope matrix and its energy derivative, for each site R a finite cluster of first few nearest-neighbor lattice sites in real space is set up. The low- l block of the slope matrix and its energy derivative for every RR' pair are computed by Eq. (5.10) and Eq. (5.18). Then using Eq. (5.18) the off-diagonal elements are calculated. To make this procedure complete, it is necessary to determine appropriate values for several parameters.

The first important parameter is the hard sphere radius. This parameter can affect to some extent the degree of localization of screened spherical waves. The boundary conditions in Eqs. (4.11) and (4.12) make the head and tail functions energy independent on the hard sphere. Therefore the slope matrix is expected to show a smooth behavior and weak energy dependence. Moreover, since the tail function vanishes on hard spheres, the slope matrix and its derivative should decrease rapidly with the distance $|\mathbf{R}' - \mathbf{R}|$. Detailed calculations for a *bcc* structure for $\omega = 0$ show that the slope matrix and its energy derivatives have short range when the hard sphere radius is within an interval of $0.50w < a_R < 0.75w$ [20]. It was also found that this condition holds for other lattice types and usually the best behavior is obtained for $a_R \approx 0.7w$ [18].

¹The n th order derivative of a matrix product, like AB , is obtained by $(AB)^{(n)} = \sum_{i=0}^n \frac{n!}{i!(n-i)!} A^{(n-i)} B^{(i)}$, where the superscripts in parenthesis is the derivative order.

Another important parameter is the size of the cluster. An optimized value for this parameter can be obtained by observing the convergence of diagonal elements of the slope matrix, particularly the ss element which has the longest range, in terms of coordination shell numbers [18, 20]. For instance, the calculations for a bcc structure for $\omega = 0$ show that for 9 coordination shells or equivalently 137 nearest neighbor atoms in the cluster, the absolute value of ss element of the slope matrix and its first energy derivative almost drops from 2 to 10^{-5} and from 0.15 to 10^{-6} , respectively [20]. In most cases, considering around 100 atoms in the cluster will be enough to reproduce the slope matrix and its energy derivatives with an acceptable accuracy.

The last parameter is the number of Watson orbitals. For positive energies the screened spherical waves for a finite cluster exhibit surface resonances. To overcome this problem, a concave hard sphere, so-called Watson sphere, enclosing the cluster of hard spheres is considered. The radius of this sphere is chosen to be larger than the radius of the real space cluster plus the largest a_R . Elements of the matrix which must be inverted in Eqs. (5.10) and (5.18), will be calculated for this sphere and attached to the real matrix increasing the matrix dimension. After inversion, these elements are dropped. This technique is expected to remove the surface resonances or to push them towards the higher energies. The maximum orbital quantum number on the Watson sphere is l_{max}^w . Usually, $l_{max}^w = 6 - 8$ is sufficient for positive energies $\omega \leq 5$ [20].

5.3 Taylor Expansion

For a self-consistent calculation, the slope matrix and its energy derivative need to be calculated within an energy window from the bottom of the valence band ϵ_b up to ~ 0.2 Ry above the Fermi level, *i.e.* $\epsilon_b \leq \text{Re}(z) \lesssim \epsilon_F + 0.2$ Ry, where $z \equiv \kappa^2 + v_0$. Energies above the Fermi level are used during the search for the Fermi level for the next iteration.

The presently implemented method for calculating the slope matrix and its first energy derivative for a set of complex energy points is to use a Taylor expansion around a reference energy parameter ω_0 as follows

$$S^a(\omega, \mathbf{k}) = S^a(\omega_0, \mathbf{k}) + \sum_{n=1}^{n_{max}} \frac{1}{n!} \left. \frac{d^n S^a(\omega, \mathbf{k})}{d\omega^n} \right|_{\omega=\omega_0} (\omega - \omega_0)^n, \quad (5.19)$$

and

$$\dot{S}^a(\omega, \mathbf{k}) = \dot{S}^a(\omega_0, \mathbf{k}) + \sum_{n=2}^{n_{max}} \frac{1}{(n-1)!} \left. \frac{d^n S^a(\omega, \mathbf{k})}{d\omega^n} \right|_{\omega=\omega_0} (\omega - \omega_0)^{(n-1)}, \quad (5.20)$$

where, n_{max} is the Taylor expansion order. Here, we have dropped the RL subscripts for simplicity. The slope matrix for a real number ω_0 is calculated from Eqs. (5.10), (5.13) and (5.14), and then the energy derivatives are computed using Eq. (5.18). All these calculations are performed in real space. Then, during the self-consistent cycle, the Bloch transform of these matrices for every \mathbf{k} -point are calculated. Finally, they are used to calculate $S^a(\omega, \mathbf{k})$ and $\dot{S}^a(\omega, \mathbf{k})$ for any complex ω on the energy contour using equations (5.19) and (5.20).

Although this procedure speeds up the self-consistent cycle, it imposes accuracy and system-size limitations. The first problem of this method is the considerable computer memory needed to store the slope matrix and all energy derivatives of every lattice site for reference energy parameter ω_0 . Usually, a 6th-order Taylor expansion is taken into account to produce acceptable results. The dimension of the slope matrix or each energy derivative needed to be stored for each lattice site is $\{(2l_{max}^h + 1)^2\} \times \{(2l_{max} + 1)^2 \times N\}$ where N is the size of real space cluster. The more sites in the unit cell exist, the more memory is needed. Therefore, for large systems with many atoms in the unit cell, this method imposes a too strong memory demand.

For systems with deep-lying core states and narrow valence bands, the Taylor expansion gives usually acceptable results, since the interval needed for finding eigenstates and Fermi energy is not that wide. In such cases the required interval of ω for calculating the slope matrix and its first energy derivative is around $-8 \leq \text{Re}(\omega) \leq +8$. Accuracy tests for an *fcc* structure show that a 6th-order Taylor expansion with $\omega_0 = 0$ yields $S^a(\omega, \mathbf{k})$ and $\dot{S}^a(\omega, \mathbf{k})$ for $|\omega| \leq 5$ with an accuracy around $\sim 1\%$ and $\sim 5\%$, respectively [77]. With increasing $|\omega|$ the relative error increases, particularly for $S^a(\omega, \mathbf{k})$, for which it increases to $\sim 30\%$ for $|\omega| = 10$.

The systems in which a wide energy window is required during the self-consistent cycle can be divided into two groups. First, if $\epsilon_F - v_0 \sim 0.8$ Ry or larger, the Taylor expansion diverges for energies near and above ϵ_F . Second, when $\epsilon_b \ll v_0$, the Taylor expansion breaks down for energies near the bottom of the valence band. Both of these cases become more problematic for solids with a large Wigner-Seitz radius. In order to improve the convergence of the expansion for a large energy window, a two-center Taylor expansion formalism was suggested [77]. It was shown that it can improve the accuracy of the expansion for energies near ϵ_b , but it cannot modify the expansion results for energies around ϵ_F . In addition, such a procedure increases the memory demand even further. Therefore, from the point of view of the accuracy, the main problem is around ϵ_F .

5.4 Direct Calculation of the Slope Matrix

The most robust way of calculating the slope matrix and its first energy derivative is a direct method in which $S^a(\omega)$ and $\dot{S}^a(\omega)$ matrices are computed for all selected complex energy points on the contour at every iteration of the self-consistent cycle directly from the real space cluster method described earlier in this chapter. Although this might seem to involve heavy and time-consuming calculations, it could be practical for systems in which the Taylor expansion is neither possible due to memory demands nor accurate when applied for systems with a large characteristic bandwidth.

Another important reason which motivates developing a more accurate and efficient method for the slope matrix calculation is the idea of introducing the *FCD* technique into the self-consistent cycle of SCA-EMTO calculation, which has been a main objective for new modifications of EMTO based codes. The point is that even with the SCA for the potential a self-consistent FCD approach may result in the accuracy of the total energy comparable to full-potential methods. However, the FCD method in itself is quite computationally expensive, which puts an additional constraint on the size of the crystal structure for which the derivatives of the slope matrix can be stored when the Taylor expansion is used.

The direct slope-matrix calculation has been developed within the EMTO-CPA code. To this end, the package `kstr` designed for complex ω has been rewritten using updated libraries from the linear algebra package (LAPACK). In particular, routines for matrix factorization, inversion and matrix-matrix multiplication have been used. Then, routines for the slope-matrix calculation have been incorporated into `kgrn` package as an option along with the Taylor expansion, allowing the user to choose either a direct calculation of $S^a(\omega, \mathbf{k})$ or $\dot{S}^a(\omega, \mathbf{k})$ or a Taylor expansion. Finally, the new part of the code was parallelized using the *Message Passing Interface* (MPI) library in a manner consistent with the original parallelization of the code.

When the slope matrix is calculated on the real energy axis, the Bessel and Neumann functions are used as basis functions for positive ω and Bessel and Hankel functions for negative ω . In this case the slope matrix will be real on the real energy axis. For a general complex ω , it is more consistent to use Bessel and Neumann functions everywhere. In this case, the slope matrix is complex for all complex values of ω and is real for all real values of ω . This has been illustrated in Figure 5.1, which shows the real and imaginary part of *ss* component of the slope matrix, $S_{ss}^a \equiv S_{00}^a(\omega, \mathbf{k} = (0, 0, 0))$, in terms of ω for a *bcc* lattice. The reason for showing only the *ss* components is that it is the largest and the most delocalized one in real space. The zeros in index of S_{00}^a denotes S_{LL}^a with $L = l(l + 1) + m$.

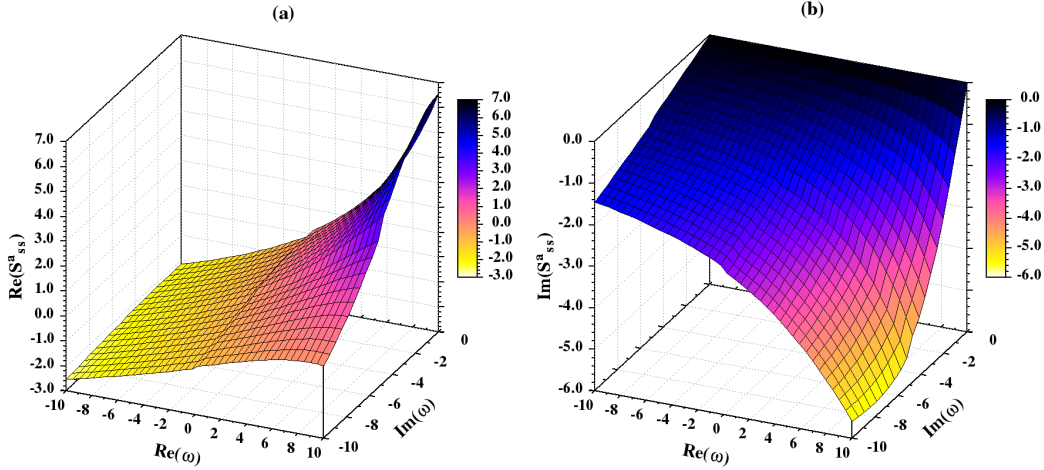


Figure 5.1: (a) Real and (b) imaginary parts of ss element of $S^a(\omega, \mathbf{k})$ of a bcc lattice for $\mathbf{k} = (0, 0, 0)$ as a function of complex ω . The mesh step for ω in complex plane is 0.5 on both real and imaginary axes.

For this calculation, 9 coordination shells or equivalently 137 nearest neighbors in the real-space cluster have been considered. Other parameters are $l_{max} = 3$, hard sphere radius $a_R = 0.7w$ and the maximum of orbital quantum number on the Watson sphere $l_{max}^w = 8$. As can be seen from the graph, the imaginary part of $Im(S_{ss}^a)$ is zero only when ω is real. Here we concentrate on the negative imaginary part of ω , since $Re[S^a(\omega)] = Re[S^a(\omega^*)]$ and $Im[S^a(\omega)] = -Im[S^a(\omega^*)]$.

Figure 5.2 shows the absolute difference between the direct calculation and a 6th-order Taylor expansion of S_{ss}^a and \dot{S}_{ss}^a , namely as $|\Delta S_{ss}^a|$ and $|\Delta \dot{S}_{ss}^a|$, respectively. According to expectation, these graphs show that the values of both $|\Delta S_{ss}^a|$ and $|\Delta \dot{S}_{ss}^a|$ increase as the distance from the expansion center $\omega_0 = 0$ increases. It is also clear that the accuracy of the Taylor expansion when $Re(\omega) > 0$ is worse than when $Re(\omega) < 0$. It also can be seen that in the regions where the real part of $|\Delta S_{ss}^a|$ or $|\Delta \dot{S}_{ss}^a|$ increases, the imaginary part decreases and vice versa. Thus, the accuracy of the Taylor expansion for real and imaginary parts show opposite trends.

A better way to express the accuracy of the Taylor expansion might be computing relative error defined as [77]:

$$\delta S^a = \frac{\{[\text{Re}(S_{\text{Direct}}^a - S_{\text{Taylor}}^a)]^2 + [\text{Im}(S_{\text{Direct}}^a - S_{\text{Taylor}}^a)]^2\}^{1/2}}{\{[\text{Re}(S_{\text{Direct}}^a)]^2 + [\text{Im}(S_{\text{Direct}}^a)]^2\}^{1/2}} \times 100. \quad (5.21)$$

Figure 5.3 shows the computed relative error of S_{ss}^a and \dot{S}_{ss}^a for bcc lattice. For

5.4. Direct Calculation of the Slope Matrix

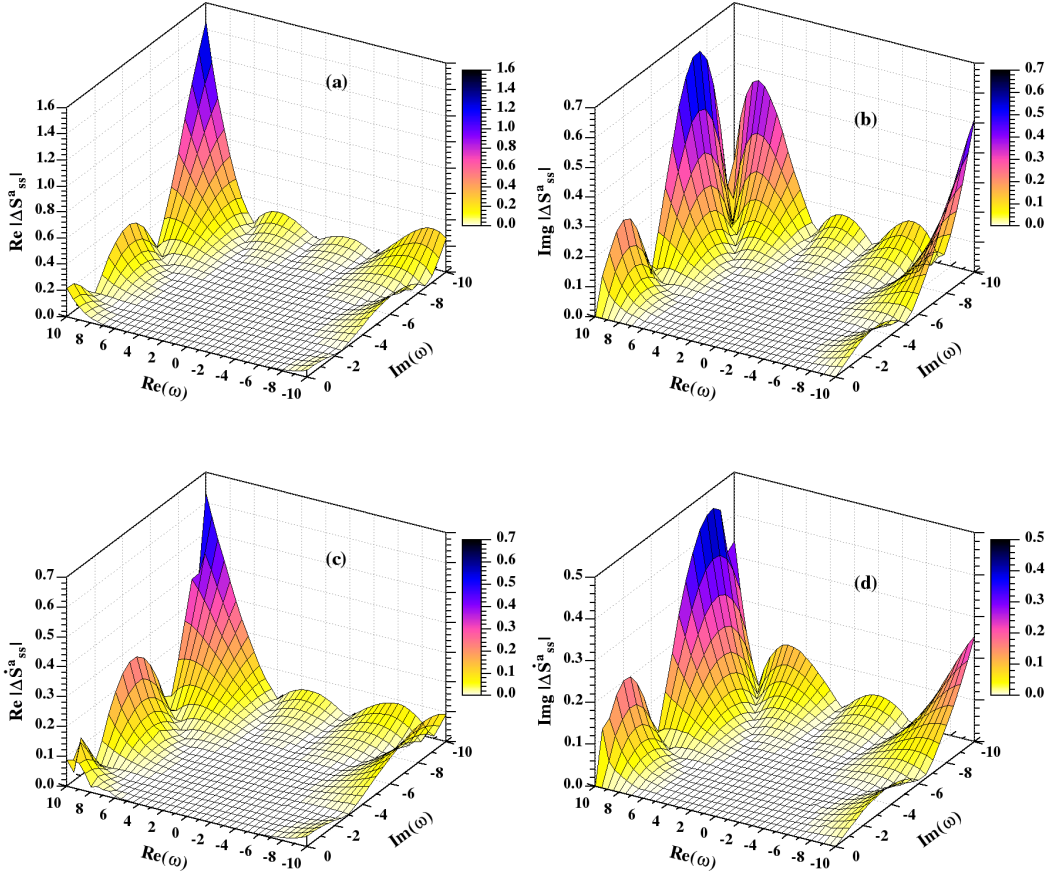


Figure 5.2: The difference between the direct calculation and a 6th-order Taylor expansion of $S_{ss}^a(\omega, \mathbf{k})$, panel (a) and (b), and $\hat{S}_{ss}^a(\omega, \mathbf{k})$, panel (c) and (d), for a *bcc* lattice as a function of complex ω . The z axes in these graphs are real and imaginary of $|\Delta S_{ss}^a| = |S_{ss}^{a,Direct} - S_{ss}^{a,Taylor}|$ and $|\Delta \hat{S}_{ss}^a| = |\hat{S}_{ss}^{a,Direct} - \hat{S}_{ss}^{a,Taylor}|$. The expansion center is $\omega_0 = 0$.

more clarity, in this figure a logarithmic scale for z -axis has been used. These graphs show that the values of δS_{ss}^a and $\delta \hat{S}_{ss}^a$ within the region $|\omega| \leq 6$ are less than 0.5% and 1%, respectively. The most important regions in these graphs are the ones close to the real axis on both negative and positive sides with $|\omega| \geq 6$, since they correspond to the previously mentioned cases of Taylor expansion failures. These graphs show a similar trend as the ones calculated for the *fcc* lattice in Ref [77]. In that paper, it was shown that a two-center Taylor expansion can improve the accuracy of determining S^a and \hat{S}^a for the negative side of the real axis, but it does not affect the accuracy for points on the positive side of the real axis. The contour used during the self-consistent cycle is usually a semi-circle or a semi-ellipse in the complex plane with the diameter along the real axis from ϵ_b

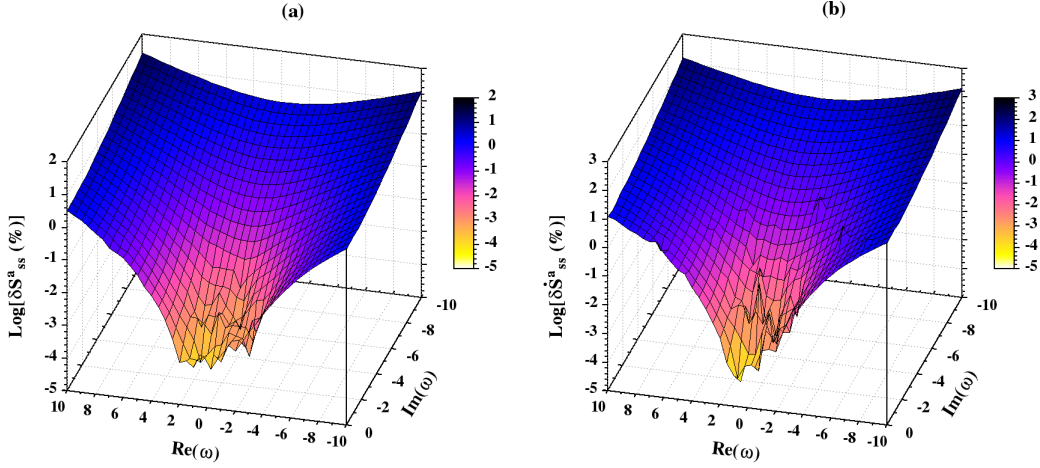


Figure 5.3: Relative error of S_{ss}^a and \dot{S}_{ss}^a as a function of ω in a logarithmic scale for bcc lattice corresponding to the graphs in Figure 5.2. The point $\omega = 0$ with $\delta S_{ss}^a = 0\%$ have been excluded for clarity.

to $\epsilon_F + \sim 0.2$. The points chosen on this contour are dense around the Fermi level since they are used, together with an additional horizontal contour containing a few points very close to the real axis, to determine the Fermi level. The graphs in Figure 5.3 show that close to the real axis the relative error of S_{ss}^a and \dot{S}_{ss}^a within the interval $6 < \text{Re}(\omega) < 10$ increases from $\sim 0.5\%$ up to $\sim 4\%$, and from $\sim 1\%$ up to $\sim 13\%$, respectively. Therefore, for systems in which this interval is used for searching the Fermi level, considerable errors in the Taylor expansion of S^a and \dot{S}^a can be expected, which affects all energies within this interval including the Fermi level and all properties derived from it.

5.4.1 Application of Directly Calculating S^a and \dot{S}^a

To see how the direct calculation performs versus the Taylor expansion in actual application, tungsten exhibiting a bcc lattice was chosen as a test system. The electronic configuration of tungsten is $[Xe]4f^{14}5d^46s^2$. Here, $5d^46s^2$ orbitals have been considered as valence states. Considering the experimental lattice constant $a = 3.165 \text{ \AA}$ [78], earlier Taylor expansion calculations for bcc -W have shown that $\epsilon_F - v_0 \simeq 0.8$ and $\epsilon_b - v_0 \simeq -0.1$. Therefore, the proper energy window for such a system is equivalent to the corresponding interval $-1 \lesssim \text{Re}(\omega) \lesssim 9$ required for calculating S^a and \dot{S}^a . But we have already seen that there are considerable errors in calculating S^a and \dot{S}^a for complex ω close to real axis and $\text{Re}[\omega] \leq 6$. Therefore, bcc -W is an ideal test case for studying the effect of accurate calculation of S^a and \dot{S}^a around its Fermi level.

5.4. Direct Calculation of the Slope Matrix

Table 5.1: Lattice parameter a_0 (Å), bulk modulus B , shear moduli C' and C_{44} (all moduli in (GPa)) of bcc -W using different exchange-correlation functional and a 6th-order Taylor expansion compared with other computational results and experimental data.

	EMTO			VASP[79]	ESPRESSO[79]	Exp[78]
	LDA	PBE	PBE-sol	PBE	PBE	
a_0	3.142	3.196	3.167	3.189	3.187	3.165
B	324	301	318	303	300	316
C'	197	191	190	159	160	165
C_{44}	195	196	191	146	149	164

Table 5.1 shows the computed equilibrium lattice parameter, Bulk modulus and elastic constants of bcc -W using the Taylor expansion method compared to the results of other computational methods and experimental data. For this calculation, a 6th-order Taylor expansion has been applied with the expansion center $\omega_0 = 0$. The slope matrix calculation in real space cluster for $\omega_0 = 0$ has been done considering 137 nearest neighbor vectors in cluster and $l_{max}^w = 8$. The lattice parameter and bulk modulus have been obtained using a Birch-Murnaghan equation of state fitting. For calculating the elastic constant C_{44} and shear moduli C' volume-conserving strains applied [80]. These type of strains have the advantage that the energy is an even function in terms of strain, and therefore we need to perform calculations only for distorted structures of positive (or negative) strains. For this calculation 11 distorted structures with positive strains from 0 to 0.05 have been considered. From the data in this table, one

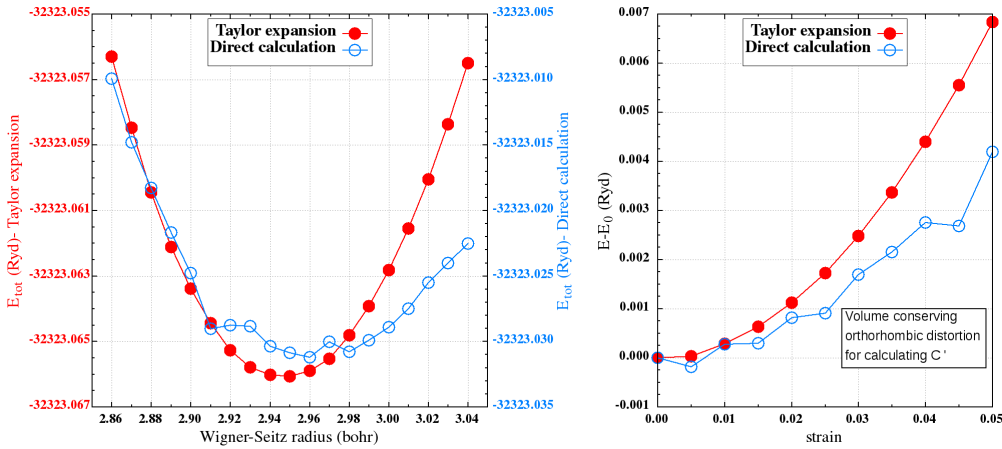


Figure 5.4: Graphs of the volume optimization and shear moduli calculations data of W - bcc using both Taylor expansion and direct calculation methods.

can see the lattice parameter and bulk modulus calculated by EMTO in a good agreement with the results of other codes, while for elastic constants a noticeable difference can be seen.

The first test calculation on *bcc*-W using the new implementation, showed the calculation converges with a reasonable trend and finishes with a few milli-Rydberg difference in total energy and Fermi energy compared to the Taylor expansion method. However, applying it for calculating equilibrium properties or elastic constants leads to unphysical discontinuities in total energy curves leading to an unpredictable total energy trend. For instance, in Figure 5.4, such energy trends are shown for volume optimization and shear moduli calculations in comparison to the regular smooth graphs obtained by Taylor expansion method. The calculated data related to the C_{44} calculation which has not been shown

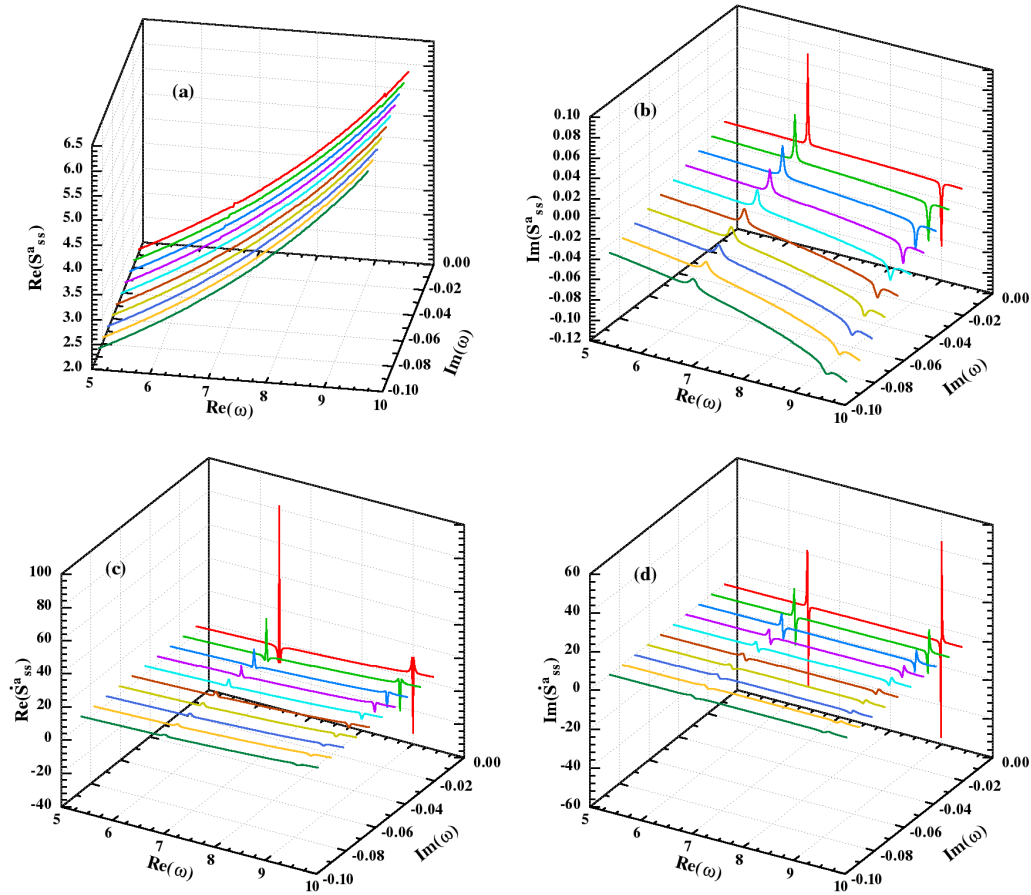


Figure 5.5: Real (panel (a), (c)) and imaginary (panel (b), (d)) parts of elements S_{ss}^a and \dot{S}_{ss}^a , respectively, calculated directly for W-*bcc* as a function of complex ω for horizontal meshes parallel to the real axis in the complex plane.

5.4. Direct Calculation of the Slope Matrix

here, shows an even worse trend than that for C' .

In order to find the reason for such an unsatisfying result, we study the behavior of the slope matrix and its energy derivative using the direct calculation method in more detail. Therefore, the slope matrix and its energy derivative of bcc -W have been computed using the direct method for a series of dense horizontal meshes parallel to the real axis. Inspecting the ss elements of $S^a(\omega, \mathbf{k} = (0, 0, 0))$ and $\dot{S}^a(\omega, \mathbf{k} = (0, 0, 0))$ revealed the presence of the sharp peaks for $-0.1 \lesssim \text{Im}(\omega) \leq 0$ and $\text{Re}(\omega) \geq 5$. These are caused by the surface resonance effect mentioned earlier which appear due to the finite size of real space cluster and are visible in Figure (5.5). As one can see from these graphs, the peak height are decreased with increasing distance from the real axis and almost disappear for $\text{Im}(\omega) \lesssim -0.1$. Further analysis on ss elements shows that it behaves smoothly as the distance from real axis increases.

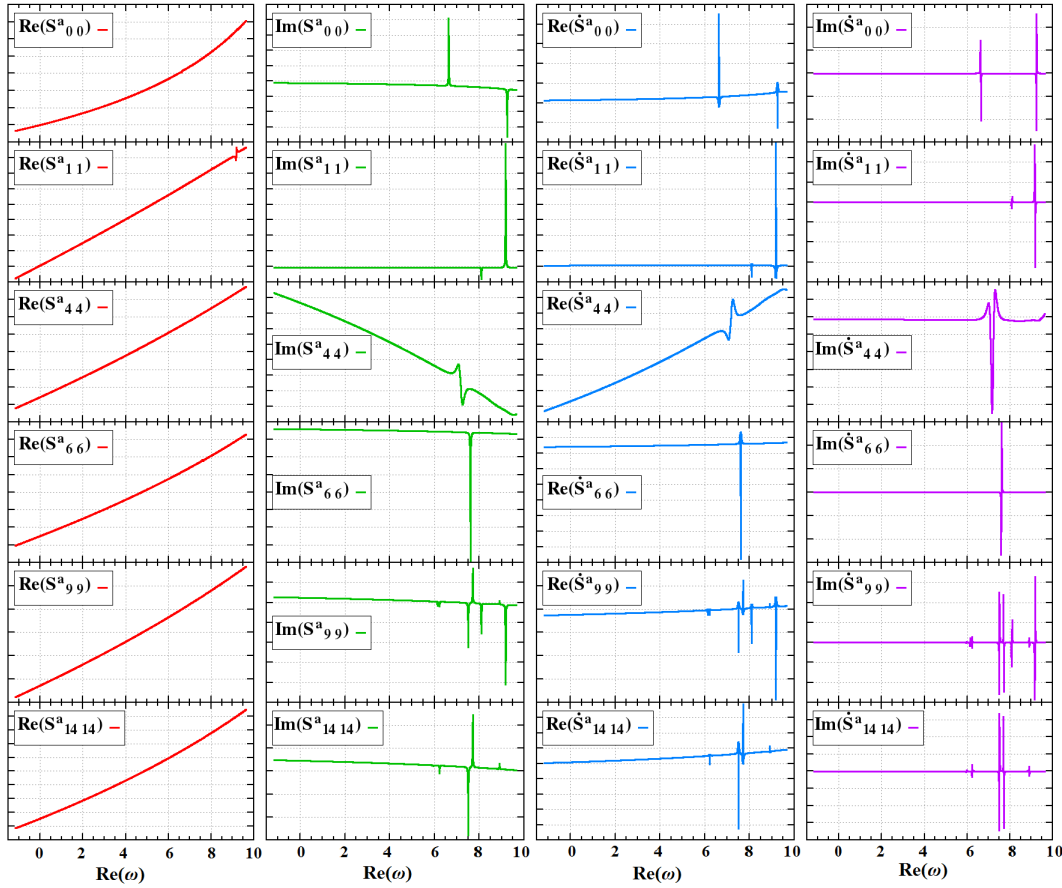


Figure 5.6: Real and imaginary parts of some different diagonal elements of $S^a(\omega, \mathbf{k})$ and $\dot{S}^a(\omega, \mathbf{k})$ matrices for bcc -W at $\mathbf{k} = 0, 0, 0$ as a function of $\text{Re}(\omega)$ on a horizontal mesh with fixed $\text{Im}(\omega) \cong -0.01$. The y axes scales are different and not shown here for simplicity.

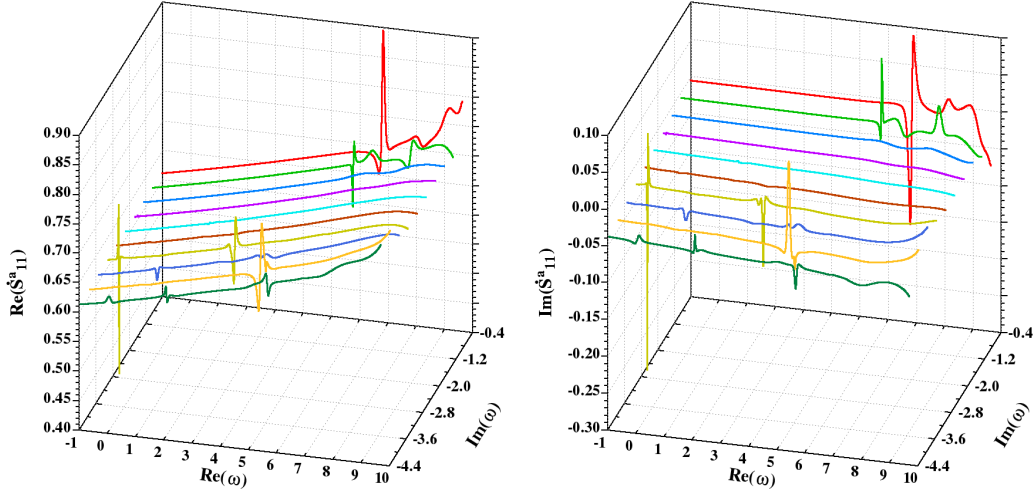


Figure 5.7: Real (left panel) and imaginary (right panel) parts of 2nd diagonal elements (pp elements) of \dot{S}^a_{ss} for bcc - W in terms of horizontal meshes of ω parallel to the real axis in complex plane.

Investigating some other selected diagonal elements of matrices which have sizable values, also confirms the presence of similar peaks. For the elements with higher L the number of these peaks is usually more than ss element. For instance, Figure 5.6 presents the real and imaginary parts of some other diagonal elements of S^a and \dot{S}^a for a dense horizontal mesh very close to the real axis. Although the peaks of the real part of S^a_{LL} are not very distinct due to the large range of variation, one can identify them from the peaks of \dot{S}^a , because any abrupt change in $\text{Re}(S^a)$ will result in a peak for $\text{Re}(\dot{S}^a)$. Furthermore, by going far from the real axis, first the peaks start to fade away, but then new peaks start to appear for different values of ω . For instance, Figure 5.7 shows the second diagonal element of \dot{S}^a for a set of horizontal meshes with $-1 \leq \text{Re}(\omega) \leq 10$ and $-4.4 \lesssim \text{Im}(\omega) \lesssim -0.4$. As is shown, close to the real axis for $\text{Im}(\omega) \approx -0.4$ and -0.8 , the graphs still fluctuate for $\text{Re}(\omega) > 5$. Then the peaks disappear, but appear again for $\text{Im}(\omega) \leq -3.2$ even when $\text{Re}(\omega) < 5$. Such a behavior was also observed for other diagonal elements with $l = 2$ or 3 .

In order to determine how the details of the current implementation for calculating S^a and \dot{S}^a can help to avoid these fluctuations, the effect of the input parameters, such as cluster size, hard sphere radii and the number of Watson orbitals, on the direct calculation of S^a and \dot{S}^a were studied. First, our investigations show that increasing the cluster size will decrease the height of the peaks, but produce smaller peaks on different locations in the complex plane. Nevertheless, this is not always valid, since for some elements an increasing cluster size

5.4. Direct Calculation of the Slope Matrix

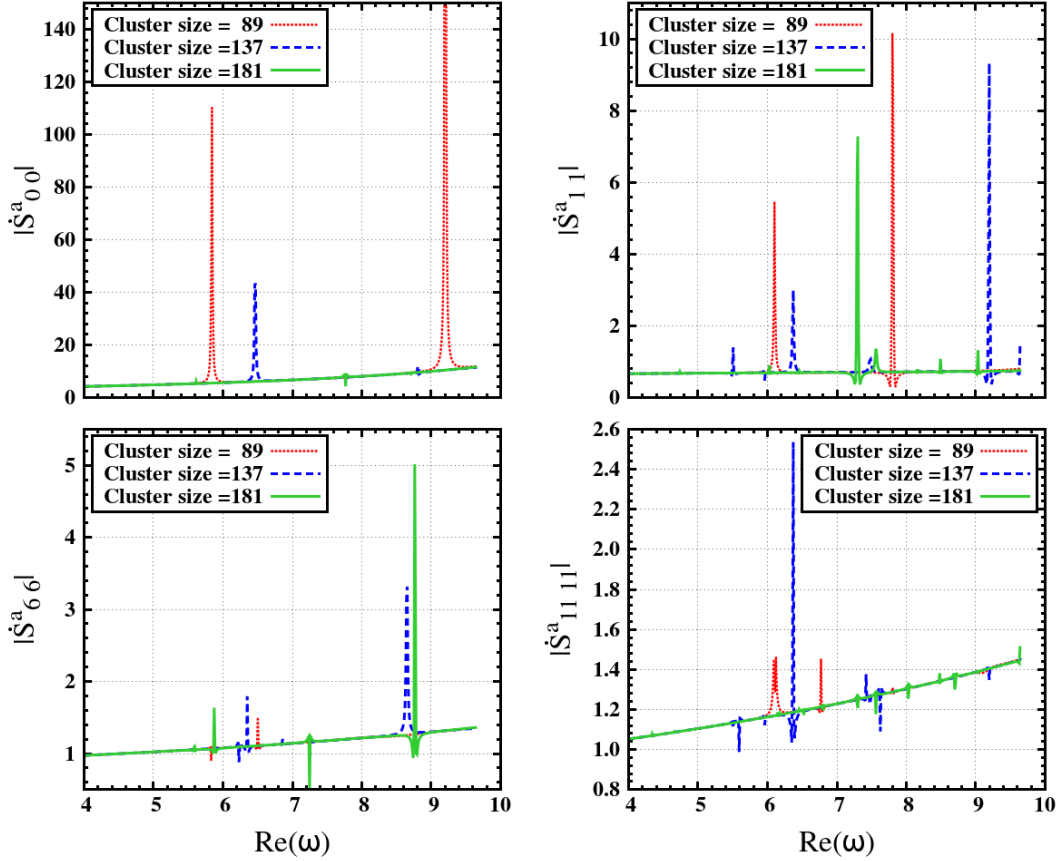


Figure 5.8: The effect of cluster size on some selected diagonal elements of $\dot{S}^a(\omega, \mathbf{k} = (0, 0, 0))$ in *bcc*-W for a horizontal mesh with $\text{Im}(\omega) \approx -0.01$.

will boost the resonances. For instance, Figure 5.8 shows the magnitude of some diagonal elements of $\dot{S}^a(\omega, \mathbf{k} = (0, 0, 0))$ as a function of $\text{Re}(\omega)$ using a horizontal mesh very close to the real axis for different values of cluster size. As one can see, the peaks for $\dot{S}^a_{0,0}$ element have reduced considerably by increasing the cluster size, while for $\dot{S}^a_{1,1}$ the reduction is not significant. For $\dot{S}^a_{6,6}$ an increasing cluster size makes the peaks larger, while for $\dot{S}^a_{11,11}$ first the peaks get larger when cluster size is 137, but then they reduce considerably for a cluster size equal to 181. Performing the same investigation for meshes chosen to be far from the real axis shows that with increasing cluster size, the overall trend of fluctuations is decreasing. This confirms once more that the surface resonance effect is a problem originating from the finite size cluster.

Repeating calculations of the volume optimization and elastic constants of *W-bcc* with increasing cluster size shows that besides having a higher computational effort, there is usually a poor convergence trend for the self-consistency

cycle. Apart from this issue, the results do not show considerable improvement of energy trends. The investigation on distorted structures also shows that their slope matrix usually behaves more fluctuating compared to the undistorted lattice. Since distorting the *bcc* lattice will reduce its symmetry, one may suspect that the fluctuations will increase for lower symmetry crystals.

Investigating the effect of the Watson sphere orbital number l_{max}^w , shows that this technique can remove the fluctuations successfully for points close to the real axis however only for $\text{Re}(\omega) \leq 5$, which is obviously not sufficient. This can be seen in upper graphs of Figure 5.9, which show two selected diagonal elements of calculated $\dot{S}^a(\omega, \mathbf{k} = (0, 0, 0))$ for *bcc*-W using the Watson sphere technique with $l_{max}^w = 8$ and without it, $l_{max}^w = 0$ as a function of $\text{Re}(\omega)$. One can clearly see that for $l_{max}^w = 8$ the fluctuations vanish for $\text{Re}(\omega) \leq 5$. One can also see this effect from Figures 5.5, 5.6 and 5.8 in which $l_{max}^w = 8$. This is in agreement with results of calculating slope matrix for real ω in Ref. [20]. Further calculations with larger

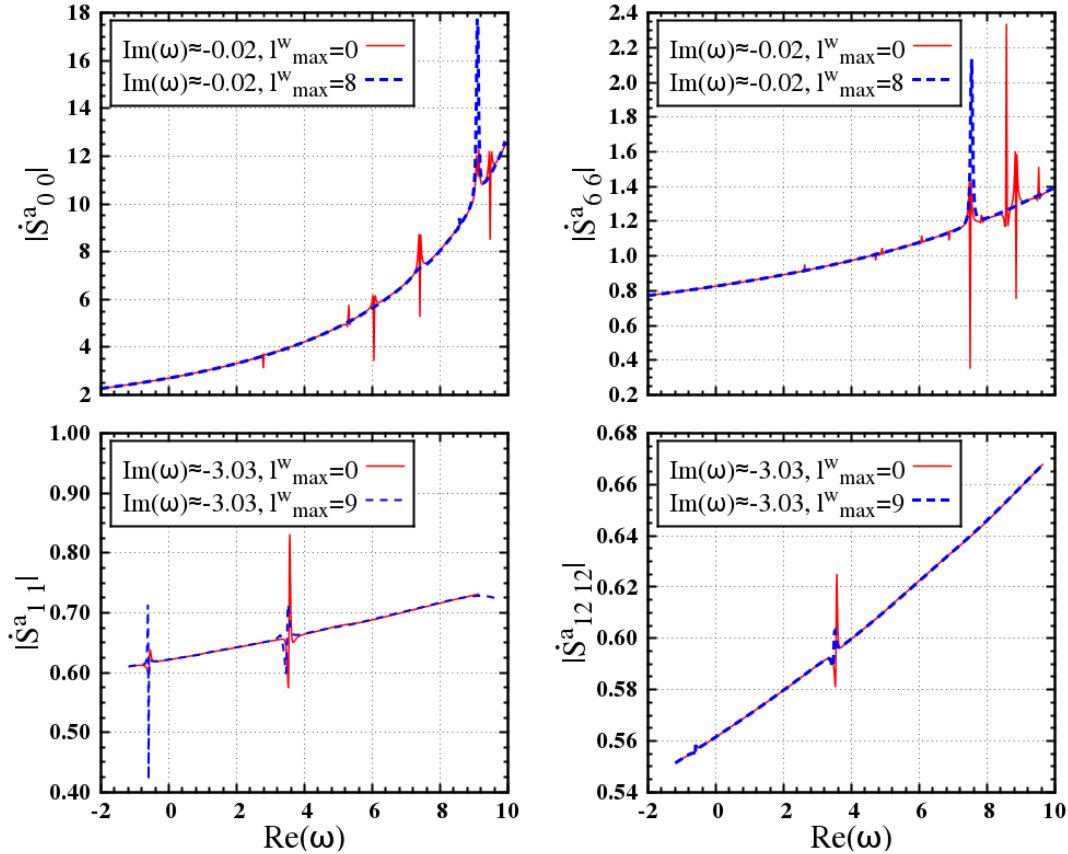


Figure 5.9: The effect of the number of Watson sphere orbitals on some selected diagonal elements of $\dot{S}^a(\omega, \mathbf{k} = (0, 0, 0))$ in *bcc*-W for a horizontal mesh with $\text{Im}(\omega) \approx -0.01$.

5.4. Direct Calculation of the Slope Matrix

l_{max}^w show no considerable effect on the peaks within the region $\text{Re}(\omega) \geq 5$. For points far from the real axis, the Watson sphere technique does not have the desired effect, since the fluctuations start to reappear again for $\text{Re}(\omega) \leq 5$. This has been shown in lower graphs of Figure 5.9 and also can be seen from the Figure 5.7.

In all of the above calculations, the hard sphere radii have been chosen to be $a = 0.7w$. The calculations show that for smaller values of the hard sphere radii the screening becomes worse and the slope matrix will get less localized, while for larger values usually it becomes more localized. This has been illustrated in Figure 5.10. As one can see from the upper panels in this figure, for a horizontal mesh close to the real axis, the real and imaginary parts of S_{00}^a for $a = 0.6w$ diverge as $\text{Re}(\omega)$ increases, while for $a = 0.8w$ they are more localized than $a = 0.7w$. Nevertheless, as is clear from the lower panels, increasing the hard sphere radii will boost the fluctuations. Analysis of some other diagonal elements of the matrices shows that changing the hard sphere radii cannot make the peaks

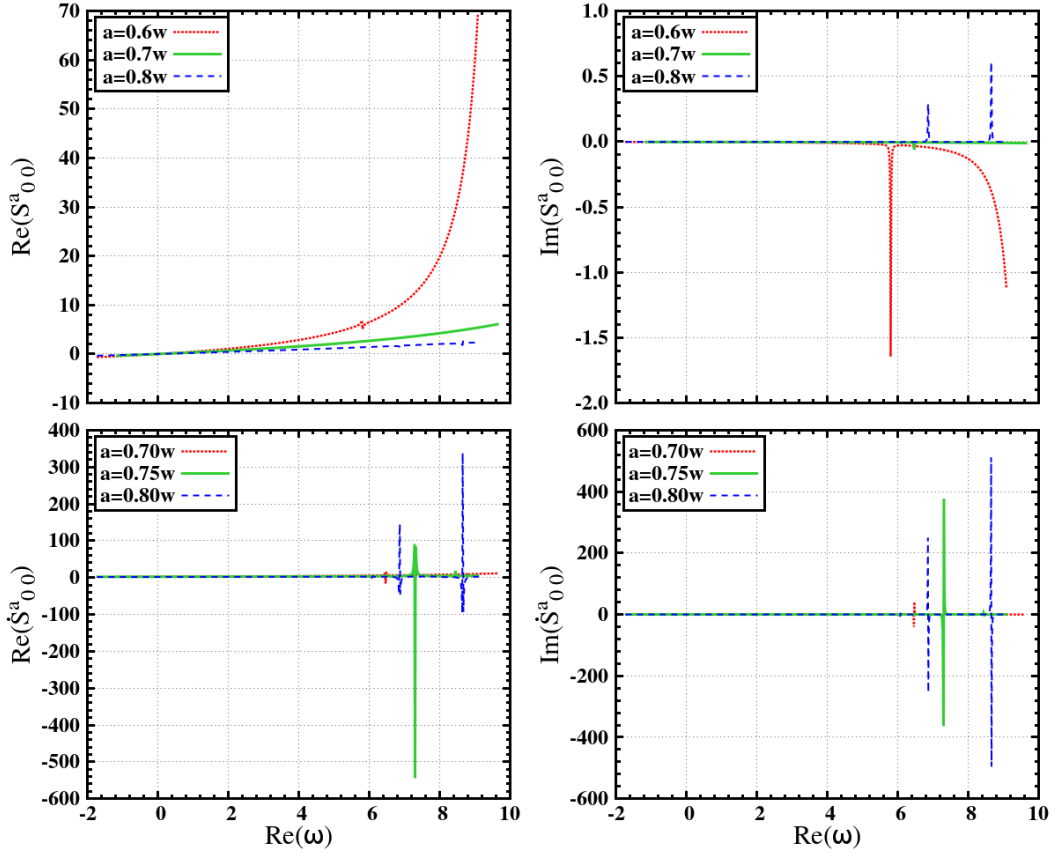


Figure 5.10: The effect of hard sphere radii on ss elements of $\dot{S}^a(\omega, \mathbf{k} = (0, 0, 0))$ in bcc -W for a horizontal mesh with $\text{Im}(\omega) \approx -0.01$.

vanish.

5.5 Conclusion

To conclude this chapter, we have explained that the current formalism for calculating the slope matrix and its first energy derivative during the self-consistent cycle of EMTO-SCA calculations using a Taylor expansion is not sufficiently accurate and efficient. As a promising replacement, we have implemented a scheme in which these matrices are calculated directly from Dyson equation for all energy points on the contour during the self-consistent cycle. However, applying this approach for calculating equilibrium properties or elastic constants of bcc-W leads to unphysical discontinuities in total energy curves leading to an unpredictable total energy trends. Further investigations revealed that the structure constants calculated using this approach show unphysical irregularities which can be seen as the sharp peaks in the graphs of the structure constants as a function of energy.

In order to determine how the new implementation can help to avoid such fluctuations, the effect of the input parameters such as cluster size, hard sphere radii and the number of Watson orbitals on the behavior of the peaks for some selected elements of the slope matrix and its first energy derivative were studied. These test calculations confirm that this effect is related to the finite size of the real-space clusters. They also show that the new implementation cannot make the fluctuations disappear from the interval energy of interest and consequently, it does not ensure to provide reliable results. Thus, it is not suitable for using within the self-consistent cycle.

Although, the most promising idea of modifications for this code has been the introduction of the FCD technique into self-consistent cycle, one must in advance devise an accurate and efficient method for calculating energy dependent slope matrix. Such a method, in the first place, must be able to overcome the deficiencies of the Taylor expansion method such as inaccuracy and inefficiency. In the second place, it must ensure that the calculated slope matrix within the interval energy of interest has no surface resonance effects and behaves smoothly. One promising solution is to calculate the slope matrix and its first energy derivative directly in the reciprocal space using techniques such as Ewald's method [81]. This approach has been implemented within some KKR-based methods [82, 83] whose potential treatment is either by the non-overlapping muffin-tin or atomic sphere approximation. Since the problem of surface resonance is related to the finite size of the real-space clusters, one can expect to calculate smooth structure constants with no fluctuations using this approach. To this end, a considerable part of `kgrrn` must be rewritten. This method imposes heavier calculations,

5.5. Conclusion

because S^a and \dot{S}^a need to be calculated for every \mathbf{k} -point as well as each complex energy. However, this approach is not applicable for LSGF method, because within this method the real space slope matrix is needed. In this case, a thorough investigation of slope matrix in real-space cluster is suggested with the aim of finding the origin of the fluctuations or understanding their behavior completely. Such a knowledge can be applied to choose a suitable approach for calculating the slope matrix in the real space.

Chapter 6

Calculating Elastic Constants of $\text{NiTi}_{(1-x)}\text{Hf}_x$ Alloys

It is known that current versions of the Green's function EMTO based methods such as the EMTO-CPA or EMTO-LSGF codes do not yield accurate results for elastic constants of many solids. In fact, comparing EMTO-CPA results with more accurate full-potential methods, one can see a notable difference in many cases [20, 84, 85]. On the other hand, for random alloys, as it has been discussed in Chapters 3 and 4, EMTO-based methods are well-suited and are advantageous over Hamiltonian-based computational schemes.

To date, the EMTO-CPA method has mainly been applied to high symmetry structures, while little is known how well it performs for low symmetry structures. The goal of this chapter is first to show the problems occurring for such systems and second to introduce the new developments within the EMTO-CPA code. One part of these new developments should facilitate elastic property calculations for low symmetry structures, the other parts should increase the efficiency of the calculation as well as the accuracy of the results. The new developments have been applied to calculate elastic properties of the shape memory alloys $\text{NiTi}_{(1-x)}\text{Hf}_x$ with $x = \{0, 0.1, 0.2, 0.3, 0.4, 0.5\}$ in the cubic $B2$ and the monoclinic $B19'$ structures.

This chapter is organized as follows. First I will briefly review the principles of elasticity theory as well as the main properties of the shape memory alloys

6.1. Ab-initio Calculation of Elastic Constants

NiTiHf. Then, the new developments are introduced in detail. Finally, I present the calculated elastic properties of NiTiHf alloys for different concentrations.

6.1 Ab-initio Calculation of Elastic Constants

The contents of this section follows Chapter 8 of Ref. [86]. Elasticity is the property of a solid material to regain its original shape after being deformed under the application of an external force. In such conditions, each part of the body exerts internal forces on neighboring parts. If the forces are proportional to the area of the surface of the given part, the force per unit area is called the *stress*. Here we only consider homogeneous stresses which means the forces acting on the surface are independent of the position of the particles in the body. In general, stress depends in the direction on the body and, therefore, is expressed as a second-rank tensor as follows,

$$\underline{\sigma} = \begin{bmatrix} \sigma_{11} & \sigma_{12} & \sigma_{13} \\ \sigma_{21} & \sigma_{22} & \sigma_{23} \\ \sigma_{31} & \sigma_{32} & \sigma_{33} \end{bmatrix}. \quad (6.1)$$

Here the underline notation is used to indicate a second-rank tensor. Note that σ_{ij} is the force component in direction $+x_i$ which is transmitted from the face that is perpendicular to $+x_j$.

The deformations are caused by an exerted strain which is described by the strain tensor. If u_i is the displacement of a point along x_i in a deformed solid, the strain tensor is then defined as

$$\epsilon_{ij} = \frac{1}{2} \left(\frac{\partial u_i}{\partial x_j} + \frac{\partial u_j}{\partial x_i} \right), \quad (6.2)$$

$$\underline{\epsilon} = \begin{bmatrix} \epsilon_{11} & \epsilon_{12} & \epsilon_{13} \\ \epsilon_{21} & \epsilon_{22} & \epsilon_{23} \\ \epsilon_{31} & \epsilon_{32} & \epsilon_{33} \end{bmatrix}. \quad (6.3)$$

The diagonal components are called tensile strains, whereas the non-diagonal components are denoted as shear strains. In absence of body torques both strain and stress tensors are symmetric.

The most general relationship connecting stress with strain is provided by the generalized version of Hooke's law. It states that for a sufficiently small stress, the amount of strain is linearly proportional to the magnitude of the applied stress,

$$\underline{\sigma} = \underline{\underline{C}} \underline{\epsilon}. \quad (6.4)$$

Chapter 6. Calculating Elastic Constants of NiTi_(1-x)Hf_x Alloys

In this equation, since stress and strain are second-rank tensors, $\underline{\underline{C}}$ must be a fourth-rank tensor constant (indicated by a double-underline notation). It is known as *elastic stiffness tensor* and its elements are called the *elastic constants*. One can write Eq. (6.4) also in the following form,

$$\underline{\epsilon} = \underline{\underline{s}} \underline{\sigma} , \quad (6.5)$$

where $\underline{\underline{s}} = \underline{\underline{C}}^{-1}$ is called *elastic compliance tensor*. The explicit form of Eq. (6.4) is as follows

$$\sigma_{ij} = \sum_{k,l=1}^3 C_{ijkl} \epsilon_{kl} . \quad (6.6)$$

The elastic constants are fundamental materials parameters providing a detailed information on the mechanical properties of materials. The knowledge of these data enables prediction of mechanical behavior in many different situations. Since the strain and stress tensors are symmetric, the tensor $\underline{\underline{C}}$ fulfills the following symmetry conditions,

$$C_{ijkl} = C_{ijlk}, \quad C_{ijkl} = C_{jikl}, \quad (6.7)$$

which reduces the number of independent elastic constants from 81 to 36. Additionally, using Eq. (6.6) and the following equation [86]

$$\sigma_{ij} = \frac{\partial \mathcal{W}}{\partial \epsilon_{ij}} , \quad (6.8)$$

in which \mathcal{W} is the free energy of the system, one can find C_{ijkl} as follows

$$C_{ijkl} = \frac{\partial}{\partial \epsilon_{kl}} \frac{\partial}{\partial \epsilon_{ij}} \mathcal{W} . \quad (6.9)$$

The order of derivatives can be changed. Hence,

$$C_{ijkl} = C_{klij} , \quad (6.10)$$

which reduces the number of independent elastic constants to 21.

Using *Voigt's* notation [86] one can represent the fourth-rank tensor of elastic constants in matrix form. Voigt's notation is introduced in the following way:

$$xx \rightarrow 1, \quad yy \rightarrow 2, \quad zz \rightarrow 3, \quad yz \rightarrow 4, \quad xz \rightarrow 5, \quad xy \rightarrow 6, \quad (6.11)$$

$$\begin{bmatrix} \sigma_{11} & \sigma_{12} & \sigma_{13} \\ \sigma_{21} & \sigma_{22} & \sigma_{23} \\ \sigma_{31} & \sigma_{32} & \sigma_{33} \end{bmatrix} = \begin{bmatrix} \sigma_1 & \sigma_6 & \sigma_5 \\ \sigma_6 & \sigma_2 & \sigma_4 \\ \sigma_5 & \sigma_4 & \sigma_3 \end{bmatrix} \Rightarrow \begin{bmatrix} \sigma_1 \\ \sigma_2 \\ \sigma_3 \\ \sigma_4 \\ \sigma_5 \\ \sigma_6 \end{bmatrix} , \quad (6.12)$$

6.1. Ab-initio Calculation of Elastic Constants

$$\begin{bmatrix} \epsilon_{11} & \epsilon_{12} & \epsilon_{13} \\ \epsilon_{21} & \epsilon_{22} & \epsilon_{23} \\ \epsilon_{31} & \epsilon_{32} & \epsilon_{33} \end{bmatrix} = \begin{bmatrix} \epsilon_1 & \frac{1}{2}\epsilon_6 & \frac{1}{2}\epsilon_5 \\ \frac{1}{2}\epsilon_6 & \epsilon_2 & \frac{1}{2}\epsilon_4 \\ \frac{1}{2}\epsilon_5 & \frac{1}{2}\epsilon_4 & \epsilon_3 \end{bmatrix} \Rightarrow \begin{bmatrix} \epsilon_1 \\ \epsilon_2 \\ \epsilon_3 \\ \epsilon_4 \\ \epsilon_5 \\ \epsilon_6 \end{bmatrix}. \quad (6.13)$$

Thus, Hooke's law can be written in matrix form as:

$$\begin{bmatrix} \sigma_1 \\ \sigma_2 \\ \sigma_3 \\ \sigma_4 \\ \sigma_5 \\ \sigma_6 \end{bmatrix} = \begin{bmatrix} C_{11} & C_{12} & C_{13} & C_{14} & C_{15} & C_{16} \\ & C_{22} & C_{23} & C_{24} & C_{25} & C_{26} \\ & & C_{33} & C_{34} & C_{35} & C_{36} \\ & & & C_{44} & C_{45} & C_{46} \\ & & & & C_{55} & C_{56} \\ & & & & & C_{66} \end{bmatrix} \begin{bmatrix} \epsilon_1 \\ \epsilon_2 \\ \epsilon_3 \\ \epsilon_4 \\ \epsilon_5 \\ \epsilon_6 \end{bmatrix}. \quad (6.14)$$

Due to the lattice symmetry of the crystal, the number of independent elastic constants may reduce even further. For instance, in case of triclinic lattice which has the lowest symmetry there are 21 independent elastic constants, while for a cubic lattice which has the highest symmetry there are only three independent elastic constants. In the following, the form of the matrix for both cubic and monoclinic (with $\gamma \neq 90^\circ$) lattices, which are the two phases of NiTiHf studied in this chapter, are shown.

$$C_{cubic} = \begin{bmatrix} C_{11} & C_{12} & C_{12} & 0 & 0 & 0 \\ & C_{11} & C_{12} & 0 & 0 & 0 \\ & & C_{11} & 0 & 0 & 0 \\ & & & C_{44} & 0 & 0 \\ & & & & C_{44} & 0 \\ & & & & & C_{44} \end{bmatrix}, \quad (6.15)$$

$$C_{monoclinic} = \begin{bmatrix} C_{11} & C_{12} & C_{13} & 0 & 0 & C_{16} \\ & C_{22} & C_{23} & 0 & 0 & C_{26} \\ & & C_{33} & 0 & 0 & C_{36} \\ & & & C_{44} & C_{45} & 0 \\ & & & & C_{55} & 0 \\ & & & & & C_{66} \end{bmatrix}. \quad (6.16)$$

In principle, there are two ways of calculating elastic constants of a single crystal using *ab initio* methods: the energy-strain approach and the stress-strain approach. In this chapter, the energy-strain approach has been applied for calculating elastic constants of NiTiHf alloys. This approach is based on computed total energies of properly selected deformed states of the crystal. From Eq. (6.8),

one can see that the work done by the stress component σ_i on a distorted structure, which is subjected to a small homogeneous strain with component ϵ_i , is obtained by

$$W = \frac{1}{2} \sum_{ij} C_{ij} \epsilon_i \epsilon_j. \quad (6.17)$$

For each strain type, several magnitudes of strains are applied and the corresponding total energies are computed with an *ab initio* approach. The elastic constant is then derived from the curvature of the energy-strain relation by means of a least-squares fit making use of Eq. (6.17). Some of the applied strains may be related to a single elastic constant while others are described by a linear combination of elastic constants, from which the elastic constant tensor is finally constructed. The number of necessary distortions is given by the number of independent elastic constants.

6.1.1 Polycrystalline Elastic Constants

In a polycrystalline material, the single crystalline grains are randomly oriented. On a large scale, such materials can be considered to be isotropic in a statistical sense. An isotropic system is completely described by the bulk modulus B and the shear modulus G [20]. Young's modulus and the Poisson ratio can be obtained from B and G as follows,

$$E = \frac{9BG}{3B + G}, \quad (6.18)$$

$$\nu = \frac{3B - 2G}{2(3B + G)}. \quad (6.19)$$

In order to calculate the polycrystalline elastic moduli, there are different methods that calculate these moduli by averaging the single crystal elastic constants c_{ij} . The three most widely used are the Voigt [87], the Reuss [88] and the Hill [89, 90] averaging methods. In the Voigt averaging method a uniform strain is assumed, while in the Reuss method a uniform stress is considered. Within the Voigt approach, the general expressions for the bulk and shear moduli are [20]

$$B_V = \frac{(C_{11} + C_{22} + C_{33}) + 2(C_{12} + C_{13} + C_{23})}{9}, \quad (6.20)$$

$$G_V = \frac{(C_{11} + C_{22} + C_{33}) - (C_{12} + C_{13} + C_{23}) + 3(C_{44} + C_{55} + C_{66})}{15}. \quad (6.21)$$

For the Reuss method the corresponding equations are

$$B_R = \frac{1}{(s_{11} + s_{22} + s_{33}) + 2(s_{12} + s_{13} + s_{23})}, \quad (6.22)$$

6.2. NiTiHf: A High Temperature Shape Memory Alloy

$$G_R = \frac{15}{4(s_{11} + s_{22} + s_{33}) - 4(s_{12} + s_{13} + s_{23}) + 3(s_{44} + s_{55} + s_{66})}. \quad (6.23)$$

Hill has shown that the Voigt and Reuss elastic moduli are the strict upper and lower bound, respectively. Thus, the Hill-averaged bulk and shear moduli can be determined from these upper and lower limits as

$$B_H = \frac{1}{2}(B_V + B_R), \quad (6.24)$$

$$G_H = \frac{1}{2}(G_V + G_R). \quad (6.25)$$

There are also two anisotropy ratios which will be reported in this chapter. The first one is the Zener anisotropy ratio, A , which for cubic materials is defined by the following equation

$$A = \frac{2C_{44}}{C_{11} - C_{12}} = \frac{C_{44}}{C'}. \quad (6.26)$$

Another anisotropy is defined by shear moduli for any type of symmetry as follows

$$A_{VR} = \frac{G_V - G_R}{G_V + G_R}. \quad (6.27)$$

Both of these ratios conceptually state to what extent the material is isotropic. For completely isotropic materials A is equal to 1, while A_{VR} equals to 0. For most metals, except some exceptions, $A_{VR} \leq 20\%$ [20].

6.2 NiTiHf: A High Temperature Shape Memory Alloy

Shape memory alloys (SMAs) are a unique category of smart materials with the ability of a shape memory effect (SME) and superelasticity (SE). The SME is described as the ability of the material to recover any deformation by heating and return to its original shape, while SE is the ability of recovery from unusually large strains. These unique behaviors are due to reversible phase transformations which occur under application of stress or heat.

In SMAs, there are usually two main phases, the high-temperature phase, austenite, and the low-temperature phase, martensite. The phase transformation occurring between these two phases is called martensitic phase transformation, which is a diffusionless transformation type. Such a phase transformation occurs by shear lattice deformation, instead of diffusion of atoms. When the temperature is decreased in absence of stress, the crystal structure changes from austenite

to martensite, which is called the *forward* transformation. By heating the material, the crystal structure transforms back to austenite, which is called *reversed* transformation. The temperature at which the forward transformation starts is called *martensitic start temperature* (M_s) and the temperature of finishing the forward transformation is called *martensitic finish temperature* (M_f). The same temperatures are defined for the reverse transformation as *austenitic start temperature* (A_s) and *austenitic finish temperature*. There are two forms of martensitic phases in SMAs: *twinned* martensite, which is formed by a combination of different martensitic single crystals called *variants*, and *detwinned* or reoriented martensite, which is deformed by a specific dominant variant. In case of forward and reverse transformation, which are only due to the changes of temperature, the transformations are in between austenite and twinned martensite phases. The detwinned phases may also form during these phase transformations.

Under application of an external stress on the twinned martensite phase, the SMA transforms to a detwinned martensite phase. By heating up the deformed material, the detwinned martensite will transform to austenite, and therefore it regains its original shape. The transformation is also possible by applying a very large mechanical stress to the austenite phase above A_f , leading to the transformation to the martensite phase. By removing the external forces the SMA will return to its original shape by a reverse phase transformation. This effect is called superelasticity or *pseudo-elastic effect*.

Among the various SMAs system, NiTi is highly interesting due to a number of unique characteristics such as its operating temperature which is near room temperature, high ductility and low elastic anisotropy. These properties together with low costs have created interests in industrial applications such as automotive, aerospace, and biomedical industries. One important aim in NiTi alloys is to raise the martensitic transformation temperature in order to be applicable for high temperature applications of the shape memory effect. This usually is done by adding Pt, Pd, Zr or Hf to NiTi [91]. Among them, NiTiHf alloys are most attractive, due to the good thermal stability and low cost, and therefore it seems to be the most encouraging alloy for a wide range of applications in the critical 100 – 300°C temperature range [92]. Among the possible compositions, the Ni-rich alloys in which Hf is added at the expense of Ti, are most promising. For a Hf content lower than 10 at-% the transformation temperatures do not increase much, but from 10 at-%Hf they tend to increase linearly up to 525°C for 30 at-% Hf. In contrast for Ni-lean alloys they do not change notably until 50 at-%Hf in which the transformation temperatures drop steeply [93]. In comparison with pure NiTi, the ductility is decreased for NiTiHf alloys, but for Ni-rich alloys this reduction is less pronounced than for other compositions. This property together with lower hysteresis presents another advantage of Ni-rich alloys over other possible compositions [93].

6.3. NiTi Structures and Details of Calculations

The investigation of elastic constants is a way to obtain important insights into mechanical properties of these alloys. Due to the impossibility of growing single crystals of these alloys in different phases, only little experimental data for pure NiTi phases has been available in the past decades. This makes the investigation of the elastic constants of NiTiHf alloys by *ab initio* methods highly desirable. Apart from this technological aspect, another goal of this study is to make EMTO-CPA code able to produce reliable results for lower symmetry crystals like monoclinic $B19'$ and then to calculate the elastic properties of $\text{NiTi}_{1-x}\text{Hf}_x$ alloys as a function of concentration x .

6.3 NiTi Structures and Details of Calculations

The parent phase of all NiTi-based alloys, austenite, has a cubic $B2$ (ordered body centered cubic) structure with space group $Pm\bar{3}m$ [94]. The crystal structure of the martensite phase is monoclinic with space group $P2_1/m$ which is called $B19'$. It has been confirmed by experiment and theory as the low-temperature phase of NiTi [95–98]. There are also intermediate phases observed experimentally during the martensitic transformation [99], but they are not investigated here. Table 6.1 shows the crystallographic data of two phases $B2$ and $B19'$. Note that in some literature, a larger tetragonal four-atom cell is used for representing $B2$ phase for a better comparison with $B19'$ phase, but here we use the conventional cubic unit cell with two atoms.

The equilibrium lattice parameter and elastic properties of $\text{NiTi}_{(1-x)}\text{Hf}_x$ ($x=0, 0.1, 0.2, 0.3, 0.4, 0.5$) have been calculated in both $B2$ and $B19'$ phases by means of the EMTO-CPA code. Since this code is not equipped for atomic coordinate relaxations, we have taken these data for $B19'$ structure from Ref. [101] obtained by the *WIEN2k* code. These are (0.6708, 0.0655, 0.25) and (0.2150, 0.3842, 0.25) for Ni and Ti, respectively, which are in a good agreement with experimental data in Table 6.1. Note that these data has been used for all values of Hf concentration x because, as it was mentioned in Section 4.6, CPA can not account for calculating local atomic relaxations.

For the \mathbf{k} -space integration, for $B2$ structure a $34 \times 34 \times 34$ mesh and for $B19'$ structure a $12 \times 14 \times 22$ mesh has been used. In all calculations, the $3d^8 4s^2$ states of Ni, the $3d^2 4s^2$ states of Ti and $4f^{14} 5d^2 6s^2$ states of Hf were treated as valence electrons. The relative ratio of the atomic spheres radii has been

¹There are two different choices of axes in a monoclinic crystal system. In the first setting, the unique axis is parallel to c and the monoclinic angle is γ . In the second one, the unique axis is parallel to b and β is the monoclinic angle. In this thesis, we use the first setting to represent the $B19'$ structure.

Table 6.1: Experimental crystallographic data of the two phases *B2* and *B19'* of NiTi.

Phase (Space group)	Lattice parameters and monoclinic angle	atomic parameters			
		atom	x	y	z
<i>B2</i> (<i>Pm</i> $\bar{3}$ <i>m</i>) ^a	a=3.013 (Å)	Ni	0	0	0
		Ti	0.5	0.5	0.5
<i>B19'</i> (<i>P2</i> ₁ / <i>m</i>) ^b	a=4.646 (Å)	Ni	0.6752	0.0372	0.25
	b=2.898 (Å)	Ti	0.2164	0.4176	0.25
	c=4.108 (Å)				
	γ=97.78°				

^a Ref. [100]^b Ref. [96]

chosen equal to $r_{(Ti,Hf)}/r_{Ni} = 1.125$. On the one hand, this value was chosen to approximate the potential more realistically and on the other hand to treat the charge transfer effect properly. Note that this ratio has been kept fixed for all values of Hf concentration x . For calculating the energy dependent slope matrix and its first energy derivative during the self-consistent calculations, a 6th-order Taylor expansion with expansion center $\omega_0 = 0$ was used. The exchange-correlation potential was treated by the PBE functional [48].

The on-site screening constants α_{scr} and β (described in Section 4.6) are determined using the LSGF calculations as described in Refs. [72, 73]. The values $\alpha_{Scr}^{Ti} = \alpha_{Scr}^{Hf} = 0.650$ and $\beta = 1.000$ calculated by A. V. Ruban have been applied in all EMTO-CPA calculations. It should be noted that these constants vary very little with alloy compositions and lattice constants [72, 73]. Thus, these values have been used for all values of $x > 0$ in both *B2* and *B19'* structures.

The equilibrium properties of *B2* structure have been obtained by volume optimization using a Birch-Murnaghan equation of state fitting. The procedure used for calculating the equilibrium lattice parameters a_0 , b_0 and c_0 and the monoclinic angle γ_0 of the *B19'* structure is as follows. In the first step, the equilibrium volume V_0 has been calculated with fixed values for b/a , c/a and γ using a Birch-Murnaghan equation of state fitting. The initial values for b/a , c/a and γ were taken from the available experimental data. Then the optimum values for b/a , c/a and γ have been obtained by varying each parameter independently and calculating the minimum of the graph of the total energy as a function of that parameter using a polynomial fitting. All the calculations performed for

optimizing these three parameters are volume-conserving with fixing the volume at V_0 . First, b/a has been optimized with fixed initial values for c/a and γ , then c/a with fixed calculated value of the equilibrium b/a and initial value of γ , and finally γ with fixed calculated values of equilibrium b/a and c/a .

6.4 Details of the New Developments

In order to improve the efficiency and accuracy of the calculations, specifically elastic constants calculations, a number of new implementations and modifications have been developed within the EMTO-CPA code. One part of these have been done to facilitate preparation of the required input files and automatize post-processing calculations using the output files, and the other parts concern the improvement of accuracy of the results by improving the smoothness of energy-strain graphs. In the following, I will describe these developments.

The first modifications have been done within the `kstr` package. Here, the routine responsible for generating spherical harmonics which is used for computing Madelung matrices has been changed to an updated version which in contrast to the old routine yields reliable results also for high ls . Next, the routines responsible for the slope matrix calculations have been updated using the *linear algebra package* (LAPACK). To this end, the *math kernel library* (MKL) has been used with option of shared memory parallelization (*OpenMP*) of routines such as matrix factorization, inversion and matrix-matrix multiplication. This can decrease the run time of this program significantly. For instance, for the $B19'$ structure, the new version is at least 10 times faster than the old version.

6.4.1 Application of the ElaStic Package

The **ElaStic** software² [25] is an open-source code developed at the Materials Center Leoben (MCL) Forschung GmbH, which allows one to obtain second-order elastic compliance tensors for all crystal lattice types from *ab initio* calculations. It is utilizing codes such as Wien2k, VASP, exciting, Quantum Espresso and recently EMTO-CPA code. This interface for EMTO-CPA code developed by T. Dengg³ has been applied for calculating elastic properties of $\text{NiTi}_{1-x}\text{Hf}_x$ alloys. It generates the required input files including the one containing basis vectors and atomic positions of deformed structures for different types of strains. After all

²<https://www.mcl.at/en/software/elastic/>

³Materials Center Leoben Forschung GmbH, A-8700 Leoben, Austria

calculations are performed, **ElaStic** will calculate the elastic constants and polycrystalline elastic moduli from the total energies output files using the method discussed in Section 6.1. For this part, **ElaStic** enables to calculate and plot the cross-validation score and second derivatives of total energy as a function of strain, which can be applied to check quality of fitting, energy trends and convergence of calculations.

For calculating the elastic constants of NiTi_{1-x}Hf_x for each concentration x , we have calculated 41 deformed structures for every strain type within the interval $|\epsilon| \leq 0.05$. As it was mentioned in Section 6.1, the number of strain types needed to fully determine the elastic constants tensor is equal to the number of independent elastic constants. Thus, considering Eq. (6.15) and Eq. (6.16), there are three types of deformations for the $B2$ structure and thirteen types for the $B19'$ structure.

6.4.2 Application of the *Voro*-shape Package

The method of tessellation of the space described in Subsection 4.5.1 works flawlessly except when the symmetry decreases, for instance in case of low symmetry crystals or deformed structures. In this case, the sum of the tetrahedra volumes is not exactly equal to the volume of the partitioned cell. Thus, the integrations in the *FCD* technique can not be calculated exactly. This can cause the appearance of discontinuous jumps in total energy versus strain graphs for different strain types and consequently unreliable elastic constants.

In order to overcome inaccuracies arising from these problems, a *shape* package (hereafter referred to as *voro-shape*) has been developed by H. Ehteshami⁴ based on *voro++*⁵ [102], an open source software library for carrying out three-dimensional computations of the *Voronoi tessellation*. First, this package has been modified to keep the relative ratio of atomic sphere radii fixed, and then has been applied for all the calculations on $B2$ and $B19'$ phases. In Figure 6.1, the effect of using this package in comparison with the old shape package is shown for some selected deformation types of pure NiTi at $B19'$ phase. As one can see, the graphs obtained by the old shape package are characterized by occasional discontinuous jumps in the total energy, while using the *voro-shape* package has improved the smoothness of the curves. It is also observed that for other concentrations ($x > 0$), the graphs of most deformation types obtained by the old shape package are even more problematic, but the *voro-shape* package yields smoother

⁴Department of Materials Science and Engineering, KTH Royal Institute of Technology, SE-100 44 Stockholm, Sweden

⁵<http://math.1bl.gov/voro++/about.html>

6.4. Details of the New Developments

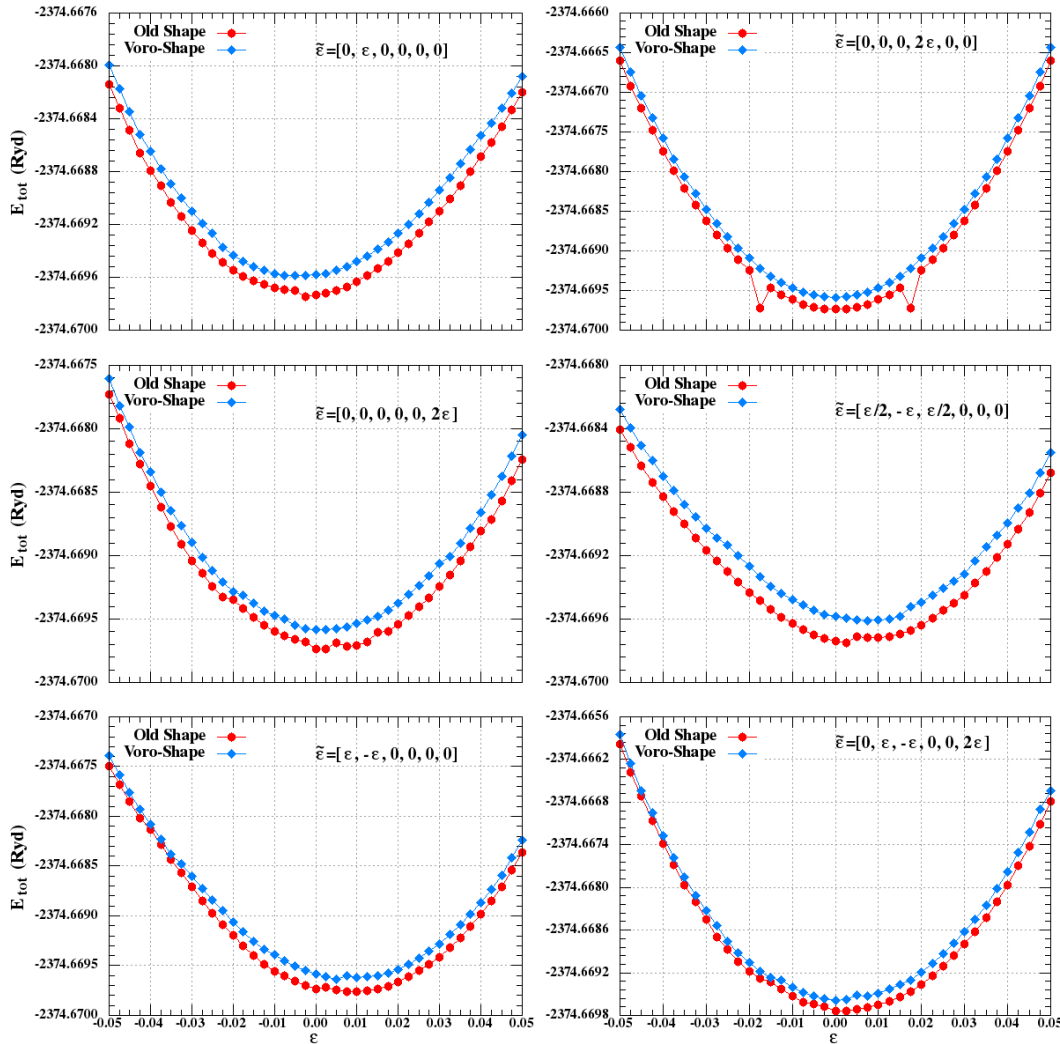


Figure 6.1: The total energy versus strain using old shape and voro-shape programs for some selected deformation types of pure NiTi in $B19'$ phase.

energy curves.

6.4.3 Modification on Radial Mesh Points

Although using the *voro-shape* package has improved the graphs of total energy versus strain, there are still some points with discontinuous jumps. These points are shown in Figure 6.1 for some selected deformation types of pure NiTi in $B19'$ phase. Further investigation to find the source of this behavior revealed that for the strains where the discontinuous jumps take place, the number of radial mesh points inside the inscribed spheres changes. The number of these mesh points

that are used to solve the *Dirac* equation alters due to changes of inscribed sphere radii which in turn is a result of deforming the structure.

Although we could not identify the source of this problem, we have found that keeping the number of the radial mesh points for both atoms Ni and Ti(Hf) unchanged, can cure the energy trends at these points. Therefore, a new mode of calculations (hereafter referred to as *FRMS* mode) has been implemented within the code that enables one to keep the number of these mesh points fixed for all strained structures of a certain deformation type, and that is equal to the minimum number of radial mesh points of all distorted structures. This value for

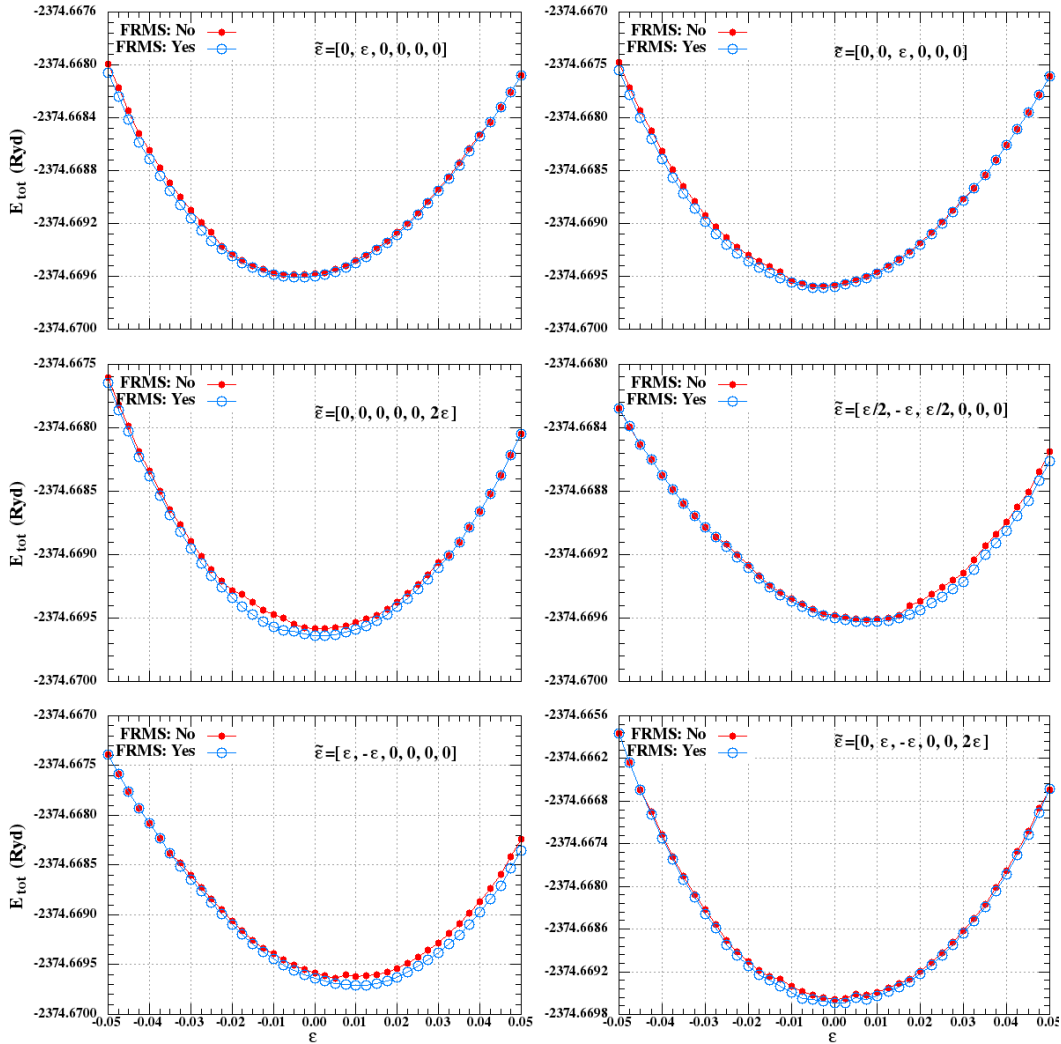


Figure 6.2: The total energy versus strain using voro-shape program in *FRMS* mode compared to normal mode for some selected deformation types of pure NiTi in *B19'* phase.

every site in the unit cell corresponds to a structure that has the minimum fraction of inscribed sphere radius to the Wigner-Seitz radius. Figure 6.2 shows the improvement of the total energy versus strain graphs using *FRMS* calculations. Note that we have applied *FRMS* calculations only for the *B19'* structure.

6.5 Results

In this section, we report the results of our calculations. The computational details have been discussed in Section 6.3. For all the calculations here, either the equilibrium structural or elastic properties, the developments discussed in the previous section have been applied for both *B2* and *B19'* phases, except the *FRMS* mode which has been used only for calculating elastic constants in the *B19'* phase.

6.5.1 Structural Parameters of $\text{NiTi}_{1-x}\text{Hf}_x$

Table 6.2 summarizes our calculated equilibrium structural properties of pure NiTi in both *B2* and *B19'* phases using the EMTO method compared to some available computational and experimental results in literature. Among the computational works referenced in this table, Ref. [101] and Ref. [103] are based on full potential methods, while in Ref. [104] a projector-augmented-wave (PAW) method has been used. For all these computational results, similar to our calculations, PBE-GGA has been applied for the exchange-correlation functional. Note that the experimental data for *B2* phase by Sittner et al. [100] was measured at 300 K which is close to 292 K, the lowest temperature which the *B2* phase is stable and the experimental data for *B19'* [96] was measured at the room temperature. It should be noted that all calculated values are for $T=0$ K, and no temperature effects have been taken into account.

As one can see from this table, EMTO overestimates the unit cell volume of the *B2* phase by 0.3% (or equivalently the lattice parameter by $\approx 0.1\%$) compared to the experimental data. Among the other computational results, Ref. [103] also overestimates the unit cell volume of this phase, while Refs. [101, 104] underestimate it compared to the experimental data. However, for the *B19'* phase all computational methods, including EMTO, overestimate the unit cell volume. For this phase, EMTO gives the largest unit cell volume with 3.3% overestimation compared to the experimental data. Among the calculated lattice constants of *B19'* phase using EMTO, c_0 has the largest difference compared to the other computational results and has the major contribution in the unit cell

Table 6.2: Equilibrium lattice parameter (\AA) and unit cell volume (\AA^3) of NiTi in $B2$ phase and equilibrium lattice parameters, unit cell volume divided by 2 (for a better comparison with $B2$ phase) and monoclinic angle γ (degree) in $B19'$ phase of pure NiTi compared to the other computational results and experimental data. In all of the computational methods referenced here, the PBE-GGA has applied for exchange-correlation functional.

		This work	Theory[101]	Theory[104]	Theory[103]	Exp
		EMTO	FLAPW+lo WIEN2k[8]	PAW VASP[9-11]	FLAPW[105]	
$B2$	a_0	3.016	3.008	3.008	3.019	3.013[100] ^a
	V_0	27.43	27.22	27.22	27.52	27.34[100] ^a
$B19'$	a_0	4.704	4.784	4.685	4.674	4.646[96] ^b
	b_0	2.939	2.943	2.941	2.919	2.898[96] ^b
	c_0	4.180	4.028	4.035	4.085	4.108[96] ^b
	γ	101.57	102.76	97.78	99.09	97.78[96] ^b
	$V_0/2$	28.31	27.66	27.54	27.52	27.40[96] ^b

^a Experiment [100] at 300 K

^b Experiment [96] at room temperature

overestimation. Compared to the experimental data, one can also see that it is only EMTO that overestimate c_0 . The larger error of the EMTO results for the equilibrium structural properties of $B19'$ phase compared to $B2$ phase could be due to two factors. First, as it was mentioned before, because the EMTO code is not equipped for atomic coordinate relaxations, we have instead taken these data from Ref. [101] which can cause inconsistencies in the calculations. Second, it could be due to the procedure of the current implementation in which the FCD technique is used only once at the end of the calculations after convergence of the SCA self-consistent cycle. This gives less accurate results for low symmetry crystals, because in such cases the non-spherical part of the potential, which is missing in SCA, has more influence on the properties of the crystal.

Next we present our results for the unit cell volume of $B2$ and $B19'$ phases as a function of Hf concentration in Figure 6.3. From literature, experimental results are only available for the $B19'$ phase, which have been added to this graph. The experimental data for pure NiTi ($x = 0$) in this figure is the one reported in Table 6.2, while the data for other values of x has been taken from Ref. [91]. As one can see from this graph, the calculated unit cell volume of both phases

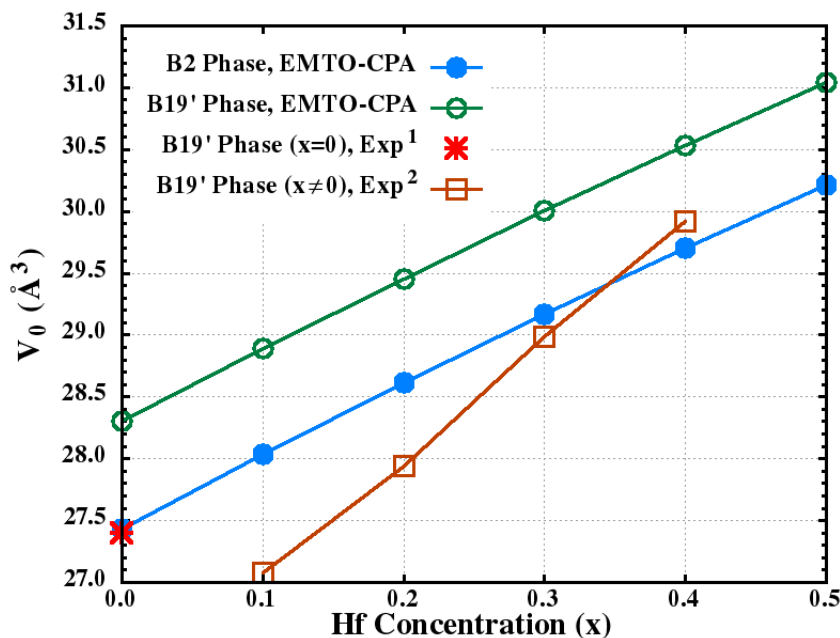


Figure 6.3: The calculated unit cell volumes of $\text{NiTi}_{1-x}\text{Hf}_x$ as a function of Hf concentration x for $B2$ phase and $B19'$ phase divided by 2 in comparison with $B19'$ experimental data (Exp¹ from Ref. [96] for pure NiTi and Exp² from Ref. [91] for $(x \neq 0)$).

increases linearly by raising the Hf concentration which is expected because Hf has a larger atomic radius. In the case of the $B19'$ phase, this is in agreement with the shown experimental data in this graph and also experimental observation in Ref. [106]. Although the experimental data points suggest a non-monotonous behavior between $x = 0$ and $x = 0.1$, such a conclusion is not robust, because these data points have been taken from two different measurements and there is no available experimental data in the range of $0 < x < 0.1$. From the results for $B19'$ phase in this figure, one can also see that the EMTO-CPA calculations underestimate the volume increase from $x = 0.1$ to $x = 0.4$ by $\approx 50\%$ compared to the experimental data.

Figure 6.4 shows the calculated lattice parameters and the monoclinic angle of $\text{NiTi}_{1-x}\text{Hf}_x$ in $B19'$ phase as a function of x compared to available experimental data. As one can see from these graphs, EMTO-CPA calculations yield increasing values for all lattice parameters and the monoclinic angle as a function of Hf content with almost linear trends. For a_0 , b_0 and γ , this is in agreement with experimental data. The amount of calculated variations for these structural properties from $x = 0.1$ to $x = 0.4$ have been underestimated compared to experimental data. However, for c_0 the trend of EMTO-CPA and experimental data are in contradiction. This disagreement for c_0 can be a consequence of CPA limitations such as the lack of local atomic relaxations. Remember that here again

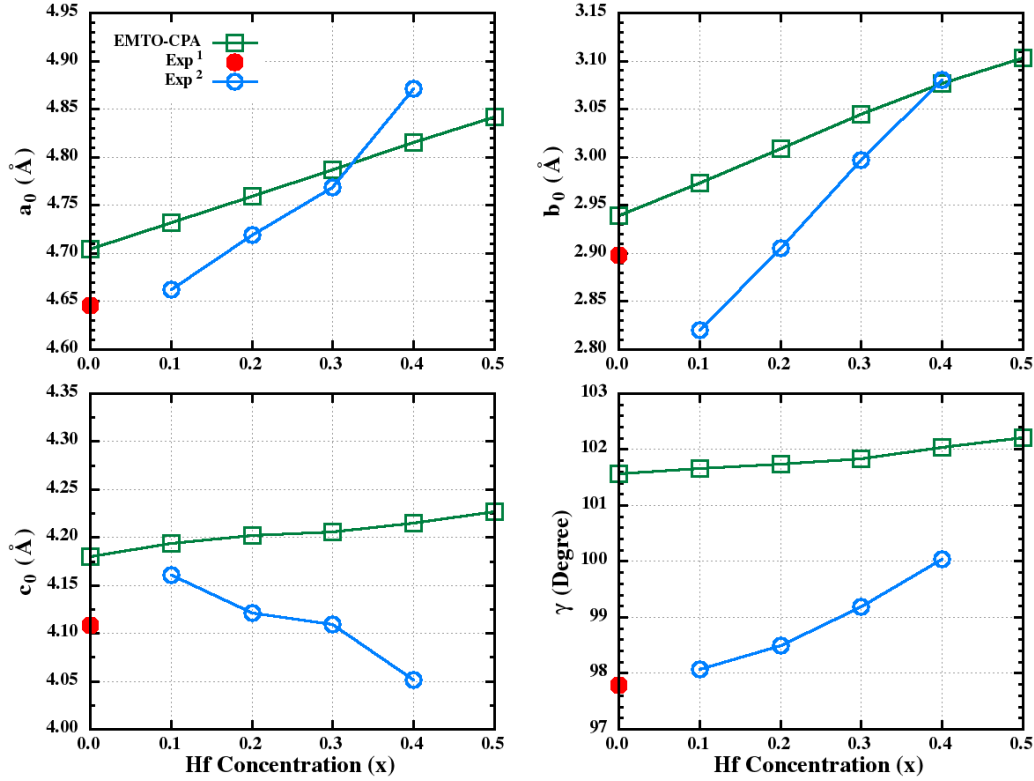


Figure 6.4: The calculated lattice parameters and the monoclinic angle of NiTi_{1-x}Hf_x as a function of Hf concentration x compared to the experimental results. Exp¹ data are those repeated in Table 6.2 taken from Ref. [96] and Exp² data are taken from Ref. [91].

the experimental data of $x = 0$ and $x = 0.1$ are from two different measurements and therefore, one cannot deduce any result from the changes within this range of Hf concentration.

6.5.2 Elastic Properties of NiTi_{1-x}Hf_x

We have calculated the elastic properties of NiTi_(1-x)Hf_x in both $B2$ and $B19'$ phase based on the computed equilibrium structures. The computational details have been described in Sections 6.3 and 6.4. In Table 6.3, we list the calculated and experimental elastic constants for pure NiTi in $B2$ phase. Here, C' has been obtained by means of C_{11} and C_{12} using the well-known equation $C' = (C_{11} - C_{12})/2$ for cubic structures.

Elastic constants usually decrease with increasing temperature. In general, this is mainly due to the lattice expansion which softens the elastic properties

Table 6.3: Calculated elastic constants, shear moduli C' and bulk modulus B (all moduli in (GPa)) of pure NiTi in B2 phase compared to other computational results and experimental data. B is calculated by applying the Birch-Murnaghan fit.

	This work	Theory[101]	Theory[104]	Theory[103]	Exp ^a	Exp ^b
	EMTO	FLAPW+lo WIEN2k[8]	PAW VASP[9-11]	FLAPW[105]		
C_{11}	203	173	138	183	162	137
C_{12}	135	157	169	146	129	120
C'	34	8	-16	19	16	8
C_{44}	56	50	40	46	34	34
B	158	161	159	159	142	126

^a Experiment [107] at 298 K

^b Experiment [108] at 400 K

of the crystals. Comparing the experimental results from Ref. [107] measured at 298 K, which is the lowest temperature of B2 phase to be stable, with Ref. [108] measured at 400 K shows this effect for C_{11} , C_{12} , C' and B . Since DFT calculations simulate ground-state properties of a material at 0 K and we have not taken into account any temperature effects or lattice vibrations for our calculations, our results are better comparable to the experimental data measured at 298 K. Comparing our results with these experimental data shows that C_{11} , C_{12} and C_{44} have been overestimated by 7%, 5% and 65%, respectively, which may be due to the neglect of temperature effect. Among the other computational results, Ref. [104] reported $C_{12} > C_{11}$ or equivalently $C' < 0$. This would mean that the B2 structure is unstable at zero K which is in agreement with experimental observation. However, the results of this work especially for C_{11} and C_{12} are quite different from other computational results, since it has reported the smallest value for C_{11} and the largest value for C_{12} compared to other computational results. For instance, comparing the experimental data for C_{11} at two different temperatures, one can expect that an ab initio DFT calculation yields a value larger than 162 GPa reported in Ref. [107]. While all the other computational results including EMTO-CPA yield a larger value as it is expected, Ref. [104] has reported 138 GPa which is obviously far from the expectation.

The polycrystalline elastic moduli of B2 structure are summarized in Table 6.4. Since for cubic structures $B_V = B_R = B_H$, only B_H is reported here. Among the other DFT results, the one from Ref. [104], which reported a fully unstable B2 phase, does not yield comparable results with experimental. The best results

Table 6.4: Calculated macroscopic elastic properties of NiTi in *B2* structure comparing with other computational results and experimental data. Only the Hill bulk modulus B_H is reported, because for cubic structures $B_V = B_R = B_H$. All moduli are given in GPa, except for A , A_{VR} , and ν_H which are dimensionless.

	This work	Theory[101]	Theory[104]	Theory[103]	Exp ^a	Exp ^b
	EMTO	FLAPW+lo WIEN2k[8]	PAW VASP[9–11]	FLAPW[105]		
A	1.63	6.32	-2.58	2.49	2.06	4.00
B_H	158	162	159	158	140	126
G_V	48	33	18	35	27	24
G_R	45	16	-93	29	24	15
G_H	46	25	-37	32	25	20
A_{VR}	3	35	-148	9	6	23
ν_H	0.37	0.43	0.63	0.41	0.41	0.43
E_V	130	94	51	98	76	67
E_R	123	47	-345	82	68	45
E_H	127	71	-123	90	72	56

^a Experiment [107] at 298 K^b Experiment [108] at 400 K

compared to experimental data have been reported from Ref. [101] calculated by WIEN2k. Our result for the bulk modulus is in a good agreement with experimental data and other DFT methods. It also agrees with the respective B value from Table 6.3, calculated from a Birch-Murnaghan fit, which shows consistency of results. The Young's and shear moduli are overestimated and the anisotropy ratios A and A_{VR} are underestimated compared to FLAPW and WIEN2k results and experimental data. For shear and Young's moduli, the error of the Reuss limit is larger than the Voigt limit.

Table 6.5 summarizes the elastic constants of pure NiTi in *B19'* structure compared to the other DFT results. There is no reported experimental data for elastic properties of this phase in literature. Among the other DFT results in this table, Refs. [104] and [103] have applied a stress-strain method for calculating elastic constants, while Ref. [101] similar to our work has applied a total energy-strain method. Hence, our results are more comparable with those in Ref. [101] calculated by WIEN2k. Overall comparison between the EMTO re-

Table 6.5: Calculated elastic constants and bulk modulus B (all moduli in (GPa)) of NiTi in $B19'$ structure comparing with other computational results. B is calculated by applying the Birch-Murnaghan fit.

	This work	Theory[101]	Theory[104]	Theory[103]
	EMTO	FLAPW+lo WIEN2k[8]	PAW VASP[9-11]	FLAPW[105]
C_{11}	281	254	223	249
C_{12}	122	104	99	107
C_{13}	121	136	129	129
C_{16}	22	21	-27	-15
C_{22}	180	180	200	212
C_{23}	198	151	125	125
C_{26}	-18	0	-4	1
C_{33}	245	248	241	245
C_{36}	-2	-6	9	3
C_{44}	92	91	76	87
C_{45}	-2	-3	4	4
C_{55}	97	93	77	86
C_{66}	49	5	21	66
B	155	158	152	159

sults and other DFT results in Table 6.3 and 6.5, shows that the accuracy of the EMTO results for most of the elastic constants of the low symmetry $B19'$ structure is in the same range as for the high symmetry $B2$ results. The largest difference between our results and WIEN2k results for the $B19'$ phase is for C_{23} and C_{66} . Other notably different results compared to WIEN2k results are for C_{11} , C_{12} , C_{26} and C_{13} . However, among them, C_{66} and C_{13} are better comparable with VASP and FLAPW results. For some constants such as C_{23} and C_{11} , the larger discrepancies with other computational results are likely due to factors such as taking the relaxed atomic coordinates from Ref [101] which causes inconsistency in calculations, or the influence of the non-spherical part of the potential on the properties of low symmetry $B19'$ structure, which is not taken into account properly within the current implementation of EMTO code. In addition, since the current implementation of the EMTO-CPA code is not equipped for atomic co-

Table 6.6: Calculated macroscopic elastic properties of NiTi in $B19'$ structure comparing with other computational results.

	This work	Theory[101]	Theory[104]	Theory[103]
	EMTO	FLAPW+lo WIEN2k[8]	PAW VASP[9–11]	FLAPW[105]
B_V	176	163	152	159
B_R	149	127	143	157
B_H	163	145	148	158
G_V	65	57	56	71
G_R	13	5	34	67
G_H	39	31	45	69
A_{VR}	67	84	24	3
ν_H	0.39	0.40	0.36	0.31
E_V	174	153	149	185
E_R	37	15	95	176
E_H	108	87	122	181

ordinate relaxations, we have kept the internal coordinates, taken from Ref [101] calculated for equilibrium structure, fixed at each lattice distortion. Among the other DFT results in this table, the ones obtained using WIEN2k and VASP, in contrast to FLAPW calculations, allowed internal coordinates optimization in their calculations at each lattice distortion.

The polycrystalline elastic moduli of the $B19'$ structure are listed in Table 6.6. As it is clear from this table, our calculations overestimate all the macroscopic moduli in Voigt, Reuss and Hill limits compared to WIEN2k results. This could be expected from our results for elastic constants in Table 6.5. However, in comparison to FLAPW results, EMTO underestimates the shear and Young's moduli.

Figure 6.5 shows the calculated elastic constants of NiTi_(1-x)Hf_(x) in $B2$ structure as a function of Hf concentration x . These graphs show that by increasing the Hf content, C_{11} increases from 204 GPa up to 222 GPa at $x = 0.2$ and then remains almost constant until $x = 0.5$. On the other, hand C_{12} decreases from 135 GPa at $x = 0$ to 114 GPa at $x = 0.5$. The trend of C' calculated by $C' = (C_{11} - C_{12})/2$ is quite similar to C_{11} so that it increases form 35 GPa at

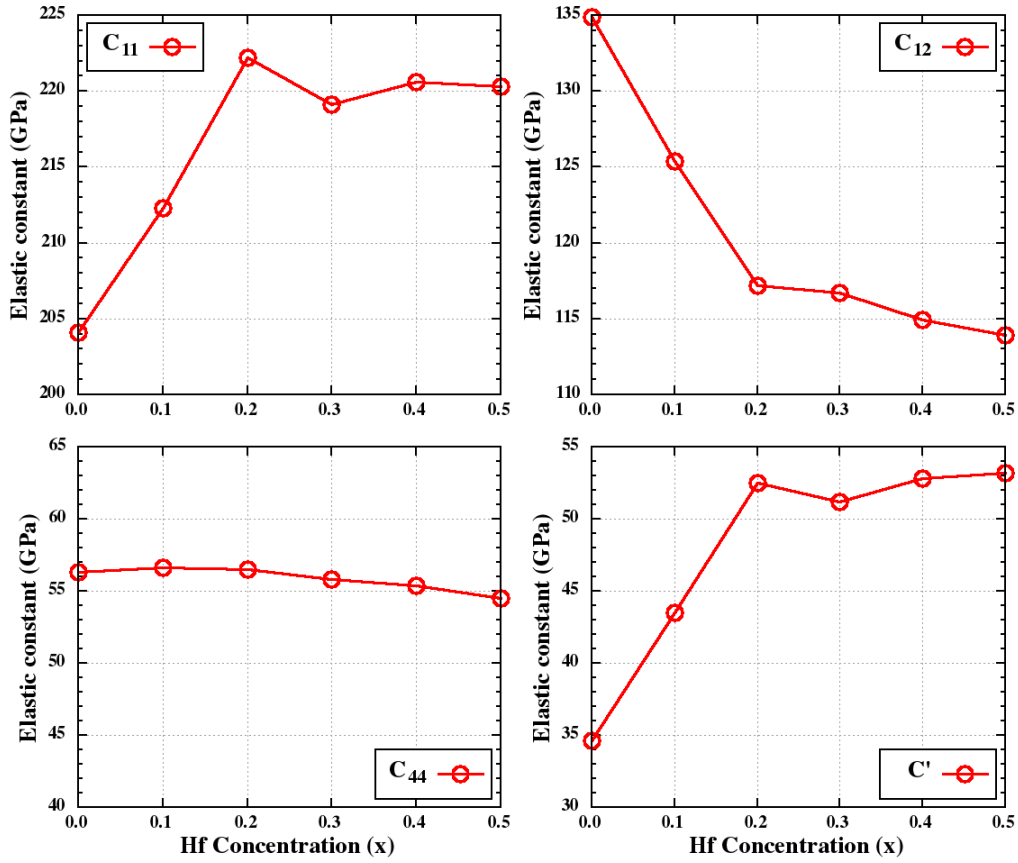


Figure 6.5: Elastic constants of $\text{NiTi}_{(1-x)}\text{Hf}_x$ in $B2$ structure as a function of Hf concentration x .

$x = 0$ to 53 GPa at $x = 0.2$ and then it remains constant. Finally, C_{44} does not show any considerable changes and reduces slightly from 56 GPa at $x = 0$ to 55 GPa $x = 0.5$.

Figure 6.6 demonstrates the Hill's macroscopic moduli and also Zener anisotropy ratio for $B2$ structure as a function of Hf concentration. One can see from this figure that B_H decreases from 158 GPa at $x = 0$ to 149 GPa at $x = 0.5$, while for shear and Young's moduli there are steep increases from $x = 0$ until $x = 0.2$ and then remain almost constant. In the left upper panel B is calculated by a Birch-Murnaghan fit. Both B and B_H show similar trends by increasing Hf content and their maximum difference is 2 GPa at $x = 0.2$ which shows consistency of results. Last graph shows that the Zener anisotropy ratio decreases from ≈ 1.6 to ≈ 1.0 . Although this ratio for $x = 0$ is underestimated compared to the experimental value (shown in Table 6.4), considering only the trend of this graph shows that increasing Hf content makes the $B2$ structure mechanically more isotropic.

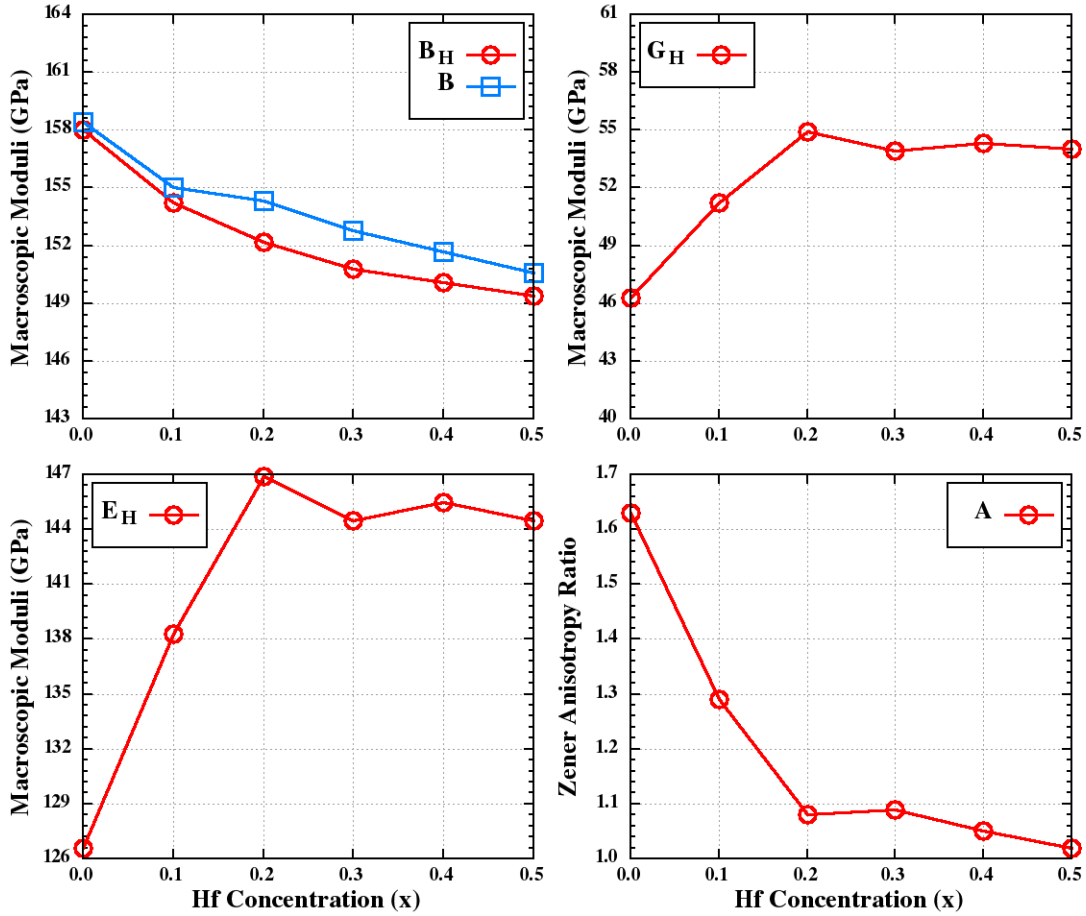


Figure 6.6: Hill's polycrystalline moduli and Zener anisotropy of $\text{NiTi}_{(1-x)}\text{Hf}_x$ in $B2$ structure as a function of Hf concentration x . In the left upper panel B is calculated by a Birch-Murnaghan fit.

The calculated elastic constants of $B19'$ structure as a function of x are shown in Figure 6.7. Our calculations predict an anisotropic behavior of elastic constants for the $B19'$ phase. One can see that for most elastic constants, there is no clear trend as a function of Hf concentration except for C_{55} which increases monotonously. The largest variation occur for C_{11} decreasing from 281 GPa at $x = 0$ to 255 GPa at $x = 0.5$. It should be noted that since the local atomic relaxation effect cannot be taken into account in the CPA, the internal atomic coordinates for all concentrations have been kept fixed at the values taken from Ref. [101] calculated for pure NiTi. However, experimental observations show that by increasing Hf content from $x = 0$ to $x = 0.4$ the internal atomic coordinates change causing increases for the Ni–Ni and Ti(Hf)–Ti(Hf) and decrease for Ni–Ti(Hf) average bond lengths [91]. Although there are no experimental observations for different elastic constants of $B19'$ phase as a function of Hf concentration, missing such an effect is most likely a reason for the anisotropic

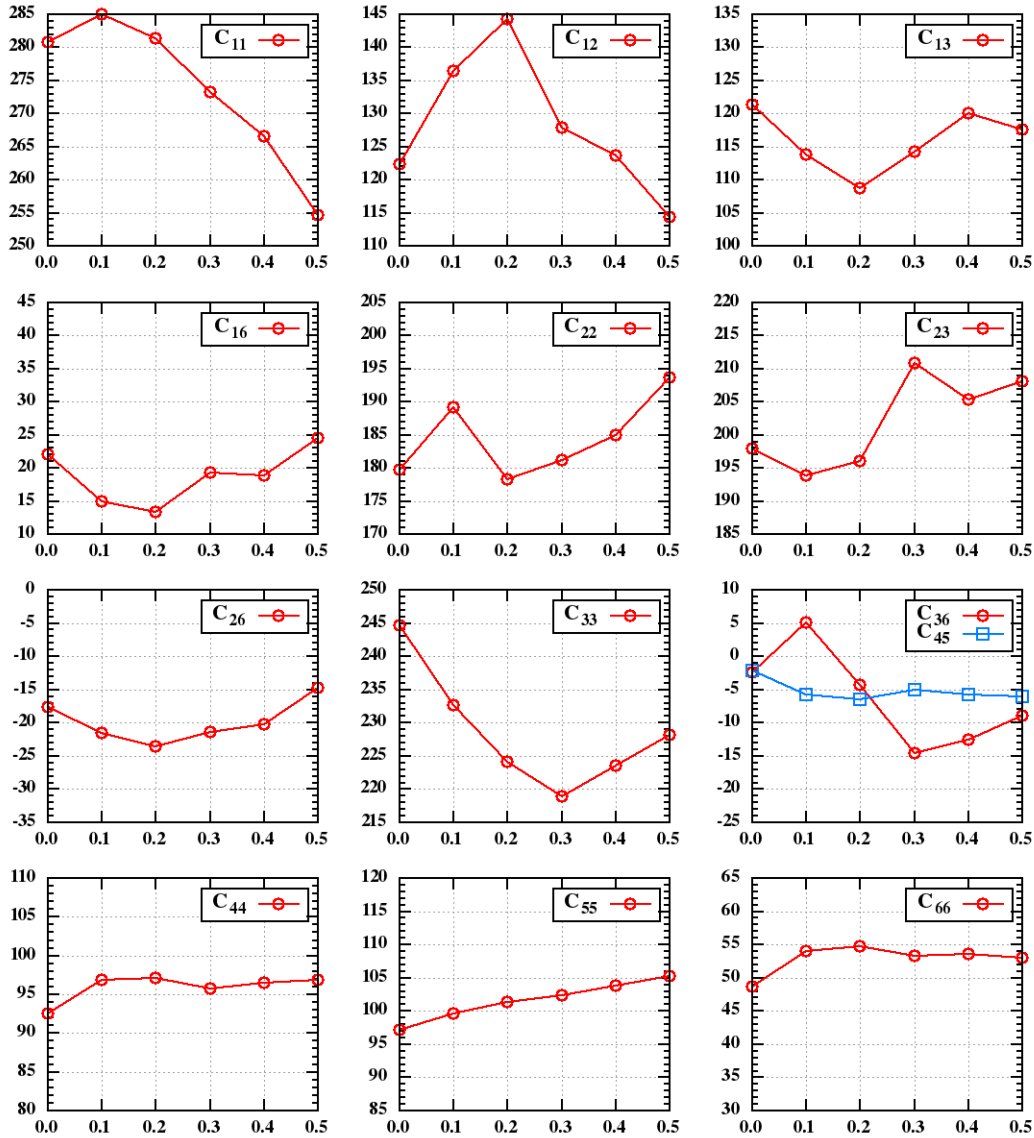


Figure 6.7: Elastic constants of $\text{NiTi}_{(1-x)}\text{Hf}_{(x)}$ in $B19'$ structure as a function of Hf concentration x .

behavior of the some constants.

The macroscopic moduli of the $B19'$ phase are depicted in Figure 6.8. The upper panel shows the bulk modulus B obtained by Birch-Murnaghan fit compared to Voigt and Reuss's bulk moduli. One can see from this graph that B_V and B , in contrast to B_R , show similar trends by increasing Hf concentration. Here the results for B_R at $x = \{0.2, 0.3, 0.4\}$ are larger than B_V . As it was discussed in Subsection 6.1.1, the Voigt's and Reuss's elastic moduli are the strict upper and lower limits of elastic moduli, respectively. Thus, B_V must be larger

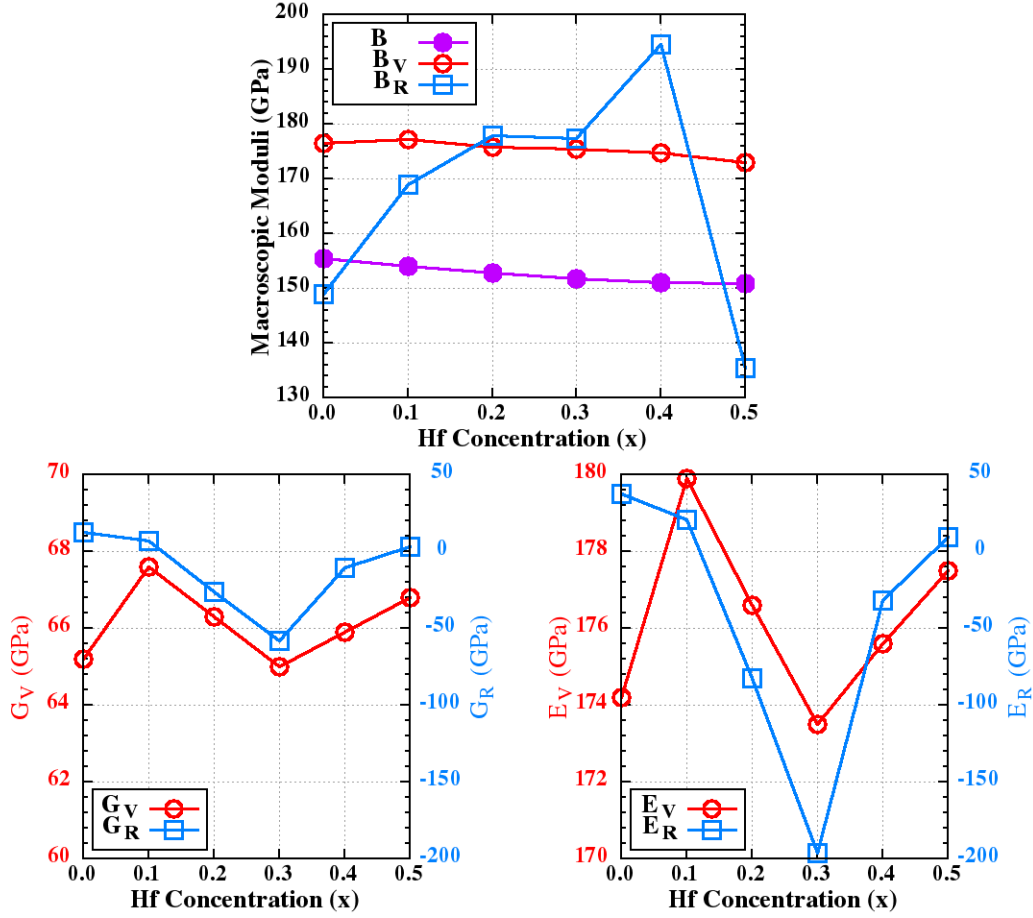


Figure 6.8: Polycrystalline moduli of NiTi_(1-x)Hf_(x) in *B19'* structure as a function of Hf concentration x . In the upper panel B is calculated by a Birch-Murnaghan fit.

than or equal to B_R for a crystal. The lower panels of this figure show the Voigt and Reuss's shear and Young's moduli as a function of x . From these graphs, one can see that our calculated Reuss's moduli from $x = 0.2$ to $x = 0.4$ become negative. To calculate the Reuss's elastic moduli, one must use the elements of the elastic compliance matrix s_{ij} (see Eqs. (6.22) and (6.23)), which is obtained by inverting the elastic constants matrix using the `ElaStic` package. The compliance matrix of the monoclinic structure (with $\gamma \neq 90$) has a form similar to the elastic constant matrix shown in Eq. (6.16), i.e, both are symmetric and have the same nonzero elements. One can show that each of those nonzero elements s_{ij} with $i = 1, 2, 3, 6$ depend on all C_{ij} with $i = 1, 2, 3, 6$, and the rest, i.e, s_{44} , s_{45} and s_{55} depend on all three elastic constants C_{44} , C_{45} and C_{55} . Thus, it is clear that even one miscalculated elastic constant can change the values of many compliance matrix elements and lead to such results. This is most likely due to missing the local atomic relaxation effect. The calculated values for E_R , A_{VR} and all Hill-averaged properties are also affected by the results for G_R and B_R (see

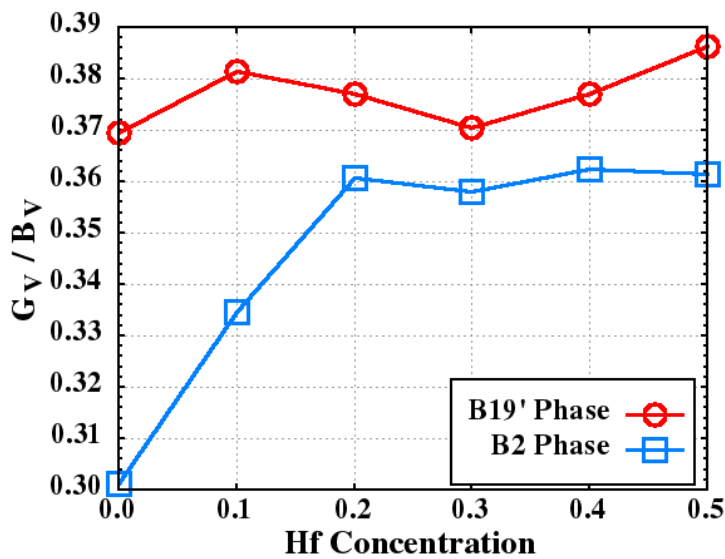
Table 6.7: G_V/B_V ratio for pure NiTi in $B2$ and $B19'$ phases.

		This work	Theory[101]	Theory[104]	Theory[103]	Exp
		EMTO	FLAPW+lo WIEN2k[8]	PAW VASP[9–11]	FLAPW[105]	
$B2$	G_V/B_V	0.30	0.20	0.11	0.22	0.19[107]
$B19'$	G_V/B_V	0.37	0.35	0.37	0.45	–

Subsection 6.1.1).

According to Pugh’s empirical rule [109], the ratio of G/B has a close relationship with ductile/brittle behavior of the material. Materials with $G/B \leq 0.57$ have a tendency to be ductile. This ratio for pure NiTi in both $B2$ and $B19'$ phases are shown in Table 6.7. All the computational methods including EMTO calculate this ratio less than 0.57, showing intrinsic ductility of pure NiTi in agreement with experiment. For the $B2$ our result overestimates G/B compared to experiment and other DFT results and for $B19'$ structure, our result is in a good agreement with other DFT results.

It is known by experimental observation that adding Hf makes the alloy less

**Figure 6.9:** G_V/B_V ratio for $\text{NiTi}_{(1-x)}\text{Hf}_{(x)}$ in $B2$ and $B19'$ phases as a function of Hf concentration x .

ductile [93]. For instance, experimental investigation on tensile behavior of the Ni₄₉Ti₃₆Hf₁₅ shows a partially brittle behavior for this alloy [110]. The graph of G_V/B_V ratio as a function of Hf content is illustrated in Figure 6.9. As one can see from this graph, according to the empirical Pugh's rule the EMTO-CPA calculations for both phases yield G_V/B_V for all values of x in the ductile regime, which is not in agreement with experiment. However, the overall trend of this ratio for the $B2$ phase shows that adding Hf content decreases the ductility, which is in agreement with experiment, while for the $B19'$ phase it does not change much compared to the $B2$ phase.

6.6 Conclusion

In this chapter, we have introduced a number of new improvements within the EMTO-CPA code as well as the integration with the **ElaStic** software which together yield better results for the elastic properties of solids, especially low symmetry crystals. We have applied these new implementations to calculate the structural and elastic properties of the shape memory alloys NiTi_(1-x)Hf_x ($x=0, 0.1, 0.2, 0.3, 0.4, 0.5$) in both the cubic $B2$ and the monoclinic $B19'$ phases. The **ElaStic** software automatizes the calculations by generating the input files and then calculating the elastic properties from the output files. The first modifications have been performed in the **kstr** package to increase the accuracy of Madelung matrices for high l s and also to speed up the calculation of the structure constants matrix and its energy derivatives.

Conventional EMTO-CPA calculations for investigating elastic constants of low symmetry crystals usually lead to ragged total energy–strain curves and consequently unreliable results. To improve this behavior, we have introduced the *Voro*-shape package as a replacement for the old shape package. This package employs a Voronoi method for tessellation of the space which in the case of low symmetry structures leads to a more accurate description of the total energy within the *FCD* technique. Applying this package for NiTi_(1-x)Hf_x in the monoclinic $B19'$ structure enhances the smoothness of the energy-strain curves. However, our calculations show that despite the great improvement of the smoothness of these curves by applying the *Voro*-shape package, there are still some points with discontinuous jumps. Further analysis to find the source of this behavior revealed that for the strains where the discontinuous jumps take place, the number of radial mesh points inside the inscribed spheres changes. Our calculations show that keeping the number of these mesh points for all distorted structures of a strain type constant, improves the energy trends at these points.

Our results for structural properties of NiTi_(1-x)Hf_x are in a good agreement

6.6. Conclusion

with experimental data, except the increasing c_0 lattice parameter of the monoclinic phase as a function of Hf concentration which is in contradiction with experimental data. The results for elastic constants of pure NiTi in the $B2$ phase show that the current implementation of EMTO-CPA usually overestimate these quantities which is in agreement with previous applications of this code on high symmetry crystals. The results for $\text{NiTi}_{(1-x)}\text{Hf}_x$ in this phase reveal a steep increase for C_{11} as a function of x until $x = 0.2$ and then it remains almost constant. A similar behavior has been obtained for the shear and Young's moduli. On the other hand, C_{12} , similar to the Zener anisotropy A , demonstrates a steep decrease as a function of x until $x = 0.2$ and then remains constant. The calculated value for C_{44} does not show any significant change for all values of Hf concentration.

The results for the elastic constants of pure NiTi in the $B19'$ phase confirm that with help of the above-mentioned improvements, the accuracy of the majority of the calculated elastic constants are in the same range as the ones for the $B2$ phase. However, there are also some constants such as C_{23} with a large difference compared to other computational results. We believe such discrepancies are related to two factors, first, using inconsistent data for the relaxed atomic positions and second, possibly higher influence of the non-spherical part of the potential on such properties of the low symmetry crystals that is not taken into account accurately in the current implementation of the EMTO-CPA code. For $\text{NiTi}_{(1-x)}\text{Hf}_x$ in the $B19'$ phase the majority of the calculated elastic constants do not show a clear trend as a function of Hf concentration. Thus, our calculations predict an anisotropic behavior for this properties. The unexpected calculated values for Reuss macroscopic elastic moduli of $x = \{0.2, 0.3, 0.4\}$ in the $B19'$ phase obtained from the calculated elastic constants also reveal the inaccuracy of the elastic constants results, which is most likely due to missing the local atomic relaxation effect.

Finally, our results for G_V/B_V of both phases and for all values of x yield values less than 0.57. According to Pugh's empirical rule, this means that our calculations predict a ductile behavior for all values of $0 \leq x \leq 0.5$ in both phases. For pure NiTi, this is in agreement with experiment, while, for $x \geq 0.3$ this is in contradiction with experiment. Nevertheless, the overall trend of our results for this ratio as a function of x confirms that by adding more Hf content, the ductility decreases which is in agreement with experimental observations.

Acknowledgments

Without the guidance and help from several people this dissertation would never have been able to be completed. On this very page, I would like to express my deep gratitude to them.

First and foremost, I would like to thank my scientific supervisor Andrei Ruban, for both teaching me the details of the EMTO-CPA method, and his guidance through the developments. His encouragements and supports beside his comprehensive knowledge and skills enlightened my way during these years. It is my honor to work under his supervision. I am extremely grateful to my academical supervisor Peter Puschnig, who gave me the chance to work as his PhD student. During these years, I have been impressed by his comprehensive knowledge in computational solid state physics as well as his programming skills. Thank you for your valuable time and patience in teaching me the basics of the ab initio methods and linear algebra. I also would like to thank both of my supervisors for their insightful comments, correcting my language and thorough proofreading of this dissertation.

I am indebted to Jürgen Spitaler for providing me this opportunity to work in atomistic modeling group at Material Center Leoben (MCL) Forschung GmbH. I would like to express my gratitude for his kindness, support and guidance especially during the calculation of elastic properties of NiTiHf alloys. I am immensely appreciative of Oleg Peil who was always willing to pay attention to my EMTO problems, and also for his guidance in the structure constants calculations and the fruitful discussions about the future developments. I would like also to thank him for reading and correcting some sections of my thesis. I want to express my deep gratitude to Thomas Dengg for both developing the integration of EMTO code with the Elastic software, and his helps for my accommodation at Leoben. I am blessed for having the pleasure of working with so many outstanding colleagues in atomistic modeling group at MCL who held friendly atmosphere in the group. Among whom, it is my pleasure to thank Lorenz Romaner, Vsevolod Razumovskiy, Maxim Popov, Daniel Scheiber and Anton Bochkarev for their help during these years.

This work would have not been possible without the financial support from the Competence Centre for Excellent Technologies (COMET) on Integrated Research in Materials, Processing and Product Engineering (MPPE). Financial support by the Austrian Federal Government and the Styrian Provincial Government is also acknowledged.

Above all, I would like to express my deepest gratitude to my beloved wife, Maedeh for all of her love, supports and encouragements. I could not complete my studies without her patience, understanding and sacrifices. I dedicate this thesis to her and also my wonderful son, Kian who came to this world in the middle of his journey and brought the most joyful moments to our life.

List of Figures

3.1	Intra-cell and inter-cell vectors in muffin-tin spheres	25
4.1	Demonstration of the CPA for a substitutional alloy with two alloy components A and B.	44
5.1	(a) Real and (b) imaginary parts of ss element of $S^a(\omega, \mathbf{k})$ of a bcc lattice for $\mathbf{k} = (0, 0, 0)$ as a function of complex ω . The mesh step for ω in complex plane is 0.5 on both real and imaginary axes.	56
5.2	The difference between the direct calculation and a 6th-order Taylor expansion of $S_{ss}^a(\omega, \mathbf{k})$, panel (a) and (b), and $\dot{S}_{ss}^a(\omega, \mathbf{k})$, panel (c) and (d), for a bcc lattice as a function of complex ω . The z axes in these graphs are real and imaginary of $ \Delta S_{ss}^a = \left S_{ss}^{a,Direct} - S_{ss}^{a,Taylor} \right $ and $ \Delta \dot{S}_{ss}^a = \left \dot{S}_{ss}^{a,Direct} - \dot{S}_{ss}^{a,Taylor} \right $. The expansion center is $\omega_0 = 0$	57
5.3	Relative error of S_{ss}^a and \dot{S}_{ss}^a as a function of ω in a logarithmic scale for bcc lattice corresponding to the graphs in Figure 5.2. The point $\omega = 0$ with $\delta S_{ss}^a = 0\%$ have been excluded for clarity.	58
5.4	Graphs of the volume optimization and shear moduli calculations data of W- bcc using both Taylor expansion and direct calculation methods.	59
5.5	Real (panel (a), (c)) and imaginary (panel (b), (d)) parts of elements S_{ss}^a and \dot{S}_{ss}^a , respectively, calculated directly for W- bcc as a function of complex ω for horizontal meshes parallel to the real axis in the complex plane.	60
5.6	Real and imaginary parts of some different diagonal elements of $S^a(\omega, \mathbf{k})$ and $\dot{S}^a(\omega, \mathbf{k})$ matrices for bcc -W at $\mathbf{k} = 0, 0, 0$ as a function of $\text{Re}(\omega)$ on a horizontal mesh with fixed $\text{Im}(\omega) \approx -0.01$. The y axes scales are different and not shown here for simplicity.	61
5.7	Real (left panel) and imaginary (right panel) parts of 2nd diagonal elements (pp elements) of \dot{S}_{ss}^a for bcc -W in terms of horizontal meshes of ω parallel to the real axis in complex plane.	62
5.8	The effect of cluster size on some selected diagonal elements of $\dot{S}^a(\omega, \mathbf{k} = (0, 0, 0))$ in bcc -W for a horizontal mesh with $\text{Im}(\omega) \approx -0.01$	63

LIST OF FIGURES

5.9	The effect of the number of Watson sphere orbitals on some selected diagonal elements of $\dot{S}^a(\omega, \mathbf{k} = (0, 0, 0))$ in <i>bcc</i> -W for a horizontal mesh with $\text{Im}(\omega) \approx -0.01$	64
5.10	The effect of hard sphere radii on <i>ss</i> elements of $\dot{S}^a(\omega, \mathbf{k} = (0, 0, 0))$ in <i>bcc</i> -W for a horizontal mesh with $\text{Im}(\omega) \approx -0.01$	65
6.1	The total energy versus strain using old shape and voro-shape programs for some selected deformation types of pure NiTi in <i>B19'</i> phase.	79
6.2	The total energy versus strain using voro-shape program in <i>FRMS</i> mode compared to normal mode for some selected deformation types of pure NiTi in <i>B19'</i> phase.	80
6.3	The calculated unit cell volumes of $\text{NiTi}_{1-x}\text{Hf}_x$ as a function of Hf concentration x for <i>B2</i> phase and <i>B19'</i> phase divided by 2 in comparison with <i>B19'</i> experimental data (Exp ¹ from Ref. [96] for pure NiTi and Exp ² from Ref. [91] for ($x \neq 0$)).	83
6.4	The calculated lattice parameters and the monoclinic angle of $\text{NiTi}_{1-x}\text{Hf}_x$ as a function of Hf concentration x compared to the experimental results. Exp ¹ data are those repeated in Table 6.2 taken from Ref. [96] and Exp ² data are taken from Ref. [91].	84
6.5	Elastic constants of $\text{NiTi}_{(1-x)}\text{Hf}_{(x)}$ in <i>B2</i> structure as a function of Hf concentration x	89
6.6	Hill's polycrystalline moduli and Zener anisotropy of $\text{NiTi}_{(1-x)}\text{Hf}_{(x)}$ in <i>B2</i> structure as a function of Hf concentration x . In the left upper panel B is calculated by a Birch-Murnaghan fit.	90
6.7	Elastic constants of $\text{NiTi}_{(1-x)}\text{Hf}_{(x)}$ in <i>B19'</i> structure as a function of Hf concentration x	91
6.8	Polycrystalline moduli of $\text{NiTi}_{(1-x)}\text{Hf}_{(x)}$ in <i>B19'</i> structure as a function of Hf concentration x . In the upper panel B is calculated by a Birch-Murnaghan fit.	92
6.9	G_V/B_V ratio for $\text{NiTi}_{(1-x)}\text{Hf}_{(x)}$ in <i>B2</i> and <i>B19'</i> phases as a function of Hf concentration x	93

List of Tables

5.1	Lattice parameter a_0 (Å), bulk modulus B , shear moduli C' and C_{44} (all moduli in (GPa)) of <i>bcc</i> -W using different exchange-correlation functional and a 6th-order Taylor expansion compared with other computational results and experimental data.	59
6.1	Experimental crystallographic data of the two phases $B2$ and $B19'$ of NiTi.	76
6.2	Equilibrium lattice parameter (Å) and unit cell volume (Å ³) of NiTi in $B2$ phase and equilibrium lattice parameters, unit cell volume divided by 2 (for a better comparison with $B2$ phase) and monoclinic angle γ (degree) in $B19'$ phase of pure NiTi compared to the other computational results and experimental data. In all of the computational methods referenced here, the PBE-GGA has applied for exchange-correlation functional.	82
6.3	Calculated elastic constants, shear moduli C' and bulk modulus B (all moduli in (GPa)) of pure NiTi in $B2$ phase compared to other computational results and experimental data. B is calculated by applying the Birch-Murnaghan fit.	85
6.4	Calculated macroscopic elastic properties of NiTi in $B2$ structure comparing with other computational results and experimental data. Only the Hill bulk modulus B_H is reported, because for cubic structures $B_V = B_R = B_H$. All moduli are given in GPa, except for A , A_{VR} , and ν_H which are dimensionless.	86
6.5	Calculated elastic constants and bulk modulus B (all moduli in (GPa)) of NiTi in $B19'$ structure comparing with other computational results. B is calculated by applying the Birch-Murnaghan fit.	87
6.6	Calculated macroscopic elastic properties of NiTi in $B19'$ structure comparing with other computational results.	88
6.7	G_V/B_V ratio for pure NiTi in $B2$ and $B19'$ phases.	93

Bibliography

- [1] P. Hohenberg and W. Kohn. *Inhomogeneous Electron Gas*. *Phys. Rev.*, 136:B864–B871, Nov 1964.
- [2] W. Kohn and L. J. Sham. *Self-Consistent Equations Including Exchange and Correlation Effects*. *Phys. Rev.*, 140:A1133–A1138, Nov 1965.
- [3] J. C. Slater. *Wave Functions in a Periodic Potential*. *Phys. Rev.*, 51:846–851, May 1937.
- [4] G. K. H. Madsen, Blaha. P., K. Schwarz, E. Sjöstedt, and L. Nordström. *Efficient linearization of the augmented plane-wave method*. *Phys. Rev. B*, 64:195134, Oct 2001.
- [5] O. Krogh Andersen. *Linear methods in band theory*. *Phys. Rev. B*, 12:3060–3083, Oct 1975.
- [6] Marvin L. Cohen and Volker Heine. *The fitting of pseudopotentials to experimental data and their subsequent application*. volume 24 of *Solid State Physics*, pages 37 – 248. Academic Press, 1970.
- [7] J. Hutter, H. P. Lthi, and M. Parrinello. *Electronic structure optimization in plane-wave-based density functional calculations by direct inversion in the iterative subspace*. *Computational Materials Science*, 2(2):244 – 248, 1994.
- [8] P. Blaha, K. Schwarz, G. Madsen, D. Kvasnicka, and J. Luitz. Wien2k: An augmented plane wave plus local orbitals program for calculating crystal properties, 2001.
- [9] G. Kresse and J. Hafner. *Ab initio molecular dynamics for liquid metals*. *Phys. Rev. B*, 47:558–561, Jan 1993.
- [10] G. Kresse and J. Furthmüller. *Efficiency of ab-initio total energy calculations for metals and semiconductors using a plane-wave basis set*. *Computational Materials Science*, 6(1):15 – 50, 1996.
- [11] G. Kresse and J. Furthmüller. *Efficient iterative schemes for ab initio total-energy calculations using a plane-wave basis set*. *Phys. Rev. B*, 54:11169–11186, Oct 1996.
- [12] J. Koringa. *On the calculation of the energy of a Bloch wave in a metal*. *Physica*, 13(67):392 – 400, 1947.
- [13] W. Kohn and N. Rostoker. *Solution of the Schrödinger Equation in Periodic Lattices with an Application to Metallic Lithium*. *Phys. Rev.*, 94:1111–1120, Jun 1954.

BIBLIOGRAPHY

- [14] B. L. Gyorffy. *Coherent-Potential Approximation for a Nonoverlapping-Muffin-Tin-Potential Model of Random Substitutional Alloys*. *Phys. Rev. B*, 5:2382–2384, Mar 1972.
- [15] P. Soven. *Coherent-Potential Model of Substitutional Disordered Alloys*. *Phys. Rev.*, 156:809–813, Apr 1967.
- [16] B. L. Gyorffy, A. J. Pindor, J. Staunton, G. M. Stocks, and H. Winter. *A first-principles theory of ferromagnetic phase transitions in metals*. *Journal of Physics F: Metal Physics*, 15(6):1337, 1985.
- [17] A. J. Pindor, J. Staunton, G. M. Stocks, and H. Winter. *Disordered local moment state of magnetic transition metals: a self-consistent KKR CPA calculation*. *Journal of Physics F: Metal Physics*, 13(5):979, 1983.
- [18] O. K. Andersen, O. Jepsen, and G. Krier. *Exact Muffin-Tin Orbital Theory*, pages 63–124.
- [19] L. Vitos, I. A. Abrikosov, and B. Johansson. *Anisotropic Lattice Distortions in Random Alloys from First-Principles Theory*. *Phys. Rev. Lett.*, 87:156401, Sep 2001.
- [20] L. Vitos. *Computational Quantum Mechanics for Materials Engineers, The EMTO Method and Applications*. Springer-Verlag London, 2007.
- [21] L. V. Pourovskii, A. V. Ruban, L. Vitos, H. Ebert, B. Johansson, and I. A. Abrikosov. *Fully relativistic spin-polarized exact muffin-tin-orbital method*. *Phys. Rev. B*, 71:094415, Mar 2005.
- [22] L. Vitos, H.L. Skriver, B. Johansson, and J. Kollár. *Application of the exact muffin-tin orbitals theory: the spherical cell approximation*. *Computational Materials Science*, 18(1):24 – 38, 2000.
- [23] L. Vitos, J. Kollár, and H. L. Skriver. *Full charge-density scheme with a kinetic-energy correction: Application to ground-state properties of the 4d metals*. *Phys. Rev. B*, 55:13521–13527, May 1997.
- [24] L. Vitos. *Total-energy method based on the exact muffin-tin orbitals theory*. *Phys. Rev. B*, 64:014107, Jun 2001.
- [25] R. Golezorkhtabar, P. Pavone, J. Spitaler, P. Puschnig, and C. Draxl. *ElaStic: A tool for calculating second-order elastic constants from first principles*. *Computer Physics Communications*, 184(8):1861 – 1873, 2013.
- [26] M. Born and R. Oppenheimer. *Zur Quantentheorie der Molekeln*. *Annalen der Physik*, 389(20):457–484, 1927.
- [27] R. G. Parr and W. Yang. *Density-Functional Theory of Atoms and Molecules*. Oxford University Press, New York, USA, 1989.

BIBLIOGRAPHY

- [28] L. H. Thomas. *The calculation of atomic fields*. *Proc. Cambridge Phil. Soc.*, 23:542–548, 1927.
- [29] E. Fermi. *Un metodo statistico per la determinazione di alcune proprieta del atomo*. *Atti Acad. Naz. Lincei, Rend.*, 6:602–607, 1927.
- [30] P. A. M. Dirac. *Note on Exchange Phenomena in the Thomas Atom*. *Mathematical Proceedings of the Cambridge Philosophical Society*, 26(3):376–385, 1930.
- [31] M. Levy. *Universal variational functionals of electron densities, first-order density matrices, and natural spin-orbitals and solution of the v-representability problem*. *Proc. Natl. Acad. Sci. USA*, 76:6062–6065, 1979.
- [32] M. Levy and J. P. Perdew. *The Constrained Search Formulation of Density Functional Theory*, pages 11–30. Springer US, Boston, MA, 1985.
- [33] J. W. S. Rayleigh. *On the instability of cylindrical fluid surfaces*. *Phylos. Mag*, 34:481, 1892.
- [34] M. Gell-Mann and K. A. Brueckner. *Correlation Energy of an Electron Gas at High Density*. *Phys. Rev.*, 106:364–368, Apr 1957.
- [35] R. A. ColdwellHorsfall and A. Maradudin. *ZeroPoint Energy of an Electron Lattice*. *Journal of Mathematical Physics*, 1(5):395–404, 1960.
- [36] J. P. Perdew and Y. Wang. *Accurate and simple analytic representation of the electron-gas correlation energy*. *Phys. Rev. B*, 45:13244–13249, Jun 1992.
- [37] D. M. Ceperley and B. J. Alder. *Ground State of the Electron Gas by a Stochastic Method*. *Phys. Rev. Lett.*, 45:566–569, Aug 1980.
- [38] L. Hedin and B. I. Lundqvist. *Explicit local exchange-correlation potentials*. *Journal of Physics C: Solid State Physics*, 4(14):2064, 1971.
- [39] von Barth U and L. Hedin. *A local exchange-correlation potential for the spin polarized case*. *Journal of Physics C: Solid State Physics*, 5(13):1629, 1972.
- [40] O. Gunnarsson and B. I. Lundqvist. *Exchange and correlation in atoms, molecules, and solids by the spin-density-functional formalism*. *Phys. Rev. B*, 13:4274–4298, May 1976.
- [41] S. H. Vosko, L. Wilk, and M. Nusair. *Accurate spin-dependent electron liquid correlation energies for local spin density calculations: a critical analysis*. *Canadian Journal of Physics*, 58(8):1200–1211, 1980.
- [42] J. P. Perdew and A. Zunger. *Self-interaction correction to density-functional approximations for many-electron systems*. *Phys. Rev. B*, 23:5048–5079, May 1981.

BIBLIOGRAPHY

- [43] J. P. Perdew and S. Kurth. *Density Functionals for Non-relativistic Coulomb Systems in the New Century*, pages 1–55. Springer-Verlag Berlin Heidelberg, Berlin Heidelberg, 2003.
- [44] F. Herman, J. P. Van Dyke, and I. B. Ortenburger. *Improved Statistical Exchange Approximation for Inhomogeneous Many-Electron Systems*. *Phys. Rev. Lett.*, 22:807–811, Apr 1969.
- [45] J. P. Perdew and K. Burke. *Comparison shopping for a gradient-corrected density functional*. *International Journal of Quantum Chemistry*, 57(3):309–319, 1996.
- [46] P. S. Svendsen and U. von Barth. *Gradient expansion of the exchange energy from second-order density response theory*. *Phys. Rev. B*, 54:17402–17413, Dec 1996.
- [47] A. D. Becke. *Density-functional exchange-energy approximation with correct asymptotic behavior*. *Phys. Rev. A*, 38:3098–3100, Sep 1988.
- [48] J. P. Perdew, K. Burke, and M. Ernzerhof. *Generalized Gradient Approximation Made Simple*. *Phys. Rev. Lett.*, 77:3865–3868, Oct 1996.
- [49] S. K. Ma and K. A. Brueckner. *Correlation Energy of an Electron Gas with a Slowly Varying High Density*. *Phys. Rev.*, 165:18–31, Jan 1968.
- [50] David J. Singh and Lars Nordström. *Planewaves, Pseudopotentials, and the LAPW Method*. Springer US, 2006.
- [51] Y. Mokrousov, G. Bihlmayer, and S. Blügel. *Full-potential linearized augmented plane-wave method for one-dimensional systems: Gold nanowire and iron monowires in a gold tube*. *Phys. Rev. B*, 72:045402, Jul 2005.
- [52] K. Koepf and H. Eschrig. *Full-potential nonorthogonal local-orbital minimum-basis band-structure scheme*. *Phys. Rev. B*, 59:1743–1757, Jan 1999.
- [53] B. Drittler, M. Weinert, R. Zeller, and P.H. Dederichs. *Vacancy formation energies of fcc transition metals calculated by a full potential green’s function method*. *Solid State Communications*, 79(1):31 – 35, 1991.
- [54] T. Hühne, C. Zecha, H. Ebert, P. H. Dederichs, and R. Zeller. *Full-potential spin-polarized relativistic Korringa-Kohn-Rostoker method implemented and applied to bcc Fe, fcc Co, and fcc Ni*. *Phys. Rev. B*, 58:10236–10247, Oct 1998.
- [55] M. Methfessel. *Elastic constants and phonon frequencies of Si calculated by a fast full-potential linear-muffin-tin-orbital method*. *Phys. Rev. B*, 38:1537–1540, Jul 1988.
- [56] S. Y. Savrasov and D. Y. Savrasov. *Electron-phonon interactions and related physical properties of metals from linear-response theory*. *Phys. Rev. B*, 54:16487–16501, Dec 1996.

BIBLIOGRAPHY

- [57] G. Kresse and J. Furthmüller. *Efficient iterative schemes for ab initio total-energy calculations using a plane-wave basis set*. *Phys. Rev. B*, 54:11169–11186, Oct 1996.
- [58] C. Hartwigsen, S. Goedecker, and J. Hutter. *Relativistic separable dual-space Gaussian pseudopotentials from H to Rn*. *Phys. Rev. B*, 58:3641–3662, Aug 1998.
- [59] A. Kiejna, G. Kresse, J. Rogal, A. Sarkar, K. Reuter, and M. Scheffler. *Comparison of the full-potential and frozen-core approximation approaches to density-functional calculations of surfaces*. *Phys. Rev. B*, 73:035404, Jan 2006.
- [60] Hans L. Skriver. *The LMTO Method*. Springer-Verlag Berlin Heidelberg, 1984.
- [61] O. K. Andersen, O. Jepsen, and M. Sob. *Linearized band structure methods*, pages 1–57. Springer Berlin Heidelberg, Berlin, Heidelberg, 1987.
- [62] R. W. Tank and C. Arcangeli. *An Introduction to the Third-Generation LMTO Method*. *physica status solidi (b)*, 217(1):89–130, 2000.
- [63] Lord Rayleigh Sec. R. S. *LVI. On the influence of obstacles arranged in rectangular order upon the properties of a medium*. *Philosophical Magazine Series 5*, 34(211):481–502, 1892.
- [64] A. Gonis and W. H. Butler. *Multiple Scattering in Solids*. Springer New York, 2000.
- [65] J. D. Jackson. *Classical Electrodynamics, 3rd Edition*. Wiley, NewYork, 1999.
- [66] L. Vitos, J. Kollár, and H. L. Skriver. *Full charge-density calculation of the surface energy of metals*. *Phys. Rev. B*, 49:16694–16701, Jun 1994.
- [67] B. Drittler, M. Weinert, R. Zeller, and P.H. Dederichs. *Vacancy formation energies of fcc transition metals calculated by a full potential green’s function method*. *Solid State Communications*, 79(1):31 – 35, 1991.
- [68] A. Gonis, Erik C. Sowa, and P. A. Sterne. *Exact treatment of Poisson’s equation in solids with space-filling cells*. *Phys. Rev. Lett.*, 66:2207–2210, Apr 1991.
- [69] L. Vitos and J. Kollár. *Optimized l-convergency in the solution of Poisson’s equation with space-filling cells*. *Phys. Rev. B*, 51:4074–4078, Feb 1995.
- [70] I. A. Abrikosov, A. M. N. Niklasson, S. I. Simak, B. Johansson, A. V. Ruban, and H. L. Skriver. *Order- N Green’s Function Technique for Local Environment Effects in Alloys*. *Phys. Rev. Lett.*, 76:4203–4206, May 1996.
- [71] I. A. Abrikosov, S. I. Simak, B. Johansson, A. V. Ruban, and H. L. Skriver. *Locally self-consistent Green’s function approach to the electronic structure problem*. *Phys. Rev. B*, 56:9319–9334, Oct 1997.

BIBLIOGRAPHY

- [72] A. V. Ruban, S. I. Simak, P. A. Korzhavyi, and H. L. Skriver. *Screened Coulomb interactions in metallic alloys. II. Screening beyond the single-site and atomic-sphere approximations*. *Phys. Rev. B*, 66:024202, Jun 2002.
- [73] A. V. Ruban and H. L. Skriver. *Screened Coulomb interactions in metallic alloys. I. Universal screening in the atomic-sphere approximation*. *Phys. Rev. B*, 66:024201, Jun 2002.
- [74] A. Gonis, G. M. Stocks, W. H. Butler, and H. Winter. *Local-environment fluctuations and densities of states in substitutionally disordered alloys*. *Phys. Rev. B*, 29:555–567, Jan 1984.
- [75] A. V. Ruban, S. I. Simak, S. Shallcross, and H. L. Skriver. *Local lattice relaxations in random metallic alloys: Effective tetrahedron model and supercell approach*. *Phys. Rev. B*, 67:214302, Jun 2003.
- [76] O. K. Andersen, O. Jepsen, and D. Glötzl. *Highlights of Condensed-Matter Theory*, pages 59–176.
- [77] A. E. Kissavos, L. Vitos, and I. A. Abrikosov. *Energy dependence of exact muffin-tin-orbital structure constants*. *Phys. Rev. B*, 75:115117, Mar 2007.
- [78] R. A. Ayres, G. W. Shannette, and D. F. Stein. *Elastic constants of tungsten-rhenium alloys from 77 to 298 K*. *Journal of Applied Physics*, 46(4):1526–1530, 1975.
- [79] L. Romaner, C. Ambrosch-Draxl, and R. Pippan. *Effect of Rhenium on the Dislocation Core Structure in Tungsten*. *Phys. Rev. Lett.*, 104:195503, May 2010.
- [80] M. J. Mehl, B. M. Klein, and D. A. Papaconstantopoulos. *First-principles calculation of elastic properties of metals*, volume 1, pages 195–210. Wiley, London, 1994.
- [81] P. P. Ewald. *Die Berechnung optischer und elektrostatischer Gitterpotentiale*. *Annalen der Physik*, 369(3):253–287, 1921.
- [82] F. S. Ham and B. Segall. *Energy Bands in Periodic Lattices—Green’s Function Method*. *Phys. Rev.*, 124:1786–1796, Dec 1961.
- [83] E. Bruno and B. Ginatempo. *Algorithms for Korringa-Kohn-Rostoker electronic structure calculations in any Bravais lattice*. *Phys. Rev. B*, 55:12946–12955, May 1997.
- [84] A. Taga, L. Vitos, B. Johansson, and G. Grimvall. *Ab initio calculation of the elastic properties of $Al_{1-x}Li_x$ random alloys*. *Phys. Rev. B*, 71:014201, Jan 2005.
- [85] A. Breidi, S. G. Fries, M. Palumbo, and A.V. Ruban. *First-principles modeling of energetic and mechanical properties of NiCr, NiRe and CrRe random alloys*. *Computational Materials Science*, 117:45 – 53, 2016.

BIBLIOGRAPHY

- [86] J. F. Nye. *Physical Properties of Crystals*. Oxford University Press, New York, USA, 1985.
- [87] W. Voigt. *Lehrbuch der Kristallphysik (mit Ausschluss der Kristalloptik)*. Springer Fachmedien Wiesbaden, 1966.
- [88] A. Reuss. *Berechnung der Fliegrenze von Mischkristallen auf Grund der Plastizitätsbedingung für Einkristalle*. *ZAMM - Journal of Applied Mathematics and Mechanics / Zeitschrift für Angewandte Mathematik und Mechanik*, 9(1):49–58, 1929.
- [89] R. Hill. *The Elastic Behaviour of a Crystalline Aggregate*. *Proceedings of the Physical Society. Section A*, 65(5):349, 1952.
- [90] R. Hill. *Elastic properties of reinforced solids: Some theoretical principles*. *Journal of the Mechanics and Physics of Solids*, 11(5):357 – 372, 1963.
- [91] M. Zarinejad, Y. Liu, and T. J. White. *The crystal chemistry of martensite in NiTiHf shape memory alloys*. *Intermetallics*, 16(7):876 – 883, 2008.
- [92] J. Ma, I. Karaman, and R. D. Noebe. *High temperature shape memory alloys*. *International Materials Reviews*, 55(5):257–315, 2010.
- [93] H. E. Karaca, E. Acar, H. Tobe, and S. M. Saghayan. *NiTiHf-based shape memory alloys*. *Materials Science and Technology*, 30(13):1530–1544, 2014.
- [94] Frederick E. Wang, Stanley J. Pickart, and Harvey A. Alperin. *Mechanism of the TiNi Martensitic Transformation and the Crystal Structures of TiNiII and TiNiIII Phases*. *Journal of Applied Physics*, 43(1):97–112, 1972.
- [95] G. M. Michal and R. Sinclair. *The structure of TiNi martensite*. *Acta Crystallographica Section B*, 37(10):1803–1807, Oct 1981.
- [96] Y. Kudoh, M Tokonami, S Miyazaki, and K Otsuka. *Crystal structure of the martensite in Ti-49.2 at.single crystal X-ray diffraction method*. *Acta Metallurgica*, 33(11):2049 – 2056, 1985.
- [97] Mahdi Sanati, R. C. Albers, and F. J. Pinski. *Electronic and crystal structure of NiTi martensite*. *Phys. Rev. B*, 58:13590–13593, Nov 1998.
- [98] S.D. Prokoshkin, A.V. Korotitskiy, V. Brailovski, S. Turenne, I.Yu. Khmelevskaya, and I.B. Trubitsyna. *On the lattice parameters of phases in binary TiNi shape memory alloys*. *Acta Materialia*, 52(15):4479 – 4492, 2004.
- [99] C. M. Hwang, M. Meichle, M. B. Salamon, and C. M. Wayman. *Transformation behaviour of a Ti50Ni47Fe3 alloy I. Premartensitic phenomena and the incommensurate phase*. *Philosophical Magazine A*, 47(1):9–30, 1983.

BIBLIOGRAPHY

- [100] P. Sittner, P. Luks, D. Neov, V. Novk, and D.M. Toebbens. *In situ neutron diffraction studies of martensitic transformations in NiTi*. *J. Phys. IV France*, 112:709–711, 2003.
- [101] R. Golesorkhtabar. *Ab initio Calculation of Elastic Properties General Implementation and Specific Application to the Shape-Memory Material NiTi*. PhD thesis, University of Leoben, Austria, 2013.
- [102] C. H. Rycroft. *VORO++: A three-dimensional Voronoi cell library in C++*. *Chaos: An Interdisciplinary Journal of Nonlinear Science*, 19(4):041111, 2009.
- [103] N. Hatcher, O. Yu. Kontsevoi, and A. J. Freeman. *Role of elastic and shear stabilities in the martensitic transformation path of NiTi*. *Phys. Rev. B*, 80:144203, Oct 2009.
- [104] M.F.-X. Wagner and W. Windl. *Lattice stability, elastic constants and macroscopic moduli of NiTi martensites from first principles*. *Acta Materialia*, 56(20):6232 – 6245, 2008.
- [105] E. Wimmer, H. Krakauer, M. Weinert, and A. J. Freeman. *Full-potential self-consistent linearized-augmented-plane-wave method for calculating the electronic structure of molecules and surfaces: O₂ molecule*. *Phys. Rev. B*, 24:864–875, Jul 1981.
- [106] P. L. Potapov, A. V. Shelyakov, A. A. Gulyaev, E. L. Svistunov, N.M. Matveeva, and D. Hodgson. *Effect of Hf on the structure of Ni-Ti martensitic alloys*. *Materials Letters*, 32(4):247 – 250, 1997.
- [107] O. Mercier, K. N. Melton, G. Gremaud, and J. Hgi. *Singlecrystal elastic constants of the equiatomic NiTi alloy near the martensitic transformation*. *Journal of Applied Physics*, 51(3):1833–1834, 1980.
- [108] T. M. Brill, S. Mittelbach, W. Assmus, M. Mullner, and B. Luthi. *Elastic properties of NiTi*. *Journal of Physics: Condensed Matter*, 3(48):9621, 1991.
- [109] S.F. Pugh. *Relations between the elastic moduli and the plastic properties of polycrystalline pure metals*. *The London, Edinburgh, and Dublin Philosophical Magazine and Journal of Science*, 45(367):823–843, 1954.
- [110] Y.Q. Wang, Y.F. Zheng, W. Cai, and L.C. Zhao. *The tensile behavior of Ti₃₆Ni₄₉Hf₁₅ high temperature shape memory alloy*. *Scripta Materialia*, 40(12):1327 – 1331, 1999.